Investigations of Semiconductor Laser Modulation Dynamics and Field Fluctuations

Thesis by

Michael Avery Newkirk

In Partial Fulfillment of the Requirements

for the Degree of

Doctor of Philosophy

California Institute of Technology

Pasadena, California

1991

(Defended May 21, 1991)

to Lily

Acknowledgments

I wish to express deep thanks to my parents (who may read at least this far into the dissertation). Now they can stop wondering if I'm ever going to finish school. I especially thank my advisor, Kerry Vahala. I have thoroughly enjoyed working with him and learning from him. He has shared with me many seminal ideas and a beautiful laboratory in which to do research. I know I will always look back with pride on what we accomplished.

Of course, everyone in the Vahala group who has helped make the pursuit of a Ph. D. more interesting deserves to have their name in print: Michael Hoenk, Pete Sercel, John Lebens, Charles Tsai, Jay Dawson, Namkyoo Park, and Winston Saunders. Good luck to all of you. Others who have helped out in dire times include Bill Bridges, Steve Sanders, Lars Eng, Hal Zarem, Ed Croke, Ed Yu, and especially Carl (Chück) Krill. Also, the assistance of Vicky Arriola, Rosalie Rowe, and Larry Begay is much appreciated.

Many of the experiments in this thesis were performed with lasers and detectors supplied by Ortel Corporation. Those from Ortel who have donated their time and expertise are Joel Paslaski, T. R. Chen, Kam Lau, Hank Blauvelt, Nadav Bar-Chaim, Norman Kwong, and Amnon Yariv. I also thank Tom Koch of AT&T Bell Labs for his cooperation.

Regarding my financial support, I gratefully acknowledge fellowships from IBM Corporation and Rockwell International. I also appreciate the opportunity I had to moonlight as a T.A. for APh 50 for three years. In addition, the National Science

Foundation and the Caltech Program in Advanced Technologies provided funding for much of the research in this thesis.

Special thanks go to my grandfather, who first exposed me to the amazing world of Caltech and JPL. I also thank Prof. David Park of Williams College with whom I spent a valuable year of independent study in physics.

Finally, my deepest thanks go to my wife, Lily. Your understanding and love during these past five years have been the greatest.

Abstract

Active-layer photomixing is an optical modulation technique to probe the fundamental modulation response of a semiconductor laser. By heterodyning two laser sources with a tunable frequency difference in the device's active region, the gain, and hence the optical output, is modulated at the beat frequency of the sources. Using an equivalent circuit model for the laser diode, the optical modulation is shown to be decoupled from the electrical parasitics of the laser structure. The fundamental modulation response of the laser can thereby be studied independently of the parasitic response, which would otherwise mask the fundamental response. The photomixing technique is used on GaAs/GaAlAs lasers at room temperature, liquid nitrogen and liquid helium temperature, and it is verified that the modulation response appears ideal to millimeter-wave frequencies.

Application of the active-layer photomixing technique led to the discovery and explanation of a new effect called the "gain lever." It enhances the modulation efficiency of a semiconductor laser with a quantum well active layer. By inhomogeneously pumping the device, regions with unequal differential gain are created. If the laser is above threshold, then the overall modal gain is clamped, and by modulating the section with larger differential gain, the output power can be modulated with greater than unity quantum efficiency.

The fundamental coupling between intensity noise and phase noise in semiconductor laser light is investigated. This coupling, described by the α parameter, causes the well-known linewidth enhancement, but also implies the fluctuations are corre-

lated. By the technique of "amplitude-phase decorrelation," the intensity noise can be passively reduced by the ratio $1/(1+\alpha^2)$. Using a Michelson interferometer as a frequency discriminator, intensity noise from a DFB laser is reduced below its intrinsic level up to a factor of 28.

A balanced homodyne detection scheme is used to study the noise reduction in relation to the photon shot noise floor. The decorrelated intensity noise can be reduced to within a dB of the shot noise level. Reduction below shot noise may be inhibited by uncorrelated phase noise in the lasing mode.

Contents

List of Figures

Chapter 1

Introduction

1.1 Semiconductor lasers

Since the first reports of lasing emission from a semiconductor p-n junction device in 1962 [1]–[4], semiconductor lasers have developed at a remarkable pace [5], [6]. Initially, the high injection current densities needed to reach lasing threshold caused severe heating problems. Lasing action could only be generated continuously at low temperature or in pulsed operation at room temperature. Device lifetimes were short. Since that time, fabrication technology and device design have progressed to the point where lasers with extrapolated room temperature lifetimes of a century are commonplace. Because of their low cost, reliability, low power consumption, and capability for high-speed modulation, among other features, semiconductor lasers are attractive sources of coherent light for a variety of applications. Most notably, semiconductor lasers are beginning to play a major role in the expanding lightwave communications industry.

The semiconductor material systems for laser fabrication are generally of two main types, the GaAs/GaAlAs system and InP/InGaAsP system. In a conventional buried heterostructure design, the laser's active region (where the lasing occurs) is composed of a lower bandgap material, such as GaAs, which is surrounded by higher bandgap material, such as GaAlAs, in order to confine the injected carriers (the source of the optical gain) and to guide the optical mode. GaAs/GaAlAs devices typically have lasing wavelengths in the range 0.7–0.9 μm while InP/InGaAsP devices can be made to operate at longer wavelengths within the 1.1–1.6 μm range. There are many applications which dictate the choice of lasing wavelength. For instance, longer wavelength lasers are required for long-distance terrestrial optical communication because the wavelength region of minimum loss for silica fiber occurs near 1.55 μm. In an optical disk memory, where information is read or written by a focused laser beam, a shorter wavelength laser is advantageous because the light may be focused to a smaller spot, increasing the storage density.

Specialized laser structures are currently fabricated to optimize specific features of their performance. A few important examples are listed here. Lasers designed for high-speed intensity modulation can have direct modulation bandwidths of over 10 GHz, allowing information to be conveyed on an optical carrier at very high rates [7], [8]. In contrast to the more conventional Fabry-Perot laser cavity formed by the cleaved semiconductor crystal facets, single-frequency lasing (side-mode suppression $>$ 30 dB) is achieved in distributed feedback and distributed Bragg reflector cavity configurations [9]. Improved single-frequency sources which have a narrow

linewidth [10] and tunability [11], [12] are also being developed. These types of devices will be necessary components of future coherent lightwave communication systems. Lasers with a quantum-well (i.e., quasi-two-dimensional) active region have been fabricated which have sub-mA threshold current [13], and proposed lasers with lower-dimensional quantum-confined active regions (i.e., quantum wires and quantum dots) promise enhanced modulation performance and even lower thresholds [14], [15]. Arrays of low-threshold lasers are envisioned in a future optically-interconnected computer. Furthermore, semiconductor lasers designed for mode locking can emit a continuous stream of short optical pulses at a very high repetition rate, up to 100's of GHz [16], [17]. Optical pulse trains will be useful for high-speed timing in synchronous systems, such as an optical computer or a phased-array radar.

Apart from their many applications, semiconductor lasers are intrinsically interesting from a physicist's point of view. For example, a semiconductor laser can be used as a miniature laboratory to investigate fundamental dynamics of the intra-cavity photon and carrier populations by modulating the gain and observing the lasing output. The modulated laser light can thus provide a window into the interactions taking place within the active region. The interplay between the carriers and photons in the active region is also responsible for a variety of peculiar phenomena. An example of this is the fluctuations, or noise in the laser output arising from spontaneous emission. Noise is an important practical concern because it degrades the fidelity of information encoded on the beam of light. Nevertheless, in a semiconductor laser the amplitude and phase components of the field fluctuations are strongly coupled, in

contrast to the more typical case where spontaneous emission perturbs the amplitude and phase of the lasing field independently. This coupling enhances the fundamental laser linewidth by a large factor, as is well known, but the full implications of the amplitude-phase coupling remain to be explored.

1.2 Outline of the thesis

In this thesis, experiments and accompanying theory are presented to investigate fundamental aspects of semiconductor laser modulation and noise.

Chapter 2 covers "active-layer photomixing," an experimental technique to probe the fundamental modulation response of a semiconductor laser [18]–[24]. The fundamental response is important because it depends on only a handful of basic laser parameters, such as the carrier spontaneous lifetime and the differential gain, and therefore yields insight into these parameters and the physics of lasing in semiconductors. Ordinarily, the fundamental response is not directly accessible to measurement because electrical parasitics in the device structure can dominate the measured response, especially at high frequencies. By active-layer photomixing, the fundamental modulation response of the laser can be studied independently of the parasitic response. In the technique, two laser sources with a tunable frequency difference are heterodyned in the semiconductor laser's active region. This modulates the gain, and hence the optical output, at the beat frequency of the sources. Using an equivalent circuit model for the laser diode, the optical modulation is shown to be decoupled from the parasitic circuit. The active-layer photomixing technique is used on

a GaAs/GaAlAs transverse junction stripe laser at room temperature, liquid nitrogen and liquid helium temperature, and it is verified that the modulation response appears ideal to millimeter-wave frequencies (> 30 GHz).

In chapter 3 we discuss the "gain lever," an effect which enhances the modulation efficiency of quantum well semiconductor lasers [25], [26]. The gain lever arises in a quantum well because of the special behavior of the optical gain as a function of carrier concentration. By inhomogeneously pumping the active layer, regions with unequal differential gain are created, and by modulating the region with larger differential gain the output power can be modulated with greater than unity quantum efficiency, i.e., one injected carrier can generate more than one additional lasing photon. Experiments with a GaAs/GaAlAs quantum well laser show enhanced modulation efficiency in accordance with the gain lever mechanism.

In chapter 4 the subject switches from laser modulation to laser noise with a discussion of "amplitude-phase decorrelation" [27]–[29]. Implications of the fundamental coupling between intensity noise and phase noise in semiconductor laser light are investigated. The amplitude-phase coupling causes the well-known enhancement of the fundamental laser linewidth by a factor $1+\alpha^2$, where α is the linewidth enhancement parameter, but it is shown theoretically that this inherent coupling can be exploited to reduce intensity noise below its intrinsic level by a factor of $1/(1+\alpha^2)$. When this occurs, the amplitude and phase fluctuations of the field are decorrelated. Experimentally, the decorrelation technique is applied to passively reduce intensity noise from an InGaAsP distributed feedback laser below its intrinsic level up to a factor of

28.

Because amplitude-phase decorrelation can potentially reduce intensity noise by such a large factor, it is important to determine where the reduced noise stands in relation to the fundamental shot noise floor. In chapter 5 we use a balanced homodyne detection scheme to simultaneously measure laser intensity noise and the photon shot noise level. Although the decorrelated intensity noise can be reduced to within a dB of the shot noise level, reduction below the shot noise level appears to be inhibited by uncorrelated phase noise in the instantaneous frequency fluctuation spectrum.

Work presented here is contained in the following published articles and conference proceedings [18]–[30].

Bibliography

[1] R. N. Hall, G. E. Fenner, J. D. Kingley, T. J. Soltys, and R. O. Carlson, "Coherent light emission from GaAs junctions," *Phys. Rev. Lett.*, vol. 9, pp. 366-368, 1962.

[2] M. I. Nathan. W. P. Dumke, G. Burns, F. H. Dill, Jr., and G. Lasher, "Stimulated emission of radiation from GaAs p-n junctions," *Appl. Phys. Lett.*, vol. 1, pp. 62-64, 1962.

[3] N. Holonyak, Jr. and S. F. Bevacqua, "Coherent (visible) light emission from $Ga(As_{1-x}P_x)$ junctions," *Appl. Phys. Lett.*, vol. 1, pp. 82-83, 1962.

[4] T. M. Quist, R. H. Rediker, R. J. Keyes, W. E. Krag, B. Lax, A. L. McWhorter, and H. J. Zieger, "Semiconductor maser of GaAs," *Appl. Phys. Lett.*, vol. 1, pp. 91-92, 1962.

[5] H. Kressel and J. K. Butler, *Semiconductor Lasers and Heterojunction LED's*, Orlando: Academic Press, 1977.

[6] H. C. Casey, Jr., and M. B. Panish, *Heterostructure Lasers: Part A*, Orlando: Academic Press, 1978.

[7] K. Y. Lau and A. Yariv, "Ultra-high speed semiconductor lasers," *IEEE J. Quantum Electron.*, vol. QE-21, pp. 121-138, 1985, and references therein.

[8] K. Uomi, T. Mishima, and N. Chinone, "Ultrahigh relaxation oscillation frequency (up to 30 GHz) of highly p-doped GaAs/GaAlAs multiple quantum well lasers," *Appl. Phys. Lett.*, vol. 51, pp. 78-80, 1987.

[9] T. L. Koch and U. Koren, "Semiconductor lasers for coherent optical fiber communications," *J. Lightwave Technol.*, vol. LT-8, pp. 274-293, 1990, and references

therein.

[10] K. Uomi, S. Sasaki, T. Tsuchiya, M. Okai, M. Aoki, and N. Chinone, "Spectral linewidth reduction by low spatial hole burning in 1.5 μm multi-quantum-well $\lambda/4$-shifted DFB lasers," *Electron. Lett.*, vol. 26, pp. 52-53, 1990.

[11] T. L. Koch, U. Koren, and B. I. Miller, "High performance tunable 1.5 μm InGaAs/InGaAsP multiple quantum well distributed Bragg reflector lasers," *Appl. Phys. Lett.*, vol. 53, pp. 1036-1038, 1988.

[12] M. C. Wu, Y. K. Chen, T. Tanbun-Ek, R. A. Logan, and A. M. Sergent, "Gain-levering enhanced continuous wavelength tuning (6.1 nm) in two-section strained multiquantum well DFB lasers," presented at Conf. on Lasers and Electro-Optics, May 21-25, 1990, Anaheim, CA, postdeadline paper CPDP30.

[13] K. Y. Lau, P. L. Derry, and A. Yariv, "Ultimate limit in low threshold quantum well GaAlAs semiconductor lasers," *Appl. Phys. Lett.*, vol. 52, pp. 88-90, 1988.

[14] H. Zarem, K. Vahala, and A. Yariv, "Gain spectra of quantum wires with inhomogeneous broadening," *IEEE J. Quantum Electron.*, vol. QE-25, pp. 705-712, 1989.

[15] K. Vahala, "Quantum box fabrication tolerance and size limits in semiconductors and their effect on optical gain," *IEEE J. Quantum Electron.*, vol. QE-24, pp. 523-530, 1988.

[16] K. Y. Lau, "Short-pulse and high-frequency signal generation in semiconductor lasers," *J. Lightwave Technol.*, vol. LT-7, pp. 400-419, 1989, and references therein.

[17] S. Sanders, L. Eng, J. Paslaski, and A. Yariv, "108 GHz passive mode locking of a multiple quantum well semiconductor laser with an intracavity absorber," *Appl. Phys. Lett.*, vol. 56, pp. 310-311, 1990.

[18] M. A. Newkirk and K. J. Vahala, "Parasitic-free measurement of the fundamental frequency response of a semiconductor laser by active-layer photomixing," *Appl. Phys. Lett.*, vol. 52, pp. 770-772, 1988.

[19] K. J. Vahala and M. A. Newkirk, "Measurement of the intrinsic direct modulation response of a semiconductor laser by photomixing," presented at Conf. on Lasers and Electro-Optics, April 25-29, 1988, Anaheim, CA, paper MG1.

[20] K. J. Vahala and M. A. Newkirk, "Equivalent circuit model for active-layer photomixing: Parasitic-free modulation of semiconductor lasers," *Appl. Phys. Lett.*, vol. 53, pp. 1141-1143, 1988.

[21] M. A. Newkirk and K. J. Vahala, "Low temperature measurement of the fundamental frequency response of a semiconductor laser by active-layer photomixing," presented at 11th Int. Semiconductor Laser Conf., Aug. 29 - Sept. 1, 1988, Boston, MA, postdeadline paper PD14.

[22] M. A. Newkirk and K. J. Vahala, "Low-temperature measurement of the fundamental frequency response of a semiconductor laser by active-layer photomixing," *Appl. Phys. Lett.*, vol. 54, pp. 600-602, 1989.

[23] K. J. Vahala and M. A. Newkirk, "Parasitic-free modulation of semiconductor lasers," *IEEE J. Quantum Electron.* vol. QE-25, pp. 1393-1398, 1989.

[24] M. A. Newkirk and K. J. Vahala, "Measurement of the fundamental modulation response of a semiconductor laser to millimeter wave frequencies by active-layer photomixing," *Appl. Phys. Lett.*, vol. 55, pp. 939-941, 1989.

[25] M. A. Newkirk, K. J. Vahala, T. R. Chen, and A. Yariv, "A novel gain mechanism in an optically modulated single quantum well semiconductor laser," presented at Conf. on Lasers and Electro-Optics, April 24-28, 1989, Baltimore, MD, paper WG1.

[26] K. J. Vahala, M. A. Newkirk, and T. R. Chen, "The optical gain lever: A novel gain mechanism in the direct modulation of quantum well semiconductor lasers," *Appl. Phys. Lett.*, vol. 54, pp. 2506-2508, 1989.

[27] M. A. Newkirk and K. J. Vahala, "Amplitude-phase decorrelation: A method for reducing intensity noise in semiconductor lasers," *IEEE J. Quantum Electron.*, vol. QE-27, pp. 13-22, 1991.

[28] K. J. Vahala and M. A. Newkirk, "Intensity noise reduction in semiconductor lasers by amplitude-phase decorrelation," presented at XVII Int. Quantum Electron. Conf., May 21-25, 1990, Anaheim, CA, postdeadline paper QPDP29.

[29] K. J. Vahala and M. A. Newkirk, "Intensity noise reduction in semiconductor lasers by amplitude-phase decorrelation," *Appl. Phys. Lett.*, vol. 57, pp. 974-976, 1990.

[30] M. A. Newkirk and K. J. Vahala, "Investigation of the intensity noise level of a 1.3 μm InGaAsP DFB laser by measurement with a balanced homodyne detector," presented at Opt. Fiber Comm. Conf., Feb. 18-22, 1991, San Diego, CA, paper WG3.

Chapter 2

Active-layer photomixing: Parasitic-free modulation of a semiconductor laser

2.1 Introduction

The modulation properties of semiconductor lasers are of great interest due to their importance in optical communication systems. Simply by modulating the laser's bias current, information may be written directly onto the light beam at GHz rates. The light may then be conveyed by optical fiber for tens of kilometers with very little loss. Because optical fiber has such an enormous bandwidth, on the order of THz, the capacity of the laser/fiber system is not constrained by the fiber's transmission bandwidth. For this reason, it is desirable to push the modulation bandwidth of the laser to its theoretical limit. This requires a full understanding of the physics of

high-speed modulation in semiconductor lasers.

Active-layer photomixing is an experimental technique, developed in our laboratory, to study the modulation properties of a semiconductor laser. The name "active-layer photomixing" describes the interaction of two coherent optical fields which are absorbed in the laser's active layer. The beating between the fields produces a population of electrons and holes which oscillate at the beat frequency and subsequently modulate the output power from the device. The advantage of this technique is that it allows one to probe the fundamental, or intrinsic modulation response of the laser, virtually free of device parasitics. Injection current modulation of the laser, on the other hand, is governed by a superposition of the intrinsic response and the parasitic response. At high frequencies, the modulation behavior is dominated by the electrical parasitics, masking the laser's intrinsic response.

Observation of the laser's intrinsic response function, uncontaminated by parasitic effects, provides insight into the physics of lasing in semiconductors. Agreement between the measured response and the theoretically predicted response may also justify the validity of the rate equations from which the theoretical response function is derived. We note that the modulation data in this chapter represent the first direct measurements of the fundamental modulation response of a semiconductor laser.

In this chapter, the physical principles of the active-layer photomixing technique as well as experimental results are discussed. For completeness, the fundamental modulation response of a semiconductor laser is derived from a set of rate equations for the photon and carrier populations. The parasitic-free nature of the photomixing

technique is also justified in terms of an equivalent circuit model for photomixing which may be compared to an equivalent circuit for conventional current modulation.

Three sets of experiments are described. First, the active-layer photomixing technique is used to modulate a transverse-junction stripe (TJS) laser at room temperature. Several tests of ideality are applied to the measured response, and no parasitic effects are observed. Second, the technique is used in a low-temperature experiment. A TJS laser is cooled to temperatures as low as 4.2 K and modulated by photomixing at rates up to 15 GHz. The laser is cooled for two reasons. One, semiconductor laser dynamics change in dramatic ways at low temperature. Two, the parasitic-free nature of active-layer photomixing is further demonstrated because the device parasitics become especially severe at low temperature. Finally, the response of a buried-heterostructure laser is measured to millimeter-wave frequencies (> 30 GHz). For this experiment, not only is the modulation generated optically but detected optically with a Fabry-Perot interferometer.

The semiconductor lasers used in the active-layer photomixing experiments in this chapter are GaAs/GaAlAs devices with lasing wavelengths near 0.8 μm [1]–[7]. Since the introduction of the active-layer photomixing technique, however, others have applied a related parasitic-free optical modulation technique to the study of longer wavelength InP/InGaAsP lasers [8]–[12].

2.2 The physical principles of active-layer photomixing

In this section we provide a simple picture of the physical principles of the active-layer photomixing technique. We also indicate the relationship between active-layer photomixing and ordinary optical heterodyne detection. First, the physics of photomixing must be reduced to its essentials.

2.2.1 Photomixing in a semiconductor

Consider two plane-polarized plane waves of frequencies ω_1 and ω_2, with $\omega_1 \approx \omega_2$, normally incident on a semiconductor slab. The incident electric field vector is given by

$$\mathbf{E}(t) = \mathbf{E}_1 \cos \omega_1 t + \mathbf{E}_2 \cos \omega_2 t \tag{2.2.1}$$

where for simplicity the spatial dependence is ignored and the waves are in phase at the time origin. Let the photon energies of the waves, $\hbar\omega_1$ and $\hbar\omega_2$, be greater than the bandgap energy of the material, assumed to be a direct gap semiconductor such as GaAs, so that the light is strongly absorbed. Because the dipole matrix element for the absorptive transition is isotropic, the absorption rate does not depend on the absolute orientation of the E-field vector. By Fermi's Golden Rule, the absorption rate per unit volume is a function of the square of the electric field amplitude. Electron-hole pairs are created at a rate proportional to $|\mathbf{E}(t)|^2$, and the carrier generation rate, $\pi(t)$, has a steady-state and a time-dependent part resulting from the beating of the two fields.

$$\pi(t) \propto |\mathbf{E}(t)|^2 \quad = \quad |\mathbf{E}_1 \cos \omega_1 t + \mathbf{E}_2 \cos \omega_2 t|^2$$

$$= \frac{1}{2}(|\mathbf{E}_1|^2 + |\mathbf{E}_2|^2) + \mathbf{E}_1 \cdot \mathbf{E}_2 \cos(\omega_1 - \omega_2)t. \qquad (2.2.2)$$

Components of $\pi(t)$ which oscillate at the optical frequencies ω_1, ω_2 and $\omega_1 + \omega_2$ have been temporally averaged. As shown above, the carrier generation rate is modulated at the difference frequency of the incident fields, and the strength of this modulation depends on the relative polarization of $\mathbf{E}_1$ and $\mathbf{E}_2$.

A simple two-band diagram in Fig. 2.1 shows what happens to an electron-hole pair after absorption of an input photon. Because the k quantum number of the electron is approximately conserved, and the transition energy is greater than the bandgap, the electron is sent high into the conduction band above the band-edge energy. The carriers are quite hot in comparison to the thermal energy of the system. They quickly cool to their respective band edges where they remain until they recombine.

This picture of the carrier dynamics is based on the important fact that intraband transitions occur on a much faster timescale than spontaneous interband transitions. Although these issues comprise an active area of study, for a semiconductor such as GaAs it is generally understood that intraband relaxation times are near 10^{-12} s while band-to-band spontaneous transition lifetimes are on the order of 10^{-9} s. Recent pump-probe experiments with ultrashort laser pulses in GaAs have measured separate relaxation times for hot electrons as they cool to the electron temperature (0.3×10^{-12} s) and to the lattice temperature (1.5×10^{-12} s) [13]. In comparison to timescales relevant to this thesis, these intraband relaxation processes are practically instantaneous. Consequently, the carrier pool within each band maintains thermal equilibrium even though the electron and hole populations may not be in thermal

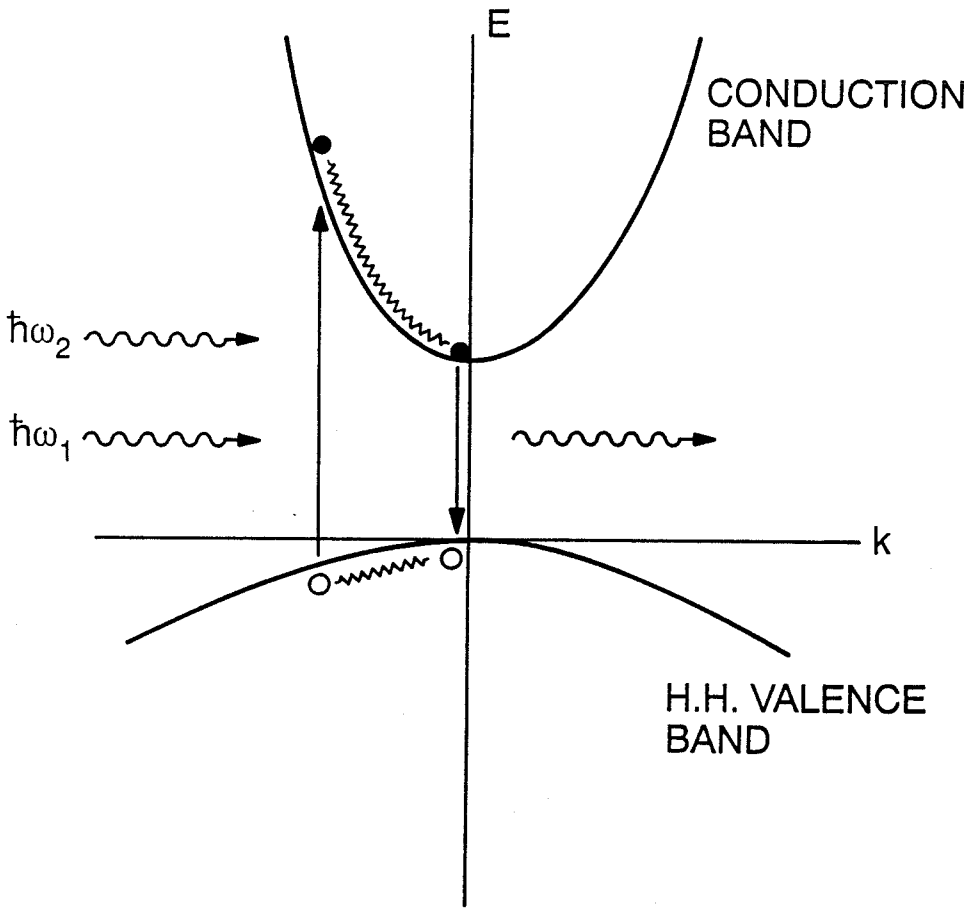

Figure 2.1: Sequence of events in a direct-gap semiconductor when a photon is absorbed. An electron is excited high into the conduction band and rapidly decays to the band edge. The hole similarly relaxes to the valence band edge. When two fields at frequencies ω_1 and ω_2 are incident, the carrier transition rate is modulated at the beat frequency $\omega_1 - \omega_2$.

equilibrium with each other. This is the conventional justification for a description of the carrier populations based on quasi-Fermi levels.

In equilibrium, the occupancy of states in a given band is governed by the Fermi distribution. The electron concentration is given by

$$N = \int_{-\infty}^{+\infty} \rho_c(E - E_c) f_c(E)\, dE \tag{2.2.3}$$

where $\rho_c(E)$ is the density of states in the conduction band, E_c is the energy of the band edge, and f_c is the Fermi factor, defined as

$$f_c(E) = \frac{1}{e^{(E-F_c)/k_BT} + 1}. \tag{2.2.4}$$

Here, F_c is the quasi-Fermi level for the conduction band, k_B is Boltzmann's constant, and T is the temperature of the crystal lattice. We see that, for T constant, if N changes by optical pumping or some other means, then the quasi-Fermi level must also change.

Returning to (2.2.2) and Fig. 2.1, it is clear that the carrier population is coherent with the generation rate $\pi(t)$, since the photo-excited carriers tumble down the band and rapidly equilibrate with the carrier pool. Equivalently, the quasi-Fermi level F_c in (2.2.4) is coherent with $\pi(t)$. Of course, we must assume that the inverse beat frequency of the mixing fields, $1/(\omega_1 - \omega_2)$, is much less than the intraband relaxation time. From the above discussion, this condition may be satisfied for beat frequencies approaching 100 GHz. Thus, by photomixing two coherent fields in a semiconductor, it is possible to drive the carrier populations at ultra-high frequencies while maintaining thermal equilibrium within each carrier pool.

2.2.2 What is active-layer photomixing?

Active-layer photomixing is a clean, optical technique to probe the fundamental lasing dynamics of a semiconductor laser. In active-layer photomixing, the coherent input fields described above are selectively mixed in a semiconductor laser's active region. Because optical gain in a semiconductor is a function of the carrier population, the technique provides a means to high-frequency modulate the gain by driving the carriers at the beat frequency. This allows one to study the fundamental dynamics of the interaction between the gain and the lasing mode of the semiconductor laser.

Clearly, the benefits of optical modulation are (1) the modulation may be generated at arbitrarily high frequency by tuning the beat frequency of the mixing sources, and (2) the carriers are produced directly in the active region where they immediately influence the optical gain. In addition, by bringing the mixing beams to a point focus it becomes possible to locally modulate the carrier density over a small portion of the laser's active region. In fact, by point modulating a semiconductor laser with a quantum-well active layer, a new gain mechanism was discovered—the "gain lever"—which is the topic of chapter 3. Active-layer photomixing is therefore a unique tool with which to study semiconductor laser dynamics.

2.2.3 Relationship to heterodyne detection

Active-layer photomixing may be viewed as a relative of ordinary optical heterodyne detection. Both methods involve the mixing of two coherent optical fields to generate a response at the difference frequency. In a typical heterodyne detection scheme, the

two fields are absorbed in the intrinsic region of a *p-i-n* photodiode. The oscillating carrier population is swept from the generation volume with a static electric field, and the beating between the input fields modulates the photocurrent at the difference frequency. This is illustrated in Fig. 2.2, where the photocurrent spectrum is given by a peak at $\omega_1 - \omega_2$. The essential feature is that the mixing of the light creates carriers which are coupled out of the detector as a modulated current. In active-layer photomixing, by constrast, the two fields are mixed in a laser diode's active region where, because the intrinsic impedance of the active region is very small (see section 2.4), the photocarriers remain to modulate the optical gain. So far the modulation has not been recovered. But because the semiconductor laser is above threshold, the oscillating gain remodulates the semiconductor laser output at the beat frequency $\omega_1 - \omega_2$. Assuming that the device is lasing at a single frequency ω_L, the result is that sidebands are generated at $\omega_L \pm (\omega_1 - \omega_2)$ (see Fig. 2.2). In this sense the beat frequency of the input fields has been detected through the appearance of sidebands on the optical carrier.

2.3 The fundamental modulation response of a semiconductor laser

The starting point for treatment of the modulation response of a laser diode is the pair of single-mode spatially-averaged rate equations for photon density in the lasing mode, P, and carrier density in the active region, N. For above-threshold operation,

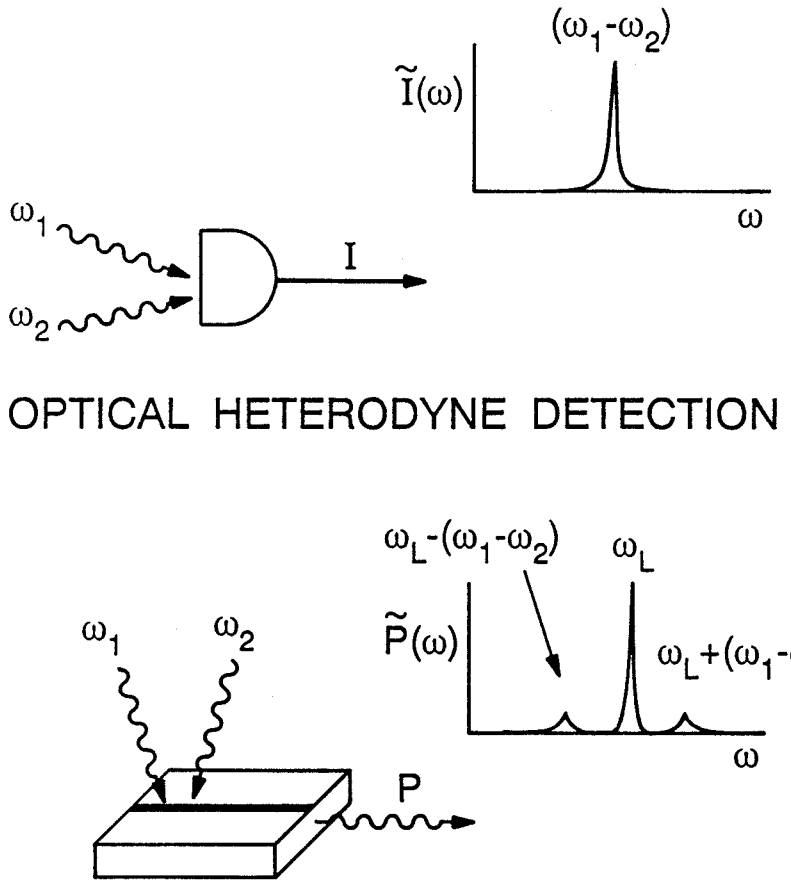

Figure 2.2: Similarity between active-layer photomixing and optical heterodyne detection. Heterodyning two fields on a detector modulates the photocurrent at the beat frequency, while active-layer photomixing generates sidebands on the lasing frequency.

the rate equations may be written as [14]

$$\frac{d}{dt}P = \Gamma G(N,P)P - \frac{P}{\tau_p} + \Theta \tag{2.3.1}$$

$$\frac{d}{dt}N = -G(N,P)P - R(N) + \Pi \tag{2.3.2}$$

where G is the optical gain, Γ is the mode confinement factor, τ_p is the photon lifetime, Θ is the spontaneous emission rate into the lasing mode per unit volume, R is the carrier spontaneous recombination rate per unit volume, and Π is the pumping rate in units of carrier density per second.

Some of these terms need to be clarified. The gain, G, is not only a function of the inversion, N, but of photon density as well. This accounts for power-dependent mechanisms which tend to reduce the gain as mode power increases (non-linear gain) [15], [16]. Because the active region is usually smaller than the lasing mode volume, the confinement factor, Γ (< 1), is needed to account for the incomplete spatial overlap. The photon lifetime, τ_p, is defined as

$$\frac{1}{\tau_p} = \frac{c}{n_l}\left(\alpha_i + \frac{1}{L}\ln(\frac{1}{r})\right) \tag{2.3.3}$$

where c is the speed of light, n_l is the refractive index of the active layer, L is the cavity length, and r is the facet reflectivity. τ_p measures the damping of the photon population due to (useful) facet loss and internal loss, α_i, such as waveguide scattering and free-carrier absorption.

The rate equations are linearized by first decomposing the dynamic variables $N(t)$, $P(t)$, and $\Pi(t)$ into a steady-state part and a small, time-varying part

$$P(t) = P_o + p(t) \text{ where } p(t)/P_o \ll 1 \text{ , etc.} \tag{2.3.4}$$

$$N(t) = N_o + n(t) \tag{2.3.5}$$

$$\Pi(t) = \Pi_o + \pi(t). \tag{2.3.6}$$

Then, the gain and spontaneous recombination rate are Taylor expanded to first order about the operating point (P_o, N_o).

$$\begin{aligned} G(N(t),P(t)) &= G(N_o,P_o) + n(t)\frac{\partial}{\partial N}G(N,P_o)\Big|_{N=N_o} + p(t)\frac{\partial}{\partial P}G(N_o,P)\Big|_{P=P_o} \\ &= G_o + n(t)g_n + p(t)g_p \end{aligned} \tag{2.3.7}$$

$$\begin{aligned} R(N(t)) &= R(N_o) + n(t)\frac{d}{dN}R(N)\Big|_{N=N_o} \\ &= R_o + \frac{n(t)}{\tau_{sp}} \end{aligned} \tag{2.3.8}$$

Here, g_n is the differential gain, g_p is the non-linear gain, and τ_{sp} is the carrier spontaneous lifetime. Substituting these expansions into the rate equations, and neglecting products of small-signal quantities, the following time-independent equations are found

$$\Gamma G_o P_o - \frac{P_o}{\tau_p} + \Theta = 0 \tag{2.3.9}$$

$$-G_o P_o - R_o + \Pi_o = 0. \tag{2.3.10}$$

Equation (2.3.9) shows the familiar gain clamping condition whereby the steady-state modal gain ΓG_o equals the loss plus a contribution from spontaneous emission. Often the spontaneous term may be neglected. Equation (2.3.10) shows that the laser power above threshold varies linearly with pumping rate. Continuing, we also find the small-signal rate equations

$$\frac{d}{dt}p = \Gamma(G_o + g_p P_o)p + \Gamma g_n P_o n - \frac{p}{\tau_p} \tag{2.3.11}$$

$$\frac{d}{dt}n = -g_n P_o n - (G_o + g_p P_o)p - \frac{n}{\tau_{sp}} + \pi \tag{2.3.12}$$

which may be Fourier transformed with respect to frequency Ω to yield the small-signal modulation response. In matrix form, the transformed equations are

$$\begin{pmatrix} (\Gamma G_o + \Gamma g_p P_o - \frac{1}{\tau_p} + i\Omega) & \Gamma g_n P_o \\ -(G_o + g_p P_o) & -(g_n P_o + \frac{1}{\tau_{sp}} - i\Omega) \end{pmatrix} \begin{pmatrix} \tilde{p}(\Omega) \\ \tilde{n}(\Omega) \end{pmatrix} = \begin{pmatrix} 0 \\ -\tilde{\pi}(\Omega) \end{pmatrix}.$$

Inverting the 2×2 matrix gives

$$\begin{pmatrix} \tilde{p}(\Omega) \\ \tilde{n}(\Omega) \end{pmatrix} = \begin{pmatrix} \Gamma g_n P_o \\ -(\Gamma G_o + \Gamma g_p P_o - \frac{1}{\tau_p} + i\Omega) \end{pmatrix} \frac{\tilde{\pi}(\Omega)}{D(\Omega)}$$

where the resonant denominator, $D(\Omega)$, is a lengthy expression.

$$D(\Omega) = -\Omega^2 - i\Omega(g_n P_o + \frac{1}{\tau_{sp}} - \Gamma G_o - \Gamma g_p P_o + \frac{1}{\tau_p}) + \frac{g_n P_o}{\tau_p} - \frac{1}{\tau_{sp}}(\Gamma G_o + \Gamma g_p P_o - \frac{1}{\tau_p}). \tag{2.3.13}$$

$D(\Omega)$ may be simplified using the gain clamping condition (2.3.9) and the fact that the $(\Gamma g_p P_o)/\tau_{sp}$ term may be neglected in comparison to the $(g_n P_o)/\tau_p$ term (for a laser with a typical 300 μm cavity length, the carrier spontaneous lifetime is 2–3 orders of magnitude greater than the photon lifetime, whereas $g_n \sim \Gamma g_p$). As a result,

$$D(\Omega) = -\Omega^2 - i\Omega(g_n P_o + \frac{1}{\tau_{sp}} - \Gamma g_p P_o + \frac{\Theta}{P_o}) + \frac{g_n P_o}{\tau_p} \tag{2.3.14}$$

The small-signal modulation response functions for the photon density and carrier density may then be written compactly in their final form.

$$\tilde{p}(\Omega) = \frac{\Gamma g_n P_o}{\omega_R^2 - \Omega^2 - i\gamma\Omega} \tilde{\pi}(\Omega) \tag{2.3.15}$$

$$\tilde{n}(\Omega) = \frac{-(\Gamma g_p P_o - \frac{\Theta}{P_o} + i\Omega)}{\omega_R^2 - \Omega^2 - i\gamma\Omega} \tilde{\pi}(\Omega) \tag{2.3.16}$$

where ω_R, the relaxation oscillation resonance frequency, and γ, the relaxation oscillation damping rate, are defined as

$$\omega_R = \sqrt{\frac{g_n P_o}{\tau_p}} \tag{2.3.17}$$

$$\gamma = \frac{1}{\tau_{sp}} + \frac{\Theta}{P_o} + (g_n - \Gamma g_p) P_o. \tag{2.3.18}$$

The response functions (2.3.15) and (2.3.16) are fundamental in the sense that they stem from the basic laser dynamics as modeled by the rate equations. These functions therefore yield insight into the physics of lasing in semiconductors. Because the cavity photon density is directly proportional to the laser output power, $\tilde{p}(\Omega)$ governs the fundamental modulation properties of the laser output. Equation (2.3.15) shows that $\tilde{p}(\Omega)$ is equivalent to the response of a damped harmonic oscillator. Important features of (2.3.15) are: The response is flat at low frequencies, there is a resonance at the natural frequency of the coupled photon/carrier system (the relaxation resonance, ω_R [23]), the width of the resonance is governed by the damping, γ, and the response decays as $1/\Omega^2$, or 20 dB/dec, beyond the resonance.

The response function for the carrier density (2.3.16) is similar to $\tilde{p}(\Omega)$, as they share the same resonant denominator. The low-frequency behavior is quite different, however, because of the $i\Omega$ term in the numerator. If not for the g_p term, at high output power the carrier density would be perfectly clamped near dc (i.e., $\tilde{n} \rightarrow 0$). At high frequencies beyond the resonance, the carrier and photon populations are in quadrature. Equation (2.3.16) will be used later for evaluating the intrinsic impedance of the laser diode.

In the laboratory, modulated semiconductor laser light is detected with a photo-

diode, and the ac photocurrent power from the detector is measured as a function of frequency with an electronic microwave spectrum analyzer. Consequently, what is measured is proportional to $|\tilde{p}(\Omega)|^2$. From (2.3.15), the measured intensity modulation response of the laser is given by

$$\left|\frac{\tilde{p}(\Omega)}{\tilde{\pi}(\Omega)}\right|^2 = \frac{(\Gamma g_n P_o)^2}{(\omega_R^2 - \Omega^2)^2 + \gamma^2\Omega^2}. \tag{2.3.19}$$

Figure 2.3 shows a calculated response function for a GaAs/GaAlAs semiconductor laser (the transverse junction stripe laser discussed in the following sections) at two different bias levels. The response is normalized by its low-frequency value. As output power increases, the resonance frequency moves out to higher frequencies, in accordance with (2.3.17). One important feature of the fundamental response $|\tilde{p}(\Omega)|^2$ is that it eventually rolls off as $1/\Omega^4$, or 40 dB/dec at high frequencies beyond the resonance.

From an optical communications standpoint, ω_R serves as the definition of the practical modulation bandwidth of a semiconductor laser. It is therefore desirable to increase ω_R as much as possible. From (2.3.17), we see that ω_R depends on three parameters, differential gain, photon density, and photon lifetime. Much progress has been made in extending ν_R ($= \omega_R/(2\pi)$) beyond 10 GHz by the use of multiple quantum well active layers to increase g_n [17], [18], window structures or tight optical confinement to increase P_o [19], [20], and short cavity lengths to reduce τ_p [21], [22].

The overall shape of the fundamental response $|\tilde{p}(\Omega)|^2$ is characterized by just two parameters, the relaxation resonance frequency, ω_R, and the damping rate, γ. Both of these parameters may easily be determined from the resonance peak of the ideal

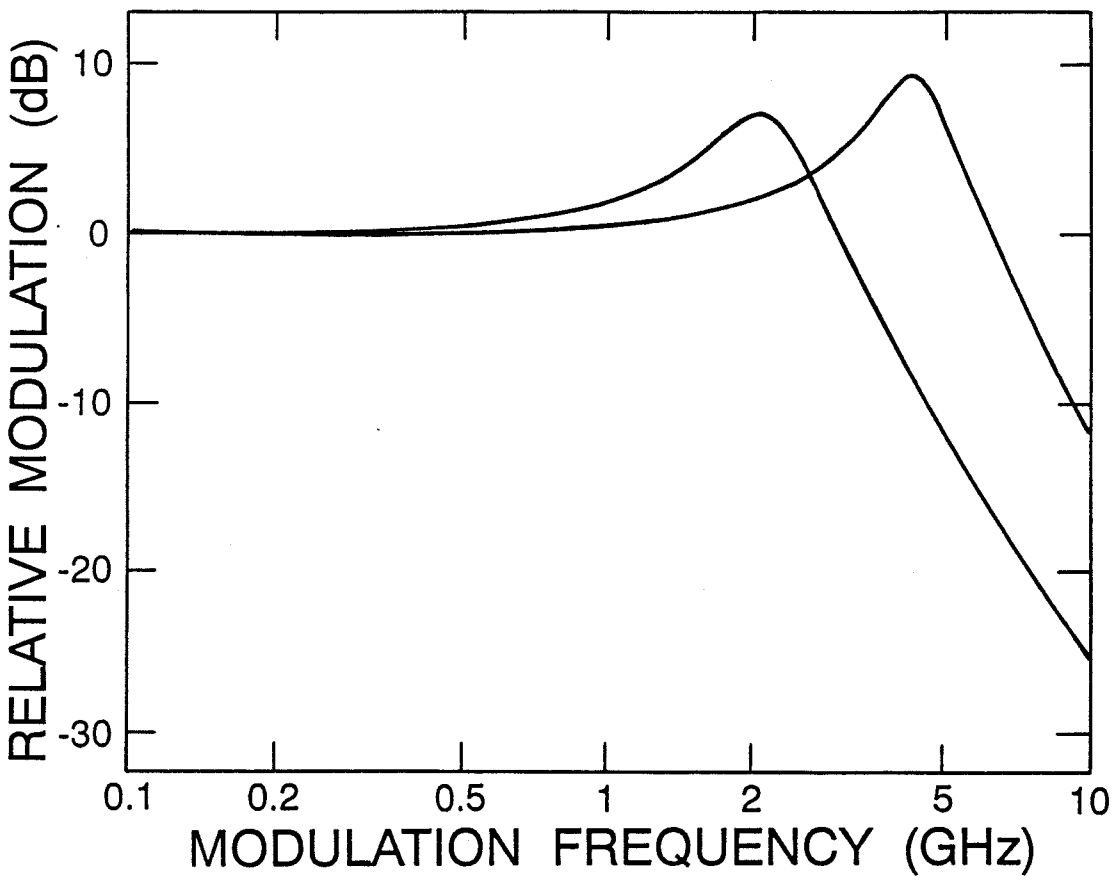

Figure 2.3: Calculated fundamental modulation response $|\tilde{p}|^2$ for a GaAs/GaAlAs TJS laser at two different bias levels (1.17 I_{th} and 1.54 I_{th}, where I_{th} is the threshold current). The resonance moves out to higher frequencies as a function of laser bias. The response decays at 40 dB/dec beyond the resonance.

response function. If the resonance reaches its maximum value at the frequency Ω_{max} with relative height $|\tilde{p}(\Omega_{max})/\tilde{p}(0)|^2$, then

$$\omega_R^2 = \frac{\Omega_{max}^2}{\sqrt{1 - \left|\frac{\tilde{p}(0)}{\tilde{p}(\Omega_{max})}\right|^2}} \tag{2.3.20}$$

and the damping rate is found from

$$\gamma^2 = 2(\omega_R^2 - \Omega_{max}^2). \tag{2.3.21}$$

By extracting ω_R and γ from a series of response curves at different laser bias levels, the dependence of these parameters on output power can be compared with theory. From (2.3.17) and (2.3.18), ω_R and γ can be reexpressed as

$$\omega_R^2 = \frac{g_n P_o}{\tau_p} \tag{2.3.22}$$

$$\gamma = \frac{1}{\tau_{sp}} + \frac{\Theta}{P_o} + \tau_p \omega_R^2 (1 + \frac{\Gamma |g_p|}{g_n}) \tag{2.3.23}$$

$$= \gamma_o + \tau_p \omega_R^2 (1 + \frac{\Gamma |g_p|}{g_n}). \tag{2.3.24}$$

where γ_o is a power-independent contribution to the damping (the Θ/P_o term is negligible except for operation very near threshold). It can be seen that ω_R^2 is a linear function of laser output power, whereas γ is expressible as a linear function of ω_R^2.

In addition to spontaneous and stimulated recombination, the carrier density in the active region may be damped by diffusion and other effects [24]. Although such mechanisms were not explicitly included in the original set of rate equations(2.3.1) and (2.3.2), additional independent damping rates may easily be incorporated in the power-independent spontaneous damping term, γ_o, to account for all sources of damping to the carrier population.

In summary, the rate equations predict that the fundamental modulation response of the laser diode (2.3.19) is flat at low frequencies, has a damped resonance near the relaxation oscillation frequency, ω_R, and eventually rolls off at 40 dB/dec beyond the resonance. In addition, ω_R^2 is a linear function of laser power, and the damping rate, γ is a linear function of ω_R^2. All of these features can be used to test the ideality of the measured response function when the laser is modulated by the active-layer photomixing technique.

2.4 Active-layer photomixing vs. conventional current modulation: Equivalent circuit model

When directly modulating the current to the laser diode, electrical parasitics in the device packaging and the laser structure will divert modulation current from the active region. The response of the laser to conventional current modulation is thus a superposition of the fundamental response, given above, and the parasitic response. The fundamental modulation response is therefore obscured by the parasitic loading, especially at high frequencies.

In this section we show that, unlike conventional current modulation, active-layer photomixing is a parasitic-free modulation technique. By modeling the laser diode in terms of an equivalent electrical circuit [3], including an equivalent impedance for the active region, it will be seen that the modulation generated by the photomixing is effectively decoupled from the parasitic circuit at all frequencies.

2.4.1 Equivalent circuit for conventional current modulation

The fundamental response $\tilde{p}(\Omega)/\tilde{\pi}(\Omega)$ (2.3.15) is the reponse of the photon density to modulation of the carrier density in the active-region. The conventional means for applying the modulation is through modulation of the laser's bias current. However, electrical parasitics will influence the degree to which the injection current modulation translates into carrier density modulation. In other words, the pumping rate $\Pi(t)$ in (2.3.2) is a function of the bias current $I(t)$ flowing to the device which must additionally drive an external parasitic circuit not accounted for in the rate equations. In the frequency domain, the small-signal quantities are related by

$$\tilde{\pi}(\Omega) = H_{RC}(\Omega)\tilde{\imath}(\Omega) \tag{2.4.1}$$

where $H_{RC}(\Omega)$ is the parasitic response function. The response function for conventional current modulation, $\tilde{p}(\Omega)/\tilde{\imath}(\Omega)$, is thus a *superposition* of the fundamental response and the parasitic response. That is,

$$\frac{\tilde{p}(\Omega)}{\tilde{\imath}(\Omega)} = H_{RC}(\Omega)\frac{\Gamma g_n P_o}{\omega_R^2 - \Omega^2 - i\gamma\Omega}. \tag{2.4.2}$$

The fundamental response is thus obscured by the parasitics, especially at high frequencies. For an example of how parasitics may dominate the measured response function, see [25].

The parasitic circuit is a combination of many things. Among them are the inductance of the bond wire, series resistance and capacitance of the contact layer, and the capacitance of the p-n junction's depletion region. Some of these impedances may be reduced by careful design of the laser and mount. However, they can only be reduced

so far. For instance, the depletion layer capacitance is unavoidable because the p-n junction is integral to the structure of a laser diode.

An equivalent circuit for conventional current modulation of the laser diode is shown in Fig. 2.4. The current source $\tilde{i}(\Omega)$ is coupled into the circuit through the bond wire. The laser's active region is represented by an equivalent impedance, $Z(\Omega)$, discussed below. It can be seen that there are parasitic paths through the depletion capacitance C_D and contact-layer capactance C which divert current around the active layer. Typical values for the parasitic impedances are $R = 10\ \Omega$, $C = 10$ pF, $C_D = 10$ pF, and $L = 1$ nH. Because $|Z(\Omega)|$ is extremely small (see below), by inspection of the figure the parasitic response is primarily governed by the parallel combination of the contact layer capacitance, C, and resistance, R. The corner frequency of this RC circuit is about 1.6 GHz for the values given above. Reductions in C, and improvements in the parasitic corner frequency, have been obtained for devices on semi-insulating substrates [26]. Nevertheless, even for optimal tailoring of the parasitics, there will always be some high-frequency cut-off beyond which the parasitic response dominates the modulation response of the laser.

2.4.2 Intrinsic impedance of the laser diode

In order to model the semiconductor laser by an equivalent circuit, it is useful to describe the laser diode by an effective impedance [27]. This impedance is given by $Z(\Omega) = \tilde{v}(\Omega)/\tilde{i}_L(\Omega)$ where $\tilde{v}$ is the small-signal voltage amplitude across the junction, i.e., the quasi-Fermi level separation, and $\tilde{i}_L$ is the small signal injection current amplitude into the active region. The voltage is related to the carrier density $\tilde{n}(\Omega)$

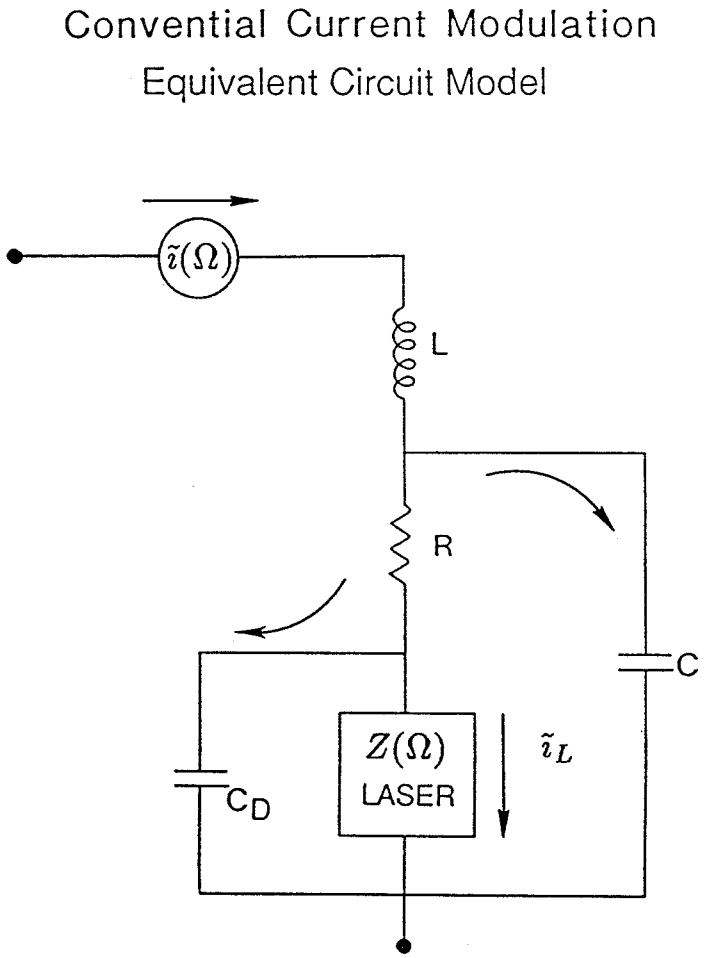

Figure 2.4: Equivalent circuit model for conventional current modulation of a laser diode. The active region is represented by an effective impedance $Z(\Omega)$.

(2.3.16) by the following expression [28]

$$\tilde{v}(\Omega) = \frac{M k_B T}{q} \frac{\tilde{n}(\Omega)}{N_o} \tag{2.4.3}$$

where k_B is Boltzmann's constant, T is the lattice temperature, q is the electron charge, N_o is the average carrier density, and M is given by

$$M = 2 + \frac{N_o}{2\sqrt{2}} \left(\frac{1}{N_v} + \frac{1}{N_c} \right). \tag{2.4.4}$$

Here, N_v and N_c are the effective density of states for the valence and conduction band, respectively.

Using $\tilde{\imath}_L(\Omega) = qV\tilde{\pi}(\Omega)$, where V is the active region volume, the intrinsic impedance is

$$Z(\Omega) = \frac{M k_B T}{q^2 V N_o} \frac{\frac{\Theta}{P_o} - \Gamma g_p P_o - i\Omega}{\omega_R^2 - \Omega^2 - i\gamma\Omega} \tag{2.4.5}$$

Using values for g_p, ω_R, and γ measured for a GaAs transverse junction stripe laser discussed below, $|Z(\Omega)|$ is plotted in Fig. 2.5 for several photon densities corresponding to output powers from 0.5 mW to 10 mW. $|Z(\Omega)|$ peaks at the relaxation resonance frequency, but overall the impedance is rather small. At low frequencies, $|Z(\Omega)|$ is on the order of 10's of milli-Ohms. Intuitively, the intrinsic impedance is small because the gain saturation impels the carrier density to clamp to its threshold value. The junction voltage is therefore clamped, giving rise to a small impedance. The finite impedance at low frequency in Fig. 2.5 results primarily from the nonlinear gain term g_p. If this term were absent, then the low-frequency impedance at high output power would approach zero.

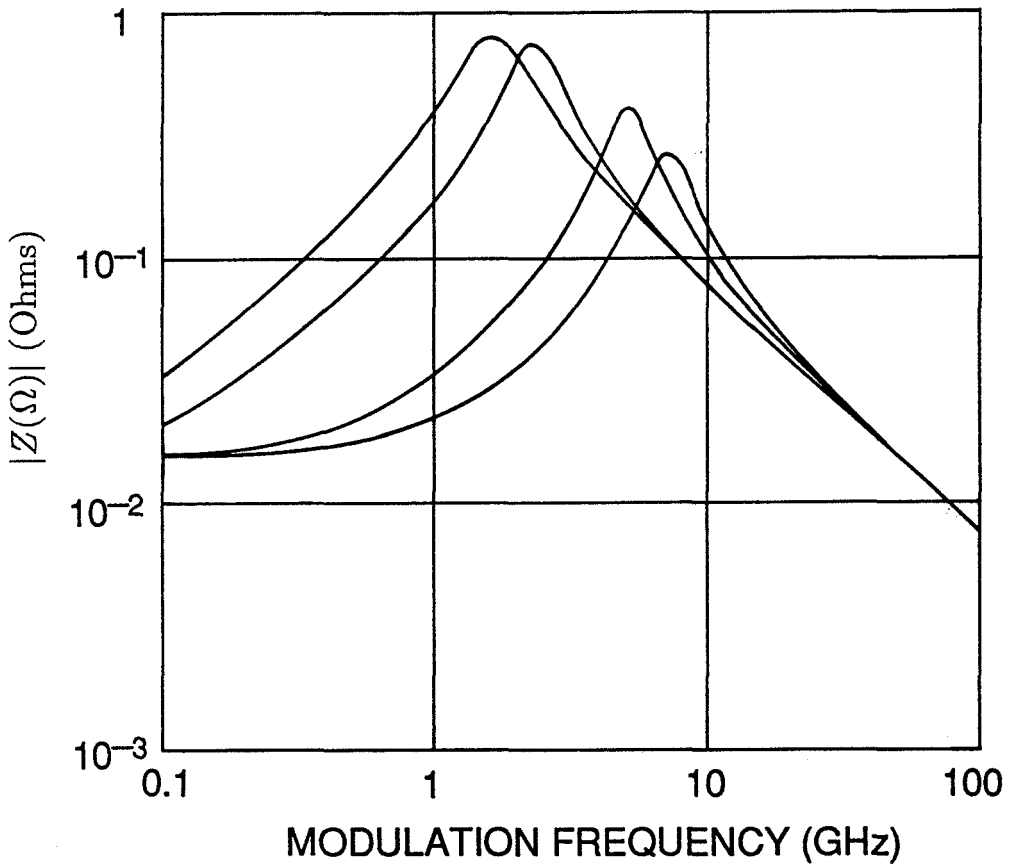

Figure 2.5: Intrinsic impedance of the laser diode vs. frequency. Characteristics correspond, from left to right, to output powers of 0.5, 1.0, 5.0 and 10 mW per facet.

2.4.3 Equivalent circuit for active-layer photomixing

As shown below, the advantage of active-layer photomixing is that the laser can be modulated nearly independently of the parasitics. Initially, this may appear obvious because the carriers are optically generated directly in the active region instead of being injected from the outside world. No matter how the carrier population is being modulated, however, an oscillating carrier density implies that the separation between the quasi-Fermi levels, and hence the junction voltage, is also oscillating (see (2.2.4)). We must therefore evaluate how this voltage interacts with the parasitic circuit before we may claim that the active-layer photomixing technique is parasitic-free.

An equivalent circuit model for active-layer photomixing is shown in Fig. 2.6. The parasitic circuit is identical to Fig. 2.4, but for photomixing the optical modulation within the active region is equivalent to a current source $\tilde{\imath}(\Omega)$ across the intrinsic impedance $Z(\Omega)$. Parasitic current paths through the contact-layer resistance and depletion capacitance are shown in the figure. Because $|Z(\Omega)| \ll R$, the only potential source of any significant parasitic loading is through C_D. The impact of this loading can be measured by the following transfer function,

$$\frac{\tilde{\imath}_L}{\tilde{\imath}} = \frac{1}{1 + i\Omega C_D Z(\Omega)}. \tag{2.4.6}$$

Figure 2.7 shows $|\tilde{\imath}_L/\tilde{\imath}|$ for two laser power levels and several values of C_D. The impact of parasitics on the active-layer photomixing modulation is evident near the relaxation resonance frequency, but only for large C_D is any capacitive loading apparent. At higher modulation frequencies beyond the resonance the small amount of parasitic loading is actually diminished, in contrast to conventional current modulation where

the parasitics only become worse at higher modulation frequencies. For the laser diode discussed below, C_D is estimated to be less than 10 pF. From the figure, we see that for $C_D \leq 10$ pF, the optical modulation generated by active-layer photomixing is effectively decoupled from the parasitic circuit at all frequencies.

2.5 Experimental implementation of active-layer photomixing

In order to perform active-layer photomixing in a semiconductor laser, there are some basic experimental requirements which must be met. First of all, two single-frequency lasers are needed for the photomixing sources, and at least one of them must be tunable. Returning to Fig. 2.1, it is apparent that the optical frequency of the mixing beams is not critical so long as the photon energy exceeds the band gap energy of the semiconductor material in the active layer. However, it is often preferable to photomix through the top surface of the laser diode. This is possible because in a conventional buried heterostructure semiconductor laser, the active region is surrounded by higher bandgap material in order to confine the carriers and to guide the optical mode. For surface pumping, the mixing light is thus constrained to a range of photon energies where the active region is absorbing but the overlying material is transparent. Alternatively, the active region may be optically modulated through one of the facets. Because the mixing light is strongly absorbed, however, this approach accelerates facet degradation which may lead to premature failure of the device under study.

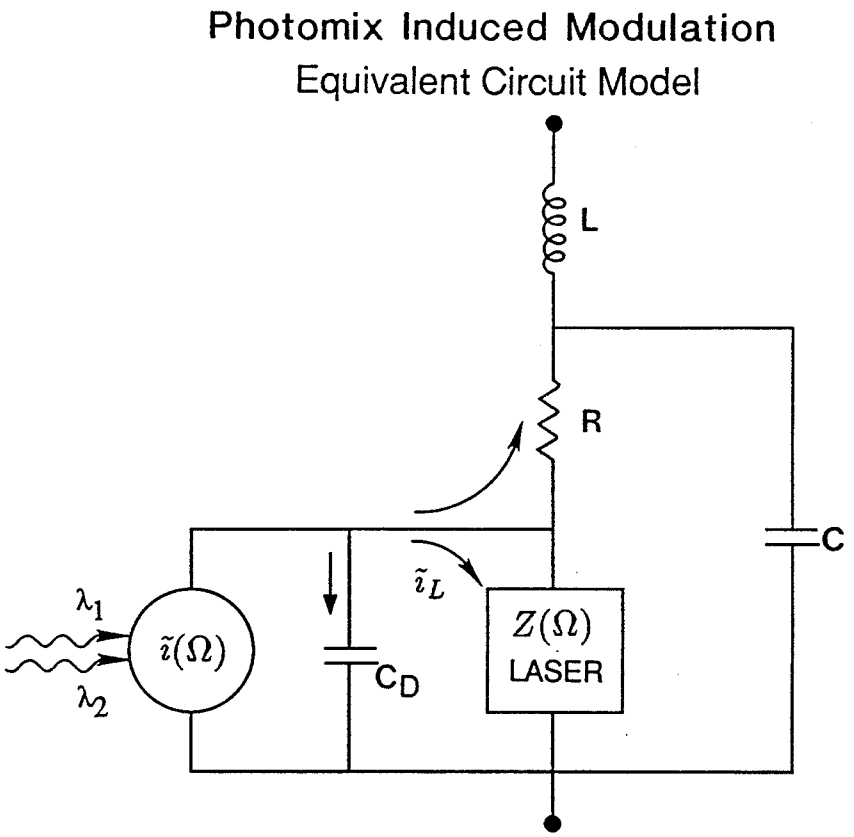

Figure 2.6: Equivalent circuit model for modulation of a laser diode by active-layer photomixing .

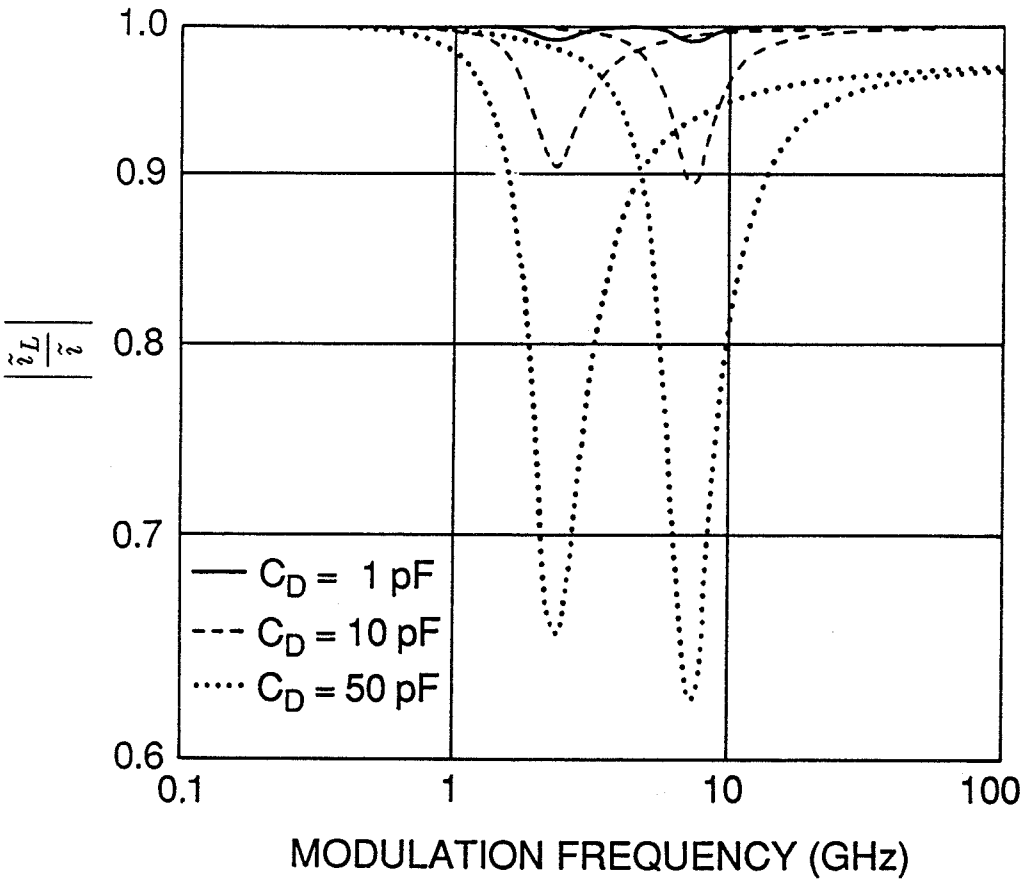

Figure 2.7: Loading of active-layer photomixing modulation by the depletion layer capacitance for several values of C_D. Characteristics are shown for laser output powers of 1 mW (low-frequency dip) and 10 mW (higher-frequency dip).

A typical experimental setup for active-layer photomixing is shown in Fig. 2.8. The photomixing sources are provided by a Kr ion laser and a tunable dye laser. Either the Kr line at 752.5 nm or 676.4 nm was used at different times for surface pumping a GaAs/GaAlAs laser diode. These two Kr wavelengths satisfy the need for absorption in the GaAs active layer and transmission through the surrounding GaAlAs. The dye laser, pumped by an Ar ion laser, operates at these wavelengths by running either Pyridine 2 or DCM laser dye, respectively.

Both lasers are single frequency. The Kr laser is forced to run single frequency by an intra-cavity etalon, while the dye laser has multiple intra-cavity etalons and a tunable birefringent filter. The free-running Kr laser maintains an effective linewidth of about 20 MHz, which is caused by mechanical vibrations in the resonator, primarily from cooling water flow. The dye laser, on the other hand, is electronically locked to an external cavity, maintaining an rms linewidth of 500 kHz. Since the two lasers are independent of each other, the beatnote spectrum is dominated by the jitter in the Kr lasing frequency, giving a beatnote linewidth of about 20 MHz. The dye laser frequency may be electronically scanned continously over 30 GHz without mode hopping.

The two laser outputs are focused into single-mode optical fibers. A 50/50 fiber coupler is then used to combine the mixing beams into the same fiber. Initial overlap of the two frequencies is accomplished by first directing the output from one arm of the fiber coupler into a 0.75 m grating spectrometer. The dye laser is mode jumped until the two laser frequencies fall within 10 GHz, the resolution of the spectrometer. We

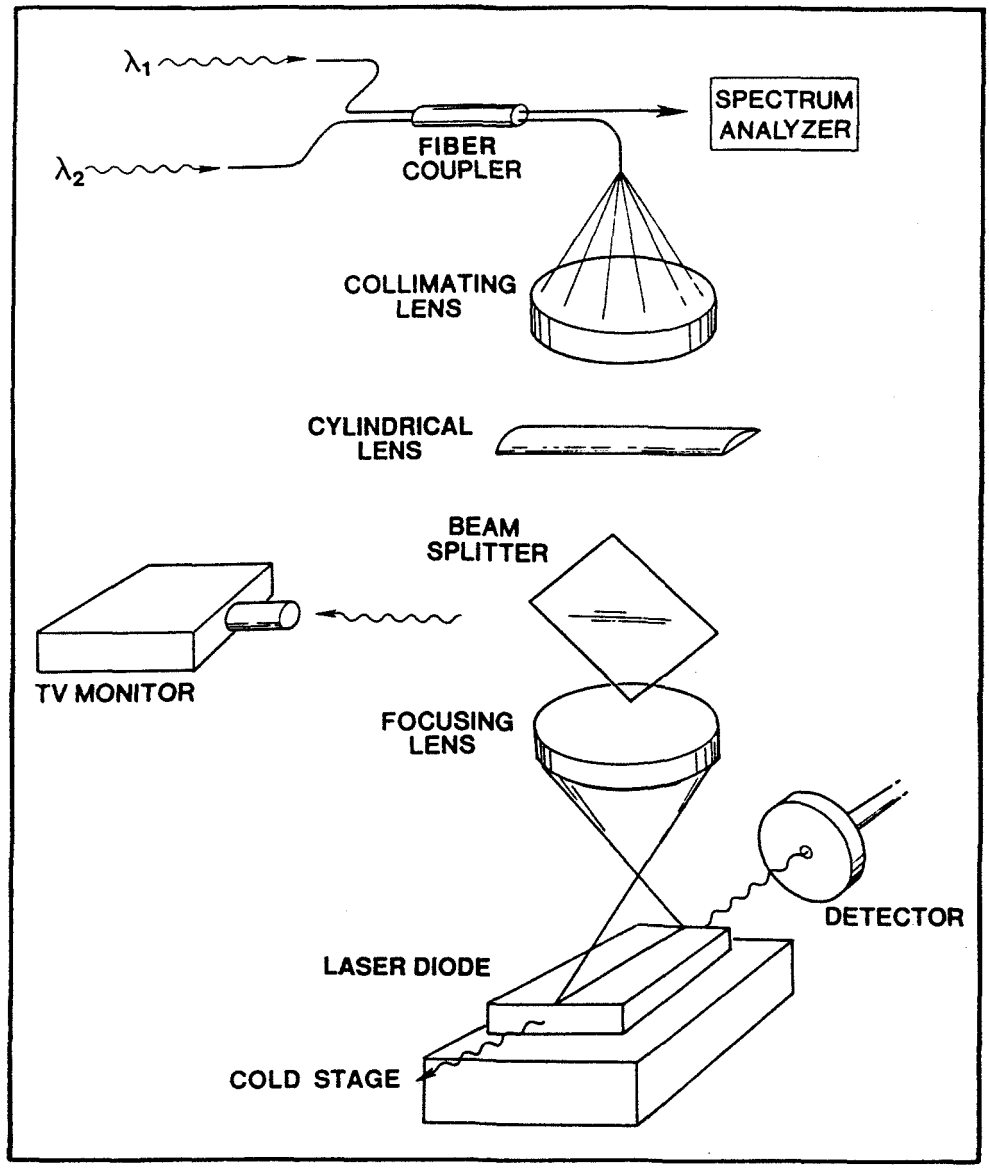

Figure 2.8: Schematic diagram of the experimental arrangement for modulation of a semiconductor laser by active-layer photomixing.

then illuminate a photodiode with the mixed light and scan the dye laser frequency until the beat frequency falls within the bandwidth of the photodiode. A beatnote in the photocurrent then appears on an electronic spectrum analyzer. The dye laser scan offset is then adjusted until the beat frequency can be continuously scanned from 0 to 30 GHz. Of course, higher beat frequencies are obtained simply by mode jumping the dye laser.

So that the maximum power is available for optical modulation (see (2.2.2)), the polarizations of the mixing beams need to be aligned at the output of the fiber coupler. In our experiment, the relative polarization is controlled by squeezing one of the input fibers between two metal plates using a PZT. The polarization can be rotated in this way because a single mode fiber becomes birefringent when stressed [29].

A *p-i-n* photodiode is used to detect the intensity modulation of the semiconductor laser. Of course, the measured response of the laser diode will be superposed with the frequency response of the detector. However, a side benefit of the active-layer photomixing technique is that the mixing beams may first be used to accurately calibrate the response of the detector by heterodyning the beams on the detector and scanning the beat frequency [30], [31]. The detector response may then be factored out of the measured laser diode response.

Efficient coupling of the mixing light into the narrow ($\sim$ 3 μm) active region of a laser diode proved to be experimentally challenging. A video camera with an infrared-sensitive vidicon is used to image the top surface of the laser diode on a CRT. The camera, in conjunction with a microscope objective lens, serves as a video

microscope. First, the laser is slightly forward biased so that the luminescent stripe from the active region is visible. Because of the beam splitter, the back reflected mixing light is also visible, and this enables rough alignment of the pump light into the active region. Then, the bias voltage to the laser is turned off, and the pump focus is adjusted to maximize the dc photocurrent in the biasing circuit induced by the pump light. By using the laser diode in this way as a photodetector, the coupling into the active-region can be brought reasonably close to the optimum. Next, the laser is biased above threshold and the photomix-induced beatnote is monitored on a microwave spectrum analyzer while making final adjustments to the pump focus. Finally, the fiber squeezer is tweaked to maximize the modulation power by bringing the polarizations of the mixing beams into alignment.

2.6 Fundamental modulation response of a TJS laser diode

In this section, the active-layer photomixing technique is used to measure the fundamental frequency response of a GaAs/GaAlAs semiconductor laser to 12 GHz [1], [2]. Well beyond the relaxation resonance, the theoretically predicted 40 dB/dec rolloff in the response is observed. Other features of the measured response function are also observed to be the theoretical ideal.

The device used in this experiment is a Mitsubishi GaAs transverse junction stripe (TJS) laser diode with a 16.2 mA lasing threshold and lasing wavelength of 838 nm. This particular device has a transparent contact to facilitate the photomixing process. It was mounted in a low-frequency hermetically-sealed capsule which was disassembled

for the experiment. As shown in Fig. 2.8, the mixed pump light is focused by a cylindrical lens and microscope objective to a stripe coincident with the active region. In this way we can couple uniformly into the active region over the entire length of the device. The modulation signal is detected with a *p-i-n* photodiode (Ortel PD050-OM). An optical isolator with 35 dB isolation (not shown) suppresses feedback to the laser diode and rejects any scattered pump light going to the detector. The detected microwave photocurrent is measured with an HP 8565A spectrum analyzer combined with an HP 8349B amplifier. We calibrated the detection system—*p-i-n* photodiode, amplifier and cables—to 20 GHz by photomixing directly on the detector, as discussed above. A storage normalizer is then used to subtract the detector response from the measured modulation characteristics. The cold stage was not used in this room temperature experiment.

The beat frequency power incident on the active region of the semiconductor laser is approximately 7 mW, which takes into account a 30% Fresnel reflection from the contact layer. The intensity modulation index of the semiconductor laser output may be found from the ratio of the amplitude of the ac photocurrent to the dc photocurrent induced in the detector. The modulation index is 5.6% and 10.3% well below the resonance for a 28 mA and 22 mA bias, respectively.

Plots of the observed modulation response (normalized by their low-frequency value) at different bias currents appear in Fig. 2.9. Data points are only given on two curves for clarity. The data for the 25 mA characteristic extend as far 12 GHz (the high-frequency cut-off in the data is caused by the noise floor in the detection system,

which rises as a function of frequency). We note the resonances are clearly defined. For each characteristic we also observe the ideal 40 dB/dec rolloff well beyond the resonance. This is most easily seen on the 17, 19, and 22 mA characteristics where the data extend to several multiples of the resonance frequency. By use of (2.3.20) and (2.3.21) we can extract from these characteristics ω_R and γ for each bias level. A plot of ν_R^2, where $\nu_R = \omega_R/(2\pi)$, versus laser bias current, proportional to output power, appears in Fig. 2.10. These data exhibit the theoretical linear behavior predicted by (2.3.22).

The damping rate, γ, can be expressed as

$$\gamma = \gamma_o + K\omega_R^2 \tag{2.6.1}$$

where γ_o includes the power independent sources of damping and $K = \tau_p(1+\frac{\Gamma|g_p|}{g_n})$ (see (2.3.24)). The theoretical linear relationship between γ and ω_R^2 is verified in Fig 2.11. The slope and intercept of the fitted line yield estimates for γ_o and K of 0.84 GHz (corresponding to a carrier spontaneous lifetime of 1.2 ns) and 6.2 ps, respectively. Based on a photon lifetime for this device of 3 ps, differential gain parameter of 2.5×10^{-6} cm^3 sec^{-1}, and mode confinement factor of 0.4, then $|g_p|$ is determined to be 6.9×10^{-6} cm^3 sec^{-1}.

In conclusion, we have measured the intrinsic modulation response of a GaAs/GaAlAs TJS laser diode by the active-layer photomixing technique. The measured response characteristics appear to be ideal, and there is no indication of any parasitic effects. Well beyond the resonance, the theoretically predicted 40 dB/dec rolloff is observed. The dependence of the resonance frequency and damping rate on

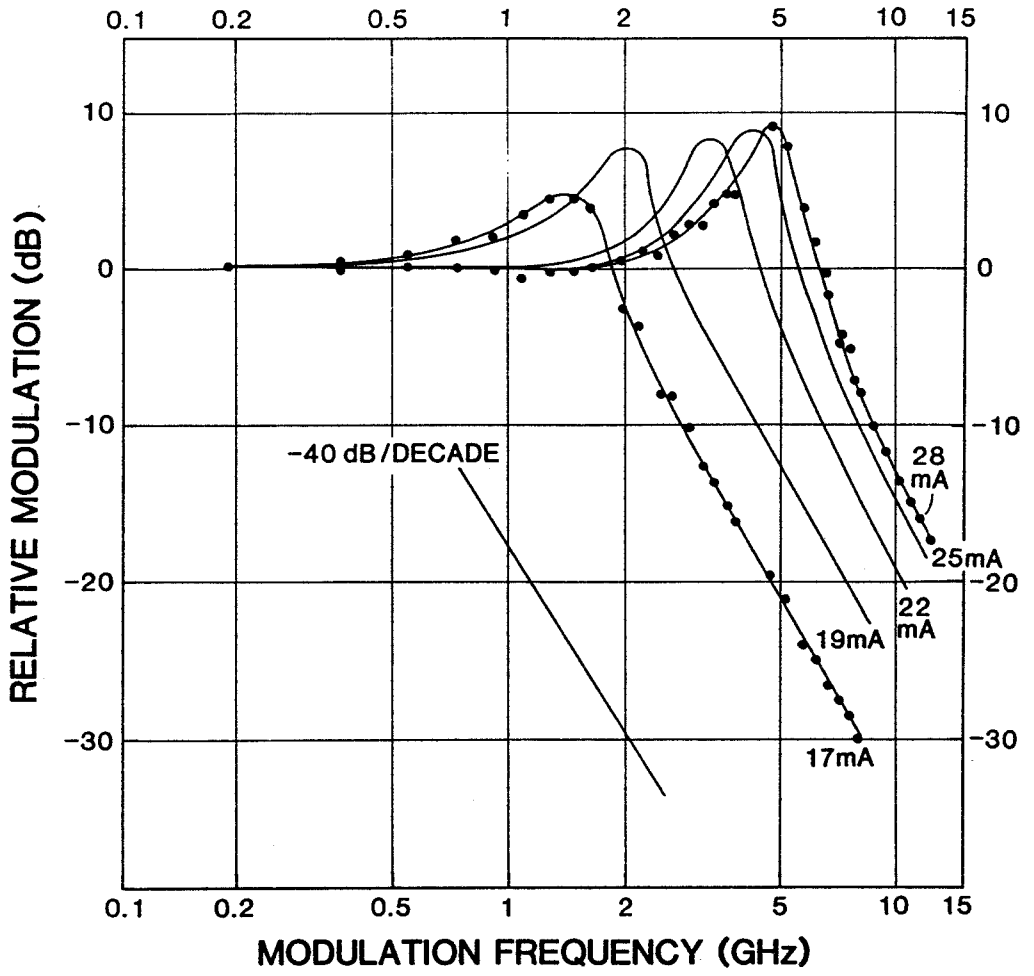

Figure 2.9: Measured modulation response at different bias levels. The resonance peaks and 40 dB/dec rolloff at high frequency are clearly visible, indicating the abscence of parasitic effects.

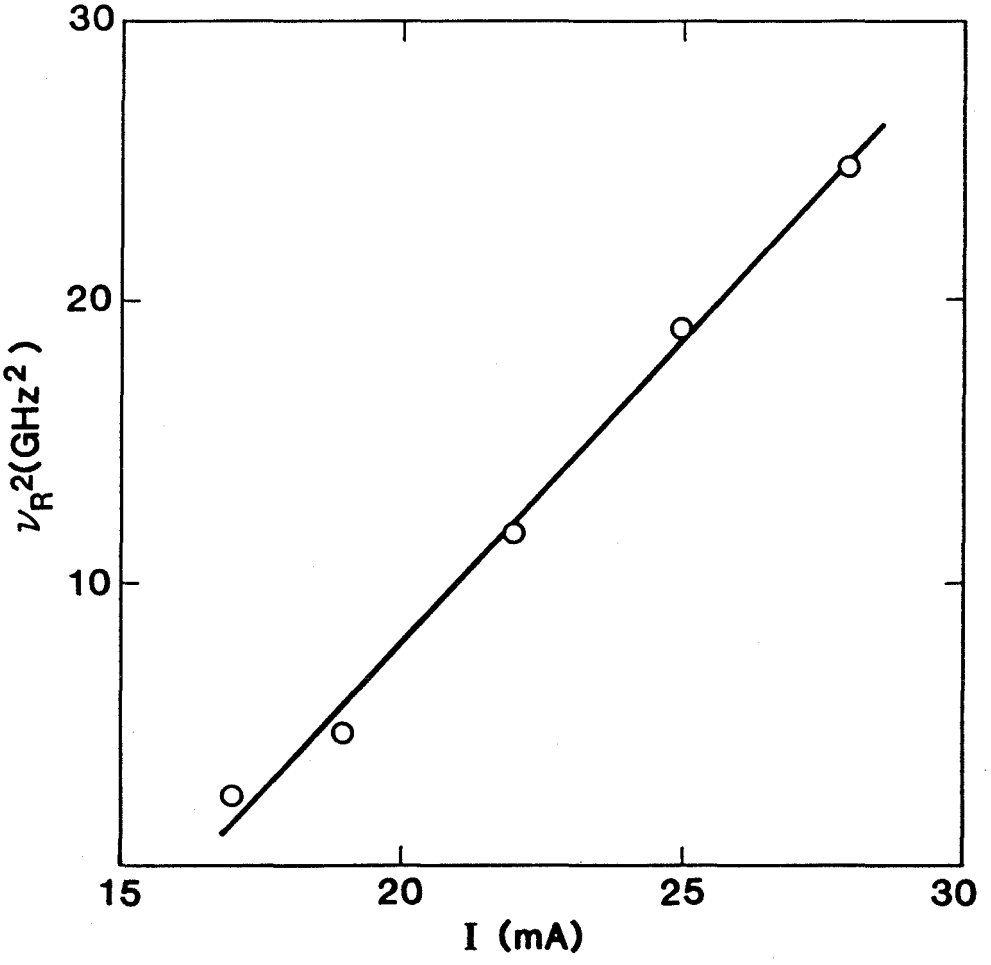

Figure 2.10: Square of the resonance frequency vs. bias current. The ideal linear relationship is predicted by the rate equations.

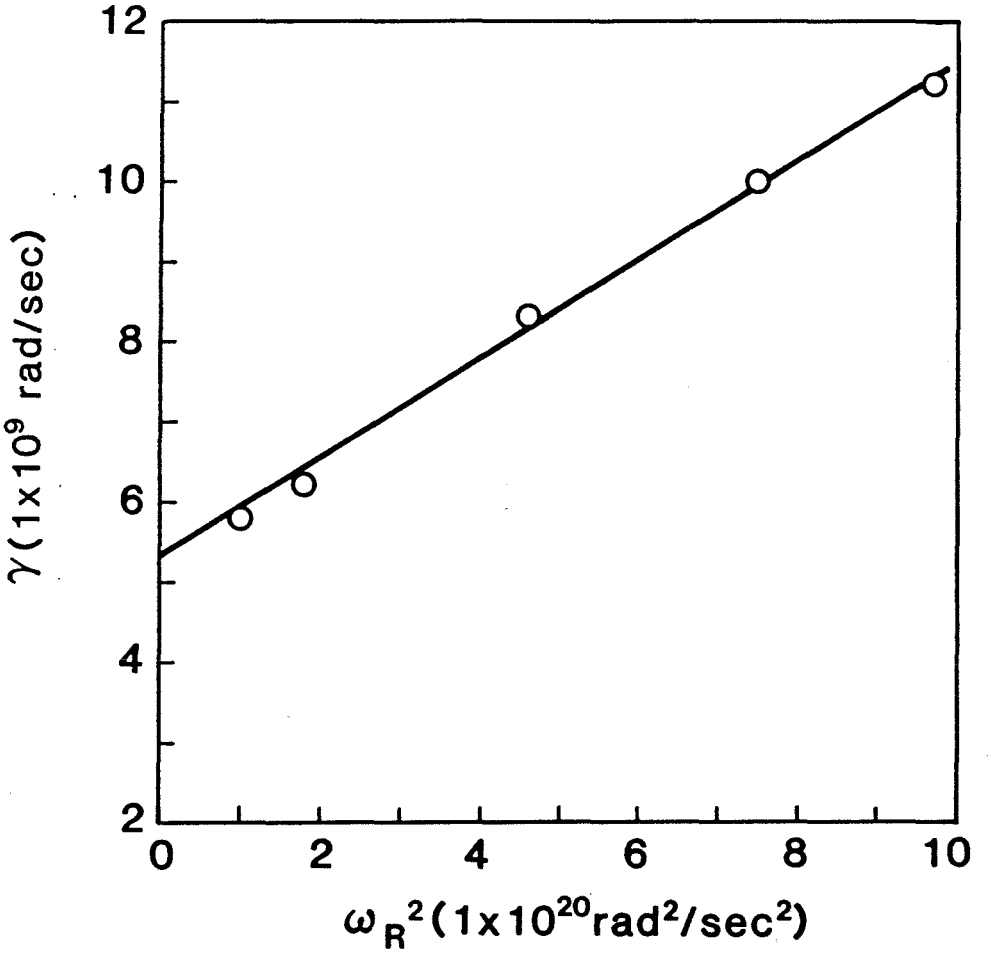

Figure 2.11: Damping rate γ vs. ω_R^2. The ideal linear relationship is predicted by the rate equations.

laser output power are also observed to be the theoretical ideal.

2.7 Low-temperature modulation response of a TJS laser diode

In this section, we use the active-layer photomixing technique to directly modulate the output of a GaAs/GaAlAs TJS laser operating at cryogenic temperatures [4]-[6]. Our objective in these low-temperature experiments is twofold. First, the laser dynamics change in dramatic ways at low temperature [32]. From the measured response functions, the relaxation resonance frequency and the damping rate can be extracted. The temperature dependence of these parameters can then be compared with theory. Second, the parasitic-free nature of the photomixing technique can be further verified because the device parasitics become especially severe at low temperature. For instance, at 4.2 K, the parasitic RC corner frequency is estimated to be 410 MHz, yet the response of the TJS laser measured by active-layer photomixing appears ideal out to 15 GHz.

2.7.1 Experimental details

The experimental arrangement for the low-temperature measurements is similar to the layout shown schematically in Fig. 2.8, the main difference being that the laser is mounted on a copper heat sink in a low-temperature cryostat under vacuum conditions (5×10^{-8} Torr). The cryostat may be operated with either liquid nitrogen or liquid helium. It is also equipped with a resistive heater and temperature controller to

maintain the heat sink within a degree of the desired temperature. Because efficient optical coupling into the laser diode's active region requires sub-micron mechanical stability, however, it proved necessary to allow sufficient time ($\approx$ 1 hr.) for thermal stresses in the mount and supporting column to equilibrate. For this reason, the heater was turned off, and the measurements were performed only at room temperature, liquid nitrogen temperature (77 K), and liquid helium temperature (4.2 K).

For the TJS laser, the photomixing light at the 752.5 nm wavelength used in the room-temperature measurement of the previous section is less efficiently absorbed in the active region at low temperature. Because the band gap increases as the semiconductor crystal is cooled (see below), the GaAs becomes less absorbing at this wavelength. We therefore switched to a shorter pump wavelength, using the 676.4 nm Kr line and converting the dye laser to run DCM dye. The GaAs is more strongly absorbing at this shorter wavelength from room temperature down to 4.2 K, while the GaAlAs cladding layer remains transparent. This wavelength was then used for all subsequent photomixing experiments.

A pair of quartz windows positioned at right angles on the vacuum chamber provides access to the top surface and front facet of the TJS laser. Because the working distance from the chamber window to the laser is about 5 cm, high-quality lenses were required to provide the best possible diffraction-limited focus.

2.7.2 The effects of low temperature on a laser diode

When a semiconductor laser is cooled, many things happen. Among them: the threshold current decreases, the lasing wavelength shifts to shorter wavelengths, the differ-

ential gain increases, and the series resistance of the contact layer increases. Many of these effects stem from the temperature dependence of the Fermi distribution function, which becomes more step-like as temperature goes down (see (2.2.4)). However, each of these effects will be dicussed in turn.

A sharper Fermi factor at low temperature causes the gain spectrum to narrow considerably [33]. Consequently, the carrier density required to reach threshold is correspondingly reduced [34]. In Fig. 2.12, light output power from the TJS laser versus bias current (L-I characteristic) is shown at three temperatures. Threshold current decreases from 14.3 mA at room temperature to 0.63 mA at liquid helium temperature. There appear to be no ill effects from cooling on the laser, because the L-I characteristics are highly linear at all three temperatures.

A narrower gain spectrum also enhances the differential gain [35]. This has a direct effect on the fundamental modulation response, because the relaxation resonance is pushed out to higher frequencies for a given output power. This will become evident when the low-temperature modulation data are presented below.

The band gap of the semiconductor is also dependent on temperature [36]. Upon cooling, the thermal contraction of the crystal lattice increases the width of the direct gap. Therefore, as the temperature is lowered the lasing wavelength moves to shorter wavelengths. Figure 2.13 shows the lasing spectrum at three temperatures. The wavelength shifts from 823 nm at room temperature, to 787 nm at liquid nitrogen temperature, and to 782 nm at liquid helium temperature. Interestingly, the TJS is seen to be fairly single-mode at 293 K and 77 K, but becomes multimode at 4.2 K.

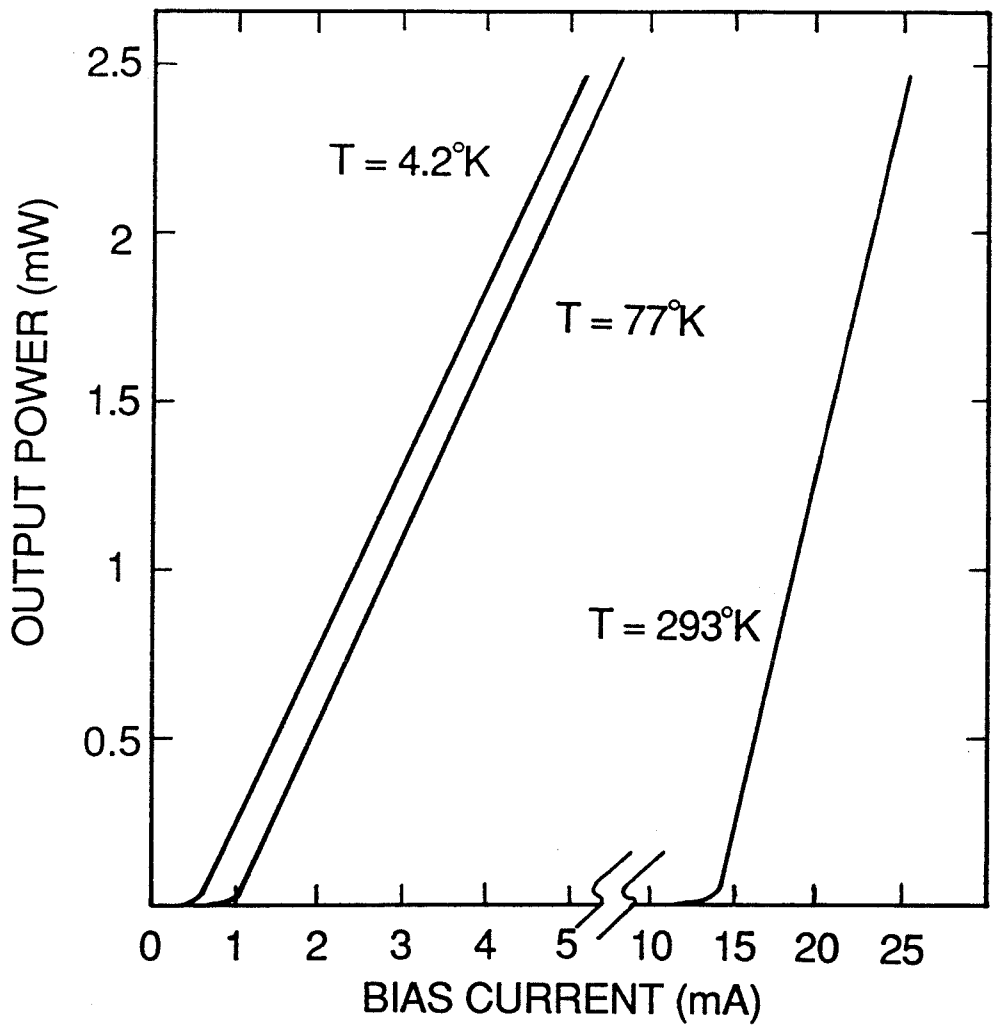

Figure 2.12: Lasing output power versus injection current (L-I characteristic) at three temperatures. The threshold current is 14.3 mA at room temperature and falls to 0.63 mA at liquid helium temperature.

The reason for this is not known.

A further low-temperature effect on the TJS is that the resistance of the contact layer increases owing to the freezing-out of excess carriers. The parasitic response is thus degraded, because the RC corner frequency of the parasitic circuit (see Fig. 2.4) decreases as R increases. Current-voltage characteristics for the laser diode at forward bias are shown in Fig. 2.14. The differential resistance dV/dI increases from 7 Ω at room temperature to 39 Ω at liquid helium temperature, over a factor of five increase. Assuming a typical 10 pF contact layer capacitance for this device, the parasitic RC corner frequency is only 410 MHz at 4.2 K. Conventional current modulation of the laser at microwave frequencies thus becomes very inefficient at low temperature.

2.7.3 Experimental results

Typical response curves at each temperature for optical modulation of the TJS are shown in Fig. 2.15. The bias levels are adjusted so that each curve corresponds to an output power of approximately 2 mW per facet. We see that the resonances are clearly defined, and that the relaxation resonance frequency increases considerably as the temperature is lowered. In addition, the room temperature response curve eventually rolls off at the theoretical 40 dB/dec rate. The high-frequency cut-off in the data results from the limited photodetector bandwidth and noise floor of the microwave spectrum analyzer. As mentioned above, the parasitic RC corner frequency is about 410 MHz at 4.2 K, yet there is no effect on the measured response curve, with the data appearing to be ideal out to 15 GHz.

Modulation response functions for many different output power levels were mea-

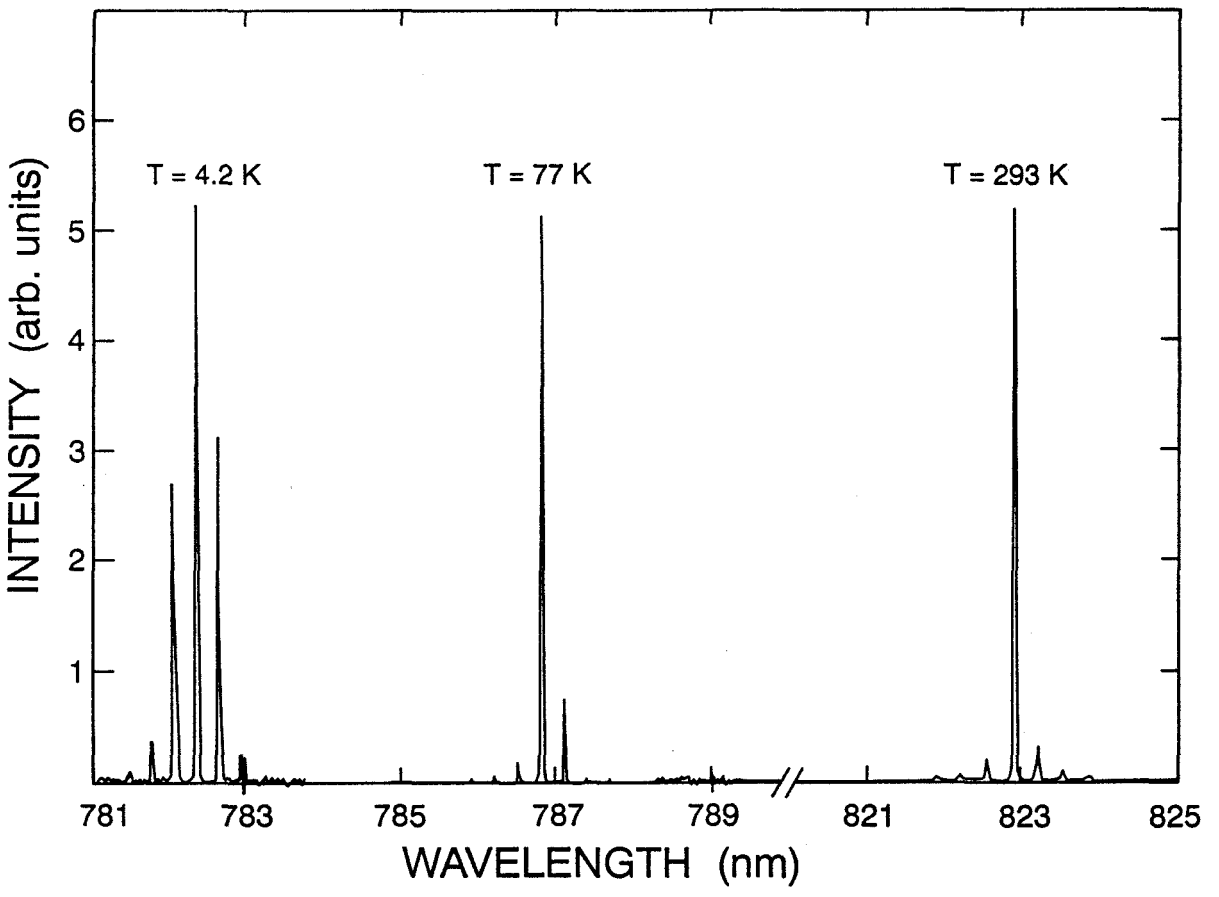

Figure 2.13: Lasing spectrum at three operating temperatures. The lasing wavelength shifts from 825 nm at room temperature to 782 nm at liquid helium temperature.

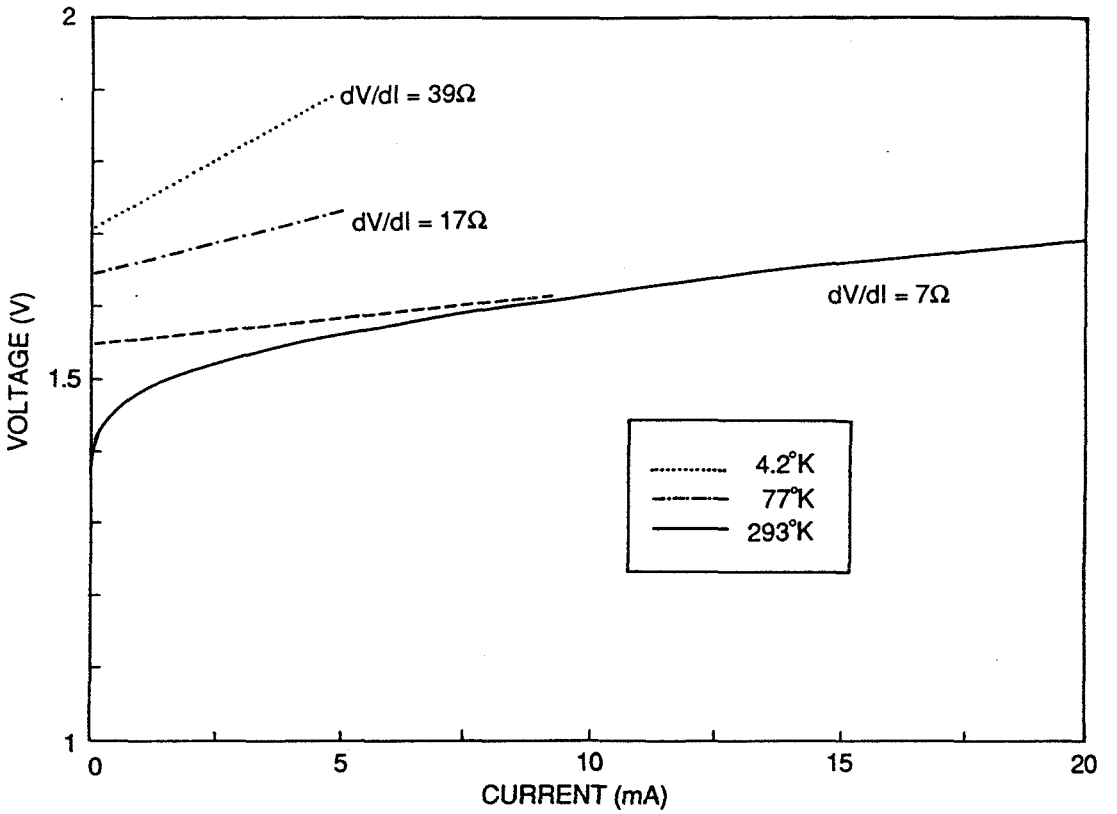

Figure 2.14: The differential resistance of the TJS laser increases from 7 Ω at room temperature to 39 Ω at liquid helium temperature. The two low-temperature characteristics have sharp knees at turn-on and are indistinguishable from the asymptotes. Also note the turn-on voltage increases as temperature is lowered, another manifestation of the increasing band gap energy and concomitant increase in quasi-Fermi level separation at threshold.

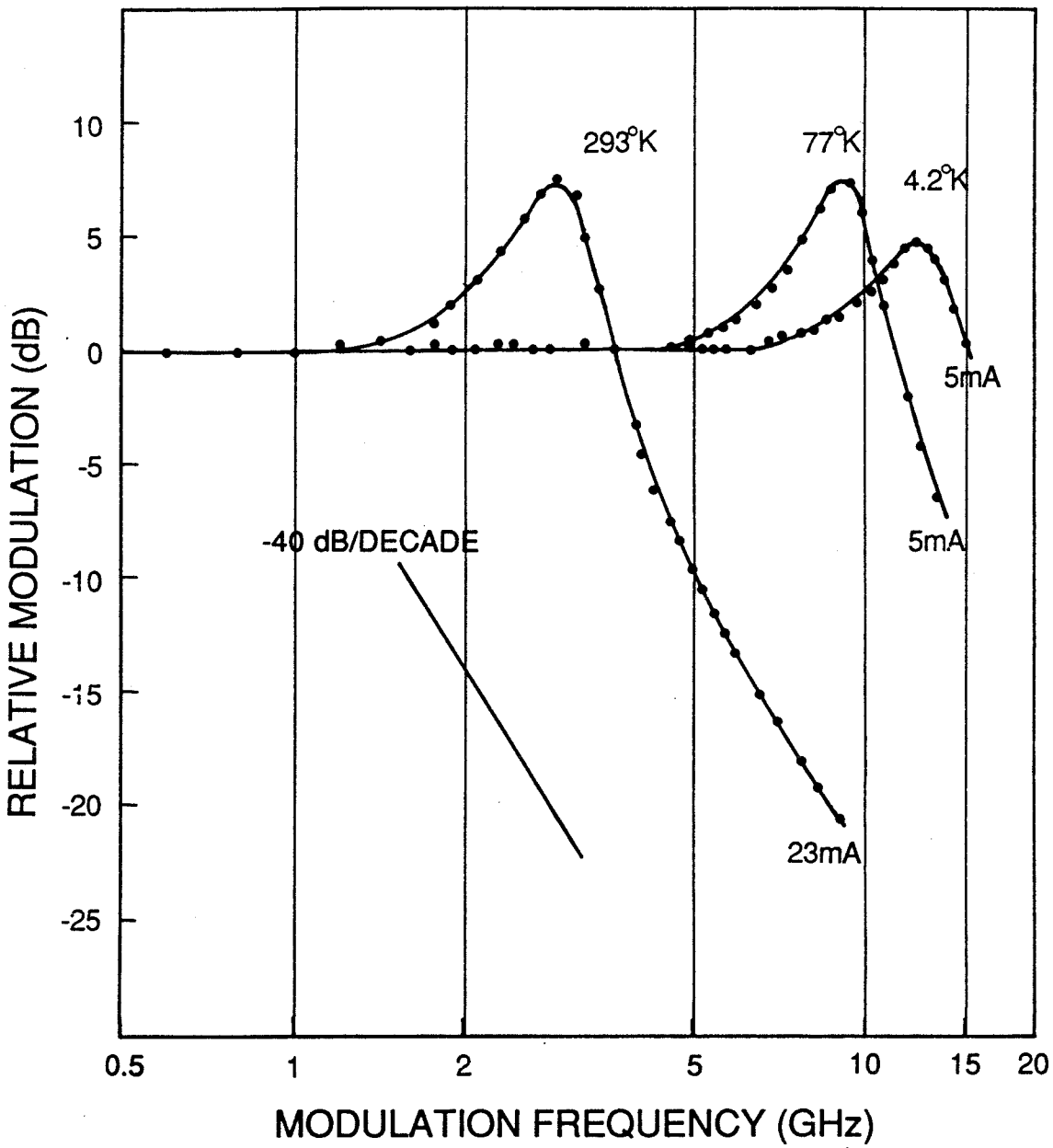

Figure 2.15: Active-layer photomixing modulation response data at three temperatures. For each characteristic the output power is 2 mW per facet.

sured at each temperature. From these, the resonance frequency and damping rate were extracted, in accordance with (2.3.20) and (2.3.21).

A plot of the square of the relaxation resonance frequency ($\nu_R = \omega_R/(2\pi)$) versus output power appears in Fig. 2.16. The theoretical linear behavior given by (2.3.22) is seen at all three temperatures. The slope of the line increases by a factor of 7.0 and 13.6 at 77 K and 4.2 K, respectively, over the room temperature slope. Assuming that the photon lifetime and modal volume of the lasing mode are not significantly affected by temperature, then the increase in slope results primarily from a large increase in g_n caused by the narrower gain spectrum at low temperature.

In Fig. 2.17 the damping rate γ is plotted as function of ω_R^2. For each temperature the linear relationship predicted by (2.3.24) is observed. The slope of the fitted line decreases from 9.3 ps at 293 K to 5.6 ps at 77 K and 4.2 K. This decrease in slope, from room temperature to liquid nitrogen temperature, is consistent with the theoretical expression which incorporates the nonlinear gain (2.3.24) and the measured increase in the differential gain at 77 K. The apparent saturation in the slope as the temperature is lowered from 77 K to 4.2 K has two possible explanations. One is that the increased differential gain causes the $\Gamma|g_p|/g_n$ term to become much less than unity, so that the slope is equal to the photon lifetime, τ_p. However, a 5.6 ps photon lifetime is too long for a 250 μm long laser with uncoated facets (see (2.3.3)). We estimate that for this device, τ_p is approximately 3 ps. The remaining explanation for the apparent saturation in the slope is that in going from 77 K to 4.2 K, the measured increase in g_n is compensated for by an increase in $|g_p|$. Although we do

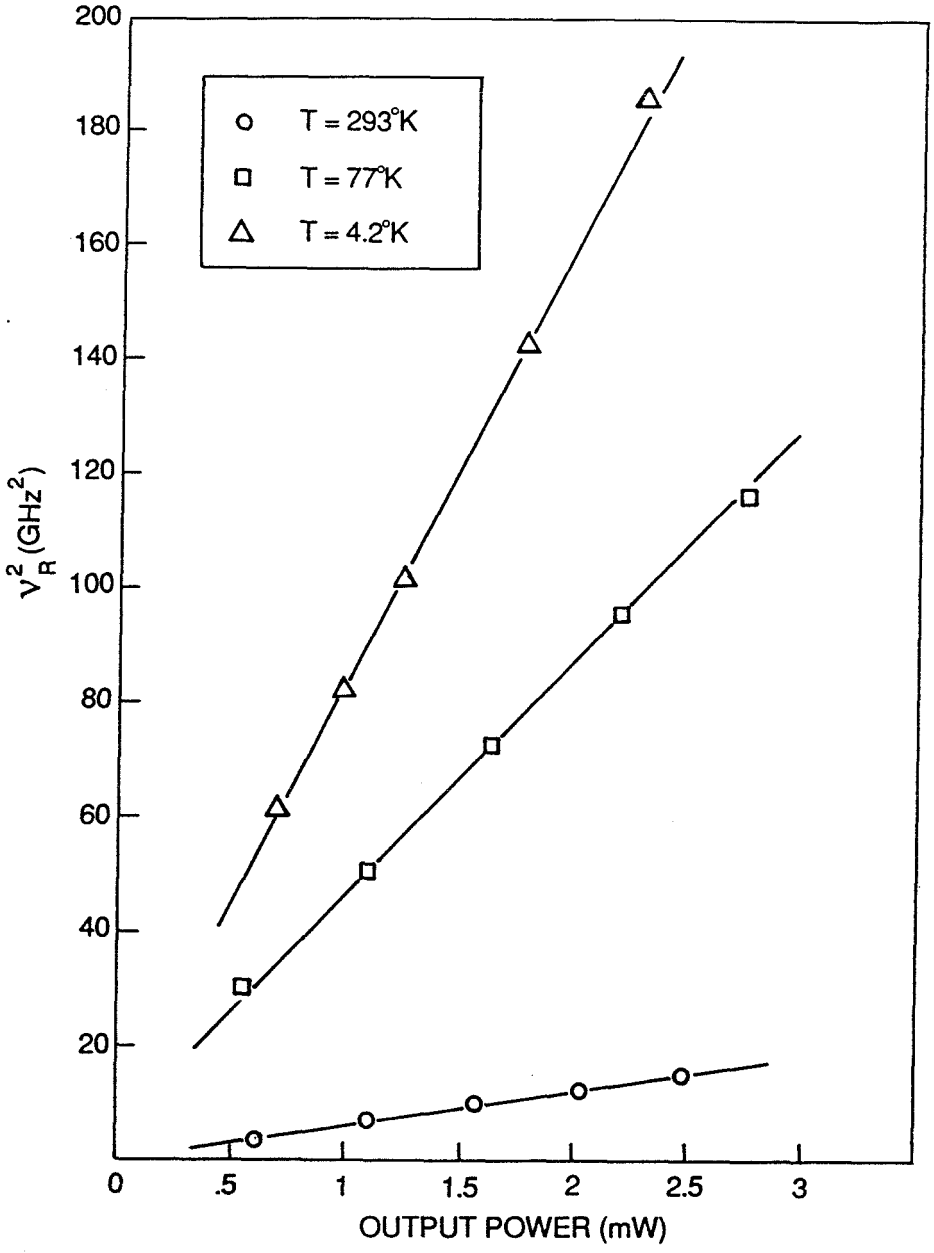

Figure 2.16: Square of resonance frequency vs. output power per facet.

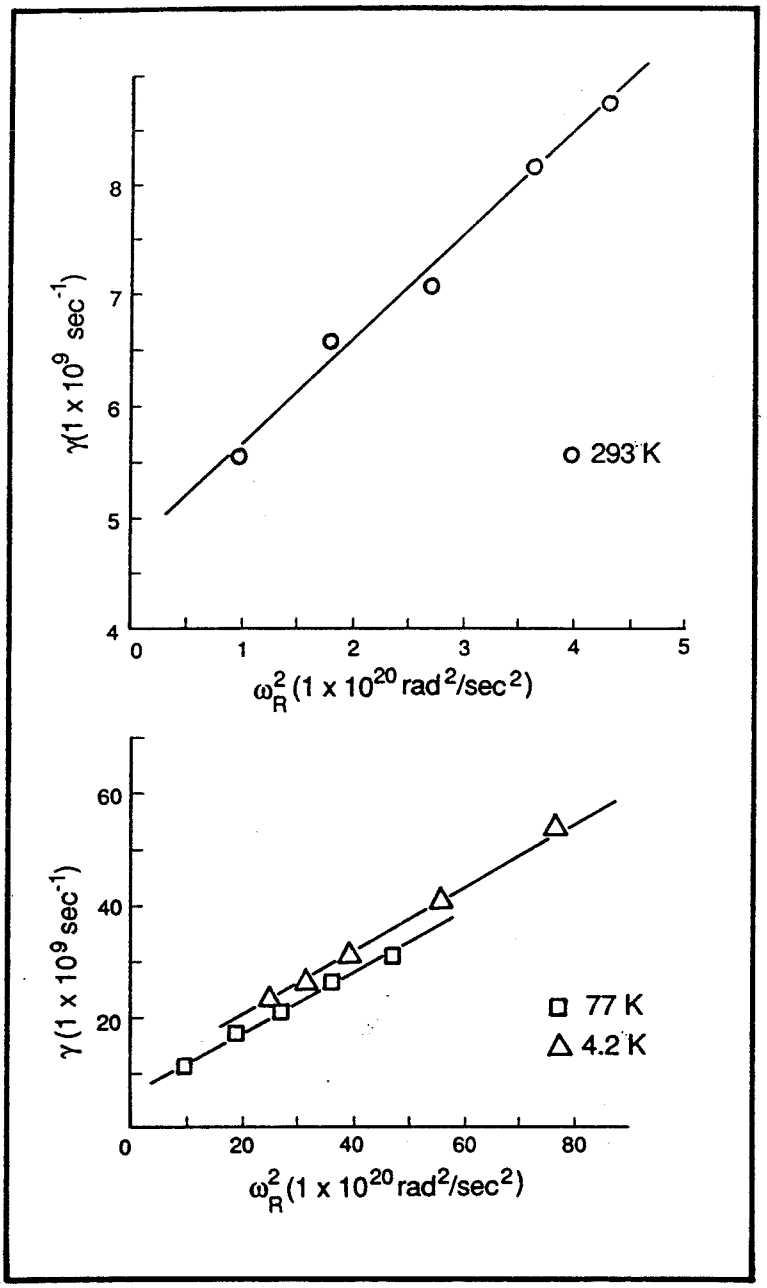

Figure 2.17: Damping rate vs. square of resonance frequency.

not speculate here on the many proposed origins of the nonlinear gain (e.g., spectral hole burning [37], dynamic carrier heating [13], standing wave dielectric grating [38], etc.) further low-temperature modulation experiments could help discriminate among possible mechanisms.

In summary, we have used the active-layer photomixing technique to directly modulate the output of a semiconductor laser operating at cryogenic temperatures. The technique produces parasitic-free modulation, enabling a measurement of the laser diode's intrinsic modulation response. Even at 4.2 K, where the parasitic corner frequency is estimated to be 410 MHz, the modulation response appears ideal out to 15 GHz. From the measured response curves we find values for the relaxation resonance frequency and the damping rate. Their low-temperature behavior agrees with the simple theory incorporating the nonlinear gain.

2.8 Active-layer photomixing to millimeter-wave frequencies

In this section the active-layer photomixing technique is used to measure the room temperature modulation response of a GaAs/GaAlAs laser diode to the millimeter wave frequency of 37 GHz [7]. The modulation sidebands in the field spectrum are detected with an ultra-high-finesse ($\sim$ 40,000) Fabry-Perot interferometer, and the measured response agrees with the theoretical response function. Although wide-band millimeter wave modulation (to 38 GHz) has been reported for a cooled InGaAsP laser with a 31 GHz corner frequency [39], in this measurement the laser diode's

resonance frequency is only 6.5 GHz. As will be seen, with a moderately faster device (i.e., resonance frequency $\sim$ 10 GHz), it should be possible to directly measure the modulation response beyond 100 GHz.

2.8.1 Detection of high-frequency modulation with a Fabry-Perot interferometer

To measure the laser diode's modulation response, the modulated light is usually detected with a fast *p-i-n* photodiode connected to an electronic microwave spectrum analyzer, as in sections 2.5 – 2.7. The detection bandwidth of commercially available near-infrared photodetectors, however, is limited to about 20 GHz. In addition, the photocurrent signal must compete with a noise floor in the spectrum analyzer which typically starts at -110 dBm near dc (for a 10 kHz integration bandwidth) and climbs at a rate of 1.7 dB/GHz [40]. A much larger detection bandwidth can be obtained by measuring the modulation signal with an optical spectrum analyzer, a scanning Fabry-Perot interferometer (FPI). The modulation then appears as sidebands in the laser field spectrum. However, the ability to observe modulation sidebands at high frequencies depends critically on the finesse of the FPI, which should be as high as possible. For this experiment, the FPI (Newport SR-240) has a finesse of 40,000, a free spectral range of 8 THz, and an instrumental resolution of 200 MHz for 800 nm light.

As shown below, beyond the resonance frequency the modulation sidebands in the field spectrum asymptotically approach a 40 dB/dec rolloff. Clearly there exists some high-frequency limit beyond which the sideband signal is not measurable. However,

in contrast to the electronic spectrum analyzer, the background, or noise floor, arising from the FPI is a decreasing function of frequency. This background results from the presence of the lasing mode (i.e., the optical carrier) which appears as a Lorentzian with the linewidth of the FPI, assuming the FPI linewidth is much greater than the lasing mode linewidth, as is the case here. The tails of this Lorentzian roll off at 20 dB/dec, eventually obscuring the sideband signals. As Fig. 2.18 shows, however, this point of intersection can be at ultrahigh frequencies, far into the millimeter wave regime (> 30 GHz). The figure shows, in a log-log plot, a typical modulation response function ($|\tilde{p}|^2$) of a laser diode with a 10 GHz resonance frequency and relative sideband amplitude, at the resonance, of 10%. Also shown is the background from the optical carrier, assuming a corner frequency of 100 MHz, corresponding to a 200 MHz linewidth for the Lorentzian. At frequencies where the modulation response function lies above the Lorentzian, the modulation sidebands are, in principle, detectable. For this example the high frequency detection limit can be over 150 GHz. In practice, the background level may be raised somewhat by spontaneous emission from the laser diode, but this did not affect our measurement.

In general, the frequency of intersection in Fig. 2.18 is given by

$$\Omega_x = \frac{m\omega_R^2}{\Omega_{FP}} \tag{2.8.1}$$

where m is the modulation index, ω_R is the relaxation resonance frequency of the laser, and Ω_{FP} is the 3 dB frequency of the Fabry-Perot Lorentzian. If the experimental goal is to observe the modulation response of the laser diode to as high a frequency as possible, then (2.8.1) shows that a Fabry-Perot with a narrow linewidth

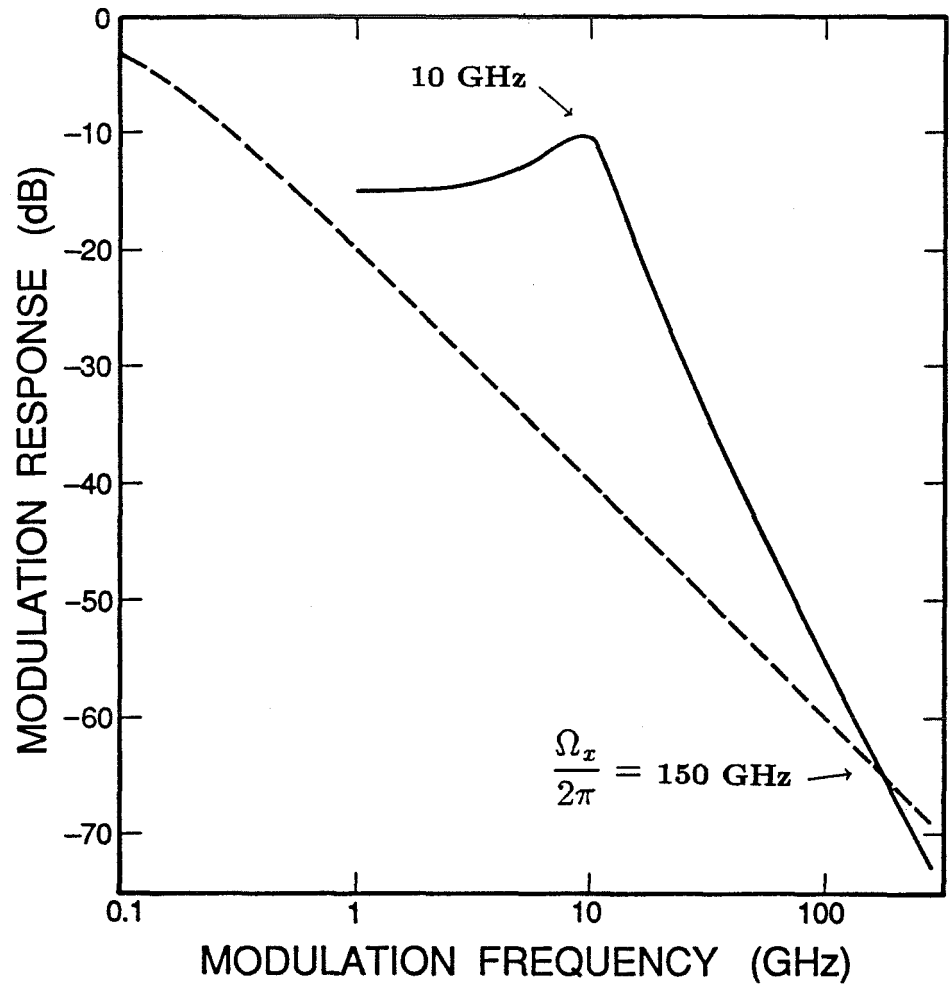

Figure 2.18: Graphical evaluation of modulation sideband detection using a Fabry-Perot interferometer. At frequencies where the modulation response function lies above the background Lorentzian (dashed curve), the modulation sidebands are observable.

is required, and that $m\omega_R^2$ should be maximized. To increase the modulation index m, the photomixing power can be increased, but for facet pumping, as in this experiment, the mixing power must be kept relatively low so as not to damage the laser facet. Although it may seem possible to increase Ω_x by running the laser diode at high bias, thereby pushing ω_R to higher frequencies, Ω_x is actually independent of laser power, because m has inverse power dependence ($m \propto \tilde{p}/P_o$ whereas $\omega_R^2 = g_n P_o/\tau_p$). An ideal laser diode for this experiment is thus intrinsically fast, i.e., g_n/τ_p is maximized, and also single mode, so that the modulation energy is not partitioned into numerous sidebands on each lasing frequency.

The FPI used in this experiment has a 20 μm cavity and 30 cm radius of curvature mirrors. In this near-planar resonator, higher-order transverse modes spaced 27.6 GHz apart may be excited by a single-frequency optical input [41]. These modes may potentially interfere with the detection of the modulation sidebands whenever the modulation frequency is near a multiple of 27.6 GHz. However, the higher-order transverse modes appear only on the high-frequency side of the fundamental, whereas the modulation sidebands appear symmetrically on both sides of the fundamental. The low-frequency sideband can thus be tracked more readily as a function of modulation frequency. Careful matching of the optical input to the fundamental transverse mode is still required, however, because weakly excited longitudinal modes of the semiconductor laser, spaced 140 GHz apart, may excite their own set of higher-order transverse modes in the FPI. In our experiment, optimum mode-matching into the FPI suppresses the higher-order transverse modes by at least 26 dB compared with

the fundamental.

2.8.2 Modulation sidebands in the field spectrum

We now examine how the intrinsic response function $\tilde{p}(\Omega)$ relates to the laser field spectrum, which is what is observed at the output of a FPI. Direct modulation of a semiconductor laser, by active-layer photomixing or injection current modulation, affects the amplitude and also the phase of the laser field due to the dependence of refractive index on carrier density. The time-dependent field may then be taken as

$$E(t) = \left(E_o + \tilde{E}(\Omega)\cos\Omega t\right) \exp\left[i\left(\omega_L t + \tilde{\phi}(\Omega)\cos\Omega t\right)\right] \tag{2.8.2}$$

where ω_L is the cw oscillation frequency and $\tilde{E}(\Omega)$ is the small-signal field amplitude, given by

$$\frac{\tilde{E}(\Omega)}{E_o} = \frac{1}{2}\frac{\tilde{p}(\Omega)}{P_o} \tag{2.8.3}$$

i.e., the field amplitude is proportional to the photon density amplitude when they are small-signal quantities. In (2.8.2), $\tilde{\phi}(\Omega)$ is the response function of the phase deviation, given by [42]

$$\tilde{\phi}(\Omega) = \frac{1}{2}\alpha\frac{\tilde{p}(\Omega)}{P_o} \tag{2.8.4}$$

where α is the linewidth enhancement factor. Although $\tilde{p}(\Omega)$, $\tilde{E}(\Omega)$, and $\tilde{\phi}(\Omega)$ are, in general, complex functions, we treat them as real for our purposes since their relative phases become zero at high frequencies beyond the relaxation resonance [16]. The field spectrum resulting from (2.8.2) consists of the center line at ω_L, and AM and FM induced sidebands at $\omega_L \pm n\Omega$, where n is an integer. For modulation frequencies greater than the relaxation oscillation frequency, only the $n = 1$ sidebands

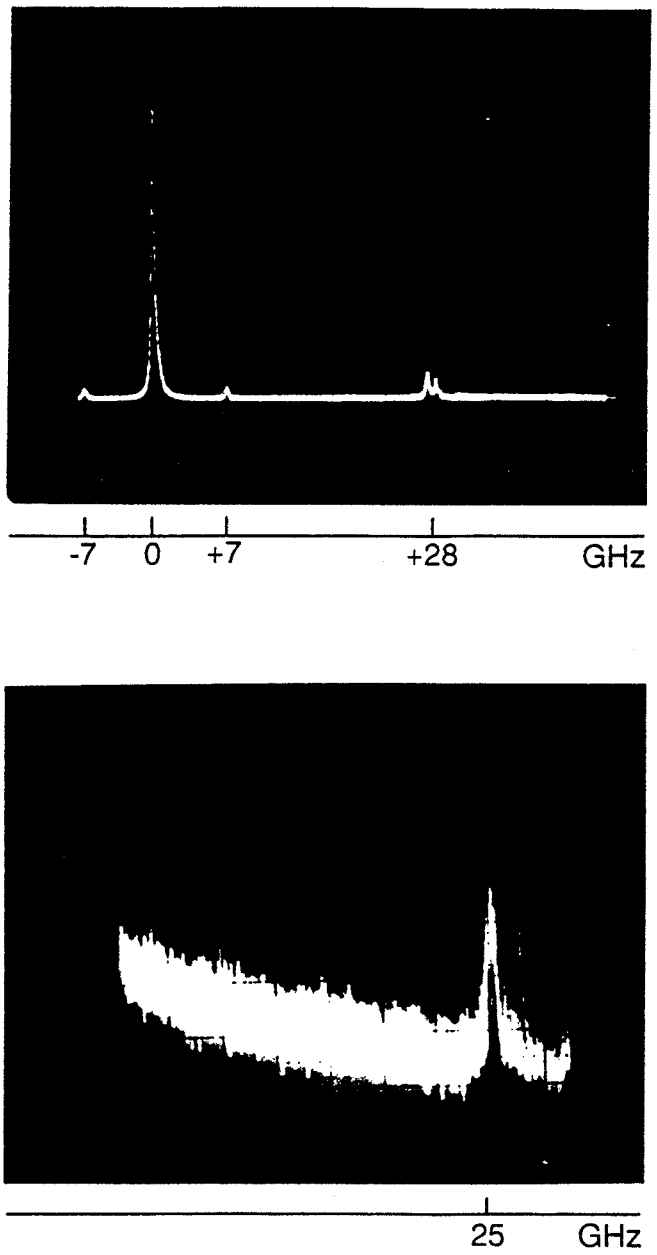

Figure 2.19: Laser field spectrum observed with a scanning Fabry-Perot interferometer. The upper photo shows the lasing line with modulation sidebands at ± 7 GHz. The peak at 27.6 GHz is a higher order Fabry-Perot mode as discussed in the text. The lower photo shows a close-up of a modulation sideband when the laser is modulated at 25 GHz. The decaying tail of the background Lorentzian is clearly visible.

are observable. The amplitude of these first sidebands is equal to

$$A(\omega_L \pm \Omega) = \left(E_o J_1(\tilde{\phi}(\Omega))\right)^2 + \left[\frac{1}{2}\tilde{E}(\Omega)\left(J_0(\tilde{\phi}(\Omega)) - J_2(\tilde{\phi}(\Omega))\right)\right]^2 \qquad (2.8.5)$$

where J_n is the Bessel function of order n. For small-signal modulation we may use the approximation

$$J_n(x) \approx \frac{x^n}{2^n n!}, \qquad x \ll 1 \qquad (2.8.6)$$

and so obtain

$$A(\omega_L \pm \Omega) = \frac{1}{4}\left(E_o^2\tilde{\phi}(\Omega)^2 + \tilde{E}(\Omega)^2\right) \quad \propto \quad (\tilde{p}(\Omega))^2 \qquad (2.8.7)$$

where (2.8.3) and (2.8.4) were used to get the final proportionality relation. The amplitude of the first order modulation sidebands, as a function of Ω, is therefore directly proportional to the square of the intrinsic response function $\tilde{p}(\Omega)$.

2.8.3 Experimental details

The experimental arrangement appears in Fig. 2.20. The laser under study is an Ortel GaAs/GaAlAs buried heterostructure device with a 23 mA threshold current and lasing wavelength of 786 nm. The laser, at room temperature, is biased above threshold by a dc injection current and the output is small-signal modulated by the active-layer photomixing technique. For the photomixing sources we use the Kr laser operating at 676.4 nm and the dye laser running DCM dye at the same wavelength. These sources are collimated from the output of a 50/50 fiber coupler and focused onto the rear facet of the laser diode, which is mounted on a narrow (300 μm) stub so that both facets may be accessed. A short-wavelength pass filter prevents feedback

to the rear facet from semiconductor laser light reflecting from the fiber end. The incident photomixing power is about 2.5 mW.

The emission from the modulated semiconductor laser is focused into a 50 m long single-mode optical fiber. An optical isolator with 40 dB isolation suppresses feedback to the front facet, and a narrow bandpass filter prevents any scattered pumping light from reaching the FPI. Coupling into the fiber serves the dual purpose of spatially filtering the lasing mode and rejecting a significant amount of spontaneous emission. Approximately 5 cm of the fiber jacket is removed at the input end and the exposed cladding is immersed in glycerine to strip the cladding modes propagating in the fiber. This was found to improve the mode-matching into the FPI. The output from the fiber is coupled into the FPI cavity through a 10 cm focusing lens, and the light transmitted through the FPI is conveyed to a photomultiplier tube (PMT) by a fiber bundle. The PMT photocurrent is converted to a voltage signal which is amplified and displayed on an oscilloscope whose sweep is synchronized with the FPI. The PMT gain is then set to a high value and the input light intensity is adjusted with calibrated neutral density filters.

2.8.4 Experimental results

Figure 2.21 shows the full modulation response of the laser diode running at a bias current of 40.5 mA. The high-frequency data (12 GHz $< \Omega/2\pi <$ 37 GHz) were obtained by measuring the modulation sideband relative amplitude, as discussed above. At the resonance, the relative amplitude (sideband/carrier) is 2%. For completeness, the low-frequency response ($\Omega/2\pi <$ 12 GHz) is also shown. These data were

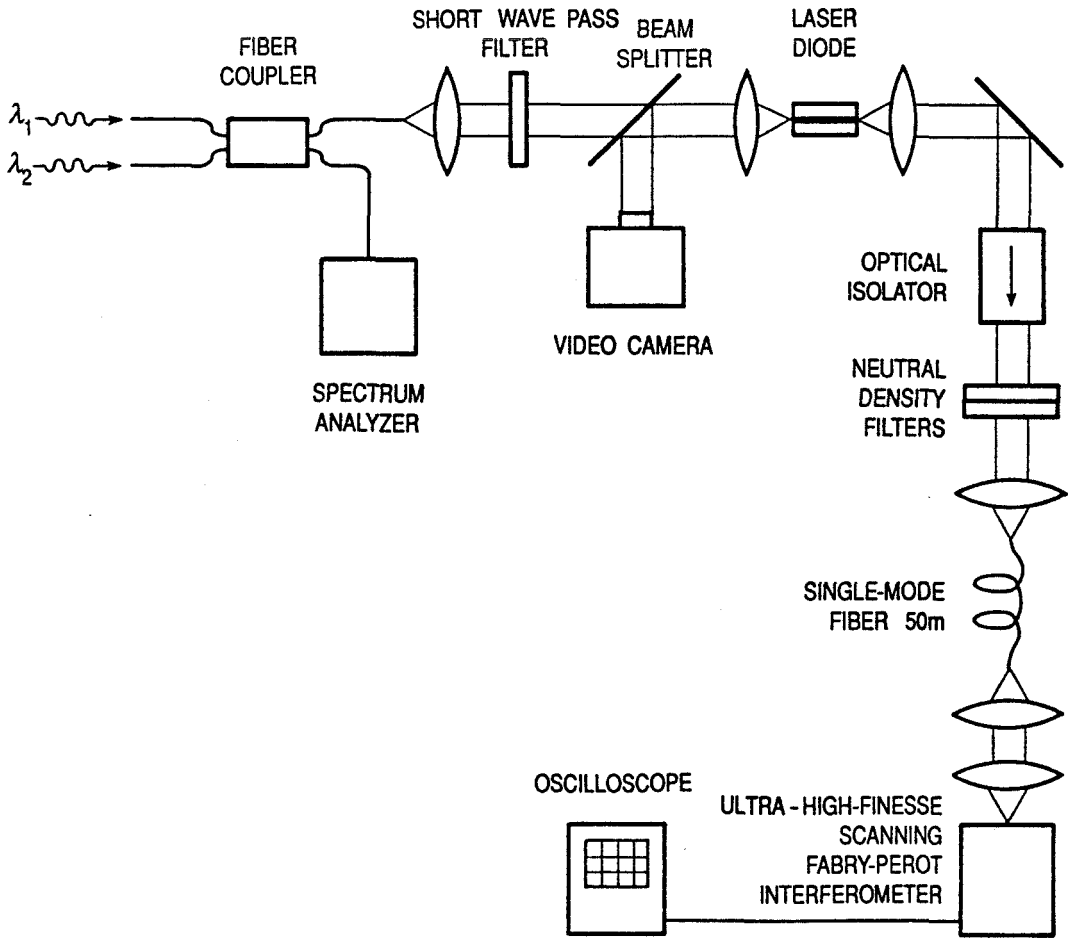

Figure 2.20: Schematic diagram of the experimental arrangement. The high-frequency modulation is generated in the laser diode by active-layer photomixing, and detected with an ultra-high-finesse Fabry-Perot interferometer.

recorded with a photodiode and microwave spectrum analyzer, because at low modulation frequencies, higher order sidebands complicate the spectrum observed on the FPI [44], [45]. From the low-frequency data we can determine the resonance frequency (6.5 GHz) and damping rate (4.7 GHz). A theoretical response curve based on these parameters also appears in the figure. The high-frequency data agree reasonably well with the theoretical curve to the highest measured frequency of 37 GHz. Again, no device parasitic effects are observable. Notice that the modulation sideband signal is lost approximately where the response curve and background Lorentzian intersect. We mention that a slightly faster laser ($\omega_R/2\pi \sim 7.5$ GHz for the same output power) was modulated to 44 GHz before the sideband signal was lost in the background. Unfortunately, it catastrophically failed before a complete response curve could be mapped out.

2.8.5 Sideband detection to higher frequencies

Equation (2.8.1) shows how the fundamental laser and Fabry-Perot parameters determine the high-frequency detection limit of the modulation sidebands. For a given laser and FPI, the response function and background Lorentzian cross at a fixed frequency, Ω_x. However, it is possible to boost the detection bandwidth by selectively filtering out the lasing mode carrier frequency before coupling into the FPI. This has the effect of pushing down the background Lorentzian in Fig. 2.18, thereby increasing Ω_x. We tested this idea by modifying part of the experiment as shown in Fig. 2.22. The modulated semiconductor laser light reflects from a diffraction grating before coupling into the optical fiber going to the FPI. Otherwise the experimental setup is

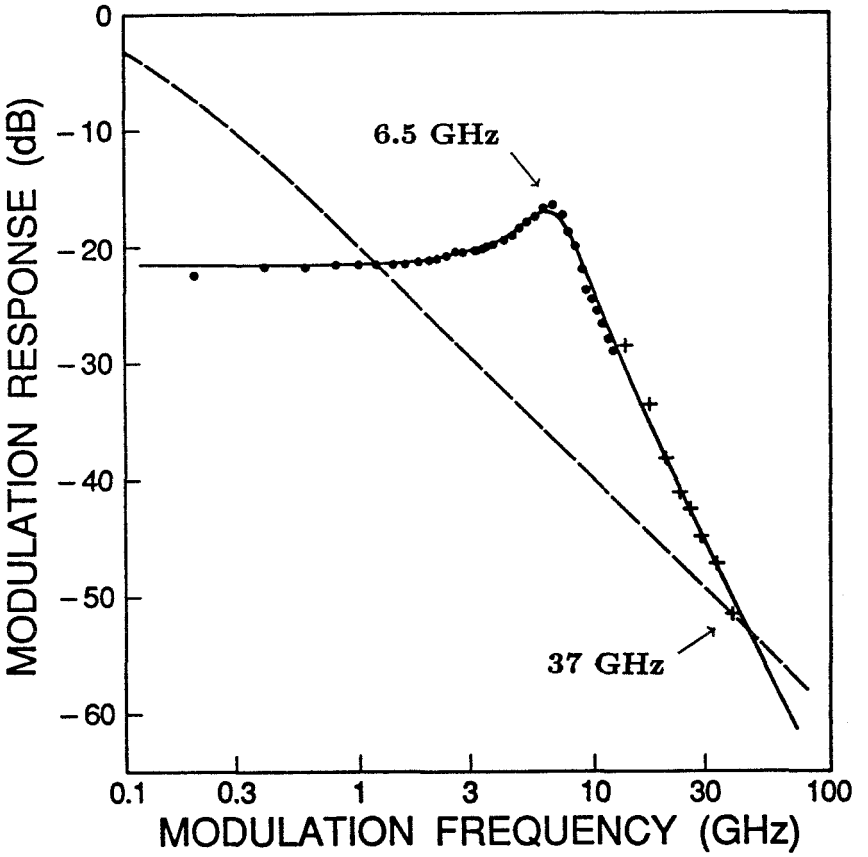

Figure 2.21: Modulation response of the GaAs/GaAlAs laser to millimeter-wave frequencies. The high-frequency data (+) were measured with a Fabry-Perot, and the low-frequency data (•) were recorded with a *p-i-n* photodiode. The background Lorenztian (dashed curve) is also shown.

identical to Fig. 2.20.

The idea is to use the diffraction grating in conjunction with the single-mode fiber as a narrow bandpass filter. The grating fans the light into its spectral components, and because the coupling efficiency into the fiber is highly sensitive to the position of the beam focus, only those frequency components which are propagating along the fiber/lens axis are efficiently launched into the fiber. By rotating the grating the filter becomes tunable. Quite simply, the fiber/grating system is like a conventional grating spectrometer where the fiber waveguide plays the role of the exit slit.

Measurements on the luminescence from the laser diode below threshold showed that this technique, while somewhat crude, provided a narrow-band filter with a FWHM of approximately 80 GHz. The grating (American Holographic, 2200 grooves/mm) had 85% diffraction efficiency into the first order. Thus by tuning the filter to track one of the modulation sidebands as the modulation frequency is increasing, the carrier could be attenuated without sacrificing much of the sideband power.

Using this filtering technique, we observed one of the modulation sidebands out as far as 77 GHz. However, it was difficult to make a quantitative measurement of the sideband amplitude, as the signal was extremely weak. At these low signal levels, the sideband did not have a definite peak, as in Fig. 2.19, but rather appeared as a fuzzy packet which was barely distinguishable from the background noise. We were thus unable to generate meaningful data points to fit a response function at these high frequencies. Nevertheless, it was important to verify that generation and detection

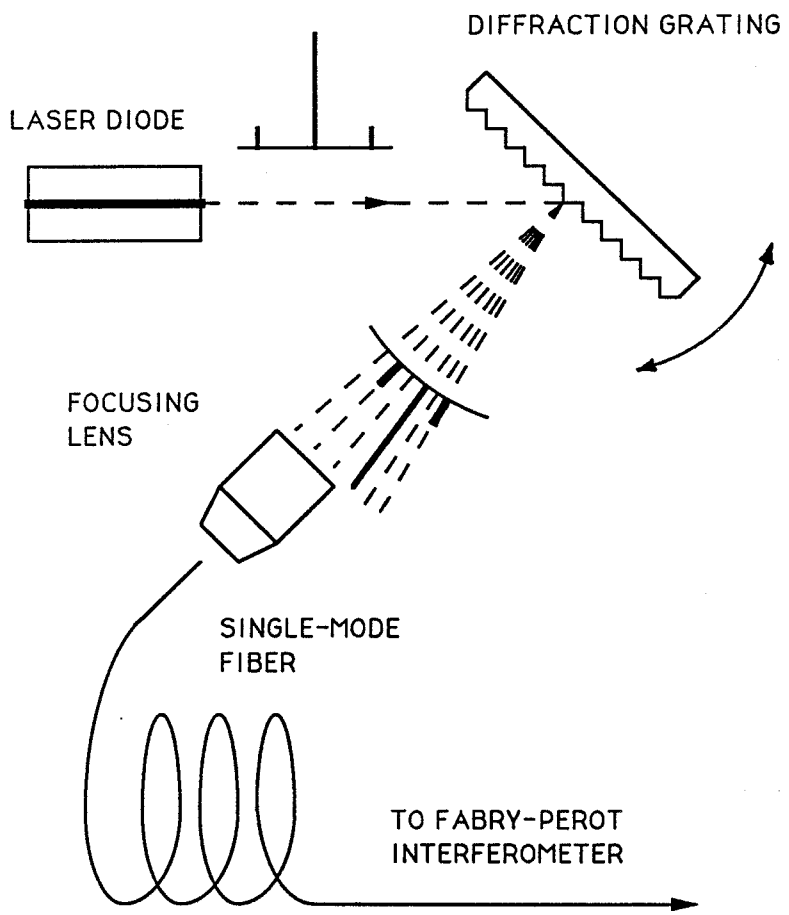

Figure 2.22: Fiber/grating bandpass filter. The field from the modulated laser diode is reflected from a diffraction grating and coupled into the optical fiber. One sideband is efficiently launched into the fiber while the carrier frequency is attenuated.

of semiconductor laser modulation was still possible even at 77 GHz. Further active-layer photomixing experiments with an optimized laser diode and a more sophisticated detection scheme should enable sideband detection well beyond 100 GHz.

2.9 Conclusion

Active-layer photomixing is an optical modulation technique to probe the fundamental modulation response of a semiconductor laser. By heterodyning two laser sources with a tunable frequency difference in the semiconductor laser's active region, the gain, and hence the optical output, is modulated at the beat frequency of the sources. Using an equivalent circuit model for the laser diode, the optical modulation was shown to be decoupled from the electrical parasitics of the laser structure. The fundamental modulation response of the laser can thereby be studied independently of the parasitic response. Under conventional current modulation, on the other hand, the fundamental response would be overwhelmed by the parasitic loading, especially at high frequencies.

The active-layer photomixing technique was used to modulate a GaAs/GaAlAs TJS laser at room temperature, liquid nitrogen and liquid helium temperature. In all cases there was no indication of parasitic effects and the measured response functions appeared to be ideal. The high-frequency decay and dependence of the resonance frequency and damping rate on laser output power agreed with the theoretical predictions. Further photomixing experiments on a GaAs/GaAlAs buried heterostructure laser showed that the modulation response appeared ideal to millimeter-wave

frequencies.

Bibliography

[1] M. A. Newkirk and K. J. Vahala, "Parasitic-free measurement of the fundamental frequency response of a semiconductor laser by active-layer photomixing," *Appl. Phys. Lett.*, vol. 52, pp. 770-772, 1988.

[2] K. J. Vahala and M. A. Newkirk, "Measurement of the intrinsic direct modulation response of a semiconductor laser by photomixing," presented at Conf. on Lasers and Electro-Optics, April 25-29, 1988, Anaheim, CA, paper MG1.

[3] K. J. Vahala and M. A. Newkirk, "Equivalent circuit model for active-layer photomixing: Parasitic-free modulation of semiconductor lasers," *Appl. Phys. Lett.*, vol. 53, pp. 1141-1143, 1988.

[4] M. A. Newkirk and K. J. Vahala, "Low temperature measurement of the fundamental frequency response of a semiconductor laser by active-layer photomixing," presented at 11th Int. Semiconductor Laser Conf., Aug. 29 - Sept. 1, 1988, Boston, MA, postdeadline paper PD14.

[5] M. A. Newkirk and K. J. Vahala, "Low-temperature measurement of the fundamental frequency response of a semiconductor laser by active-layer photomixing," *Appl. Phys. Lett.*, vol. 54, pp. 600-602, 1989.

[6] K. J. Vahala and M. A. Newkirk, "Parasitic-free modulation of semiconductor lasers," *IEEE J. Quantum Electron.* vol. QE-25, pp. 1393-1398, 1989.

[7] M. A. Newkirk and K. J. Vahala, "Measurement of the fundamental modulation response of a semiconductor laser to millimeter wave frequencies by active-layer photomixing," *Appl. Phys. Lett.*, vol. 55, pp. 939-941, 1989.

[8] C. H. Lange, J. Eom, C. B. Su, J. Schlafer, and R. B. Lauer, "Measurement of the intrinsic frequency response of semiconductor lasers using optical modulation," *Electron. Lett.*, vol. 24, pp 1131-1132, 1988.

[9] C. H. Lange and C. B. Su, "Theory and experiment of the parasitic-free frequency response measurement technique using facet-pumped optical modulation in semiconductor diode lasers," *Appl. Phys. Lett.*, vol. 55, pp. 1704-1706, 1989.

[10] J. Eom and C. B. Su, Observation of positive and negative nonlinear gain in an optical injection experiment: Proof of the cavity standing-wave-induced nonlinear gain theory in 1.3 μm wavelength semiconductor diode lasers," *Appl. Phys. Lett.*, vol. 54, pp. 1734-1736, 1989.

[11] J. Eom, C. B. Su, J. S. LaCourse, and R. B. Lauer, "The relation of doping level to K factor and the effect on ultimate modulation performance of semiconductor lasers," *IEEE Photon. Tech. Lett.*, vol. 2, pp. 692-694, 1990.

[12] J. Eom, C. B. Su, W. Rideout, R. B. Lauer, and J. S. LaCourse, "Determination of the gain nonlinearity time constant in 1.3 μm semiconductor lasers," *Appl. Phys. Lett.*, vol. 58, pp. 234-236, 1991.

[13] M. P. Kesler and E. P. Ippen, "Subpicosecond gain dynamics in GaAlAs laser diodes," *Appl. Phys. Lett.*, vol. 51, pp. 1765-1767, 1987.

[14] K. Y. Lau and A. Yariv, "Ultra-high speed semiconductor lasers," *IEEE J. Quantum Electron.*, vol. QE-21, pp. 121-138, 1985.

[15] J. Manning, R. Olshansky, D. M. Fye, and W. Powazinik, "Strong influence of nonlinear gain on spectral and dynamic characteristics of InGaAsP lasers," *Electron. Lett.*, vol. 21, pp. 496-497, 1985.

[16] M. Asada and Y. Suematsu, "Density-matrix theory of semiconductor lasers with relaxation broadening model—Gain and gain-suppression in semiconductor lasers," *IEEE J. Quantum Electron.*, vol. QE-21, pp. 434-442, 1985.

[17] Y. Arakawa, K. Vahala, and A. Yariv, "Quantum noise and dynamics in quantum well and quantum wire lasers," *Appl. Phys. Lett.*, vol. 45, pp. 950-952, 1984.

[18] K. Uomi, T. Mishima, and N. Chinone, "Ultrahigh relaxation oscillation frequency (up to 30 GHz) of highly p-doped GaAs/GaAlAs multiple quantum well lasers," *Appl. Phys. Lett.*, vol. 51, pp. 78-80, 1987.

[19] K. Y. Lau, N. Bar-Chaim, I. Ury, and A. Yariv, "11-GHz direct modulation bandwidth GaAlAs window laser on semi-insulating substrate operating at room temperature," *Appl. Phys. Lett.*, vol. 45, pp. 316-318, 1984.

[20] J. E. Bowers, B. R. Hemenway, T. J. Bridges, E. G. Burkhardt, and D. P. Wilt, "26.5 GHz bandwidth InGaAsP lasers with tight optical confinement," *Electron. Lett.*, vol. 21, pp. 1090-1091, 1985.

[21] K. Y. Lau, N. Bar-Chaim, I. Ury, Ch. Harder, and A. Yariv, "Direct amplitude modulation of short-cavity GaAs lasers up to X-band frequencies," *Appl. Phys. Lett.*, vol. 43, pp. 1-3, 1983.

[22] T. Yuasa, T. Yamada, K. Asakawa, M. Ishii, and M. Uchida, "Very high relaxation oscillation frequency in dry-etched short cavity GaAs/AlGaAs multiquantum well lasers," *Appl. Phys. Lett.*, vol. 50. pp. 1122-1124, 1987.

[23] L. W. Casperson and A. Yariv, "The time behavior and spectra of relaxation oscillations in a high-gain laser," *IEEE J. Quantum Electron.*, vol. QE-8, pp. 69-73, 1972.

[24] R. S. Tucker and D. J. Pope, "Circuit modeling of the effect of diffusion damping in a narrow-stripe semiconductor laser," *IEEE J. Quantum Electron.*, vol. QE-19, pp. 1179-1183, 1983.

[25] R. S. Tucker and I. P. Kaminow, "High-frequency characteristics of directly modulated InGaAsP ridge waveguide and buried heterostructure lasers," *IEEE J. Lightwave Technol.*, vol. LT-2, pp. 385-393, 1984.

[26] K. Y. Lau and A. Yariv, "High-frequency current modulation of semiconductor injection lasers," in *Semiconductors and Semimetals*, edited by W. T. Tsang, Academic Press, New York, vol. 22. part B, pp. 69-151, 1985.

[27] J. Katz, S. Margalit, C. Harder, D. Wilt, and A. Yariv, "The intrinsic electrical equivalent circuit of a laser diode," *IEEE J. Quantum Electron.*, vol. QE-17, pp. 4-7, 1981.

[28] C. Harder, J. Katz, S. Margalit, J. Shacham, and A. Yariv, "Noise equivalent circuit of a semiconductor laser diode," *IEEE J. Quantum Electron.* vol. QE-18, pp. 333-337, 1982.

[29] R. Ulrich, S. C. Rashleigh, and W. Eickhoff, "Bending-induced birefringence in single-mode fibers," *Opt. Lett.*, vol. 5, pp. 273-275, 1980.

[30] S. Kawanishi and M. Saruwatari, "Wideband frequency response measurement of photodetectors using optical heterodyne detection technique," *Electron. Lett.*, vol. 22, pp. 337-338, 1986.

[31] H. Blauvelt, G. Thurmond, J. Parsons, D. Lewis, and H. Yen, "Fabrication and characterization of GaAs Schottky barrier photodetectors for microwave fiber optic links," *Appl. Phys. Lett.*, vol. 45, pp. 195-196, 1984.

[32] K. Y. Lau, Ch. Harder, and A. Yariv, "Direct modulation of semiconductor lasers at $f > 10$ GHz by low-temperature operation," *Appl. Phys. Lett.*, vol. 44, pp. 273-275, 1984.

[33] A. Yariv, *Quantum Electronics*, 2nd ed., New York: Wiley, 1975, pp. 226-227.

[34] H. C. Casey, Jr., and M. B. Panish, *Heterostructure Lasers: Part A*, Orlando: Academic Press, 1978, pp. 173-174.

[35] F. J. Stern, "Calculated spectral dependence of gain in excited GaAs," *J. Appl. Phys.*, vol. 47, pp. 5382-5386, 1976.

[36] J. S. Blakemore, "Semiconducting and other major properties of gallium arsenide," *J. Appl. Phys.*, vol. 53, pp. R123-R181, 1982.

[37] G. P. Agrawal, "Gain nonlinearities in semiconductor lasers: Theory and applications to distributed feedback lasers," *IEEE J. Quantum Electron.*, vol. 23, pp. 434-442, 1987.

[38] C. B. Su, "Nonlinear gain caused by cavity standing wave dielectric grating as an explanation of the relationship between resonance frequency and damping rate of semiconductor diode lasers," *Appl. Phys. Lett.*, vol. 53, pp. 950-953, 1988.

[39] J. E. Bowers, "Millimetre-wave response of InGaAsP lasers," *Electron. Lett.*, vol. 21, pp. 1195-1197, 1985.

[40] 8565A Spectrum Analyzer Operating and Service Manual, Hewlett-Packard Company, 1977.

[41] A. Yariv, *Quantum Electronics*, 2nd ed., New York: Wiley, 1975, p. 141.

[42] Ch. Harder, K. Vahala, and A. Yariv, "Measurement of the linewidth enhancement factor α of semiconductor lasers," *Appl. Phys. Lett.*, vol. 42, pp. 328-330, 1983.

[43] T. L. Koch and J. E. Bowers, "Nature of wavelength chirping in directly modulated semiconductor lasers," *Electron. Lett.*, vol. 20, pp. 1038-1039, 1984.

[44] H. Olesen and G. Jacobsen, "A theoretical and experimental analysis of modulated laser fields and power spectra," *IEEE J. Quantum Electron.*, vol. QE-18, pp. 2069-2080, 1982.

[45] G. P. Agrawal, "Power spectrum of directly modulated single-mode semiconductor lasers: Chirp-induced fine structure," *IEEE J. Quantum Electron.*, vol. QE-21, pp. 680-686, 1985.

Chapter 3

The gain lever: Enhancing the modulation efficiency of quantum well lasers

3.1 Introduction

When the active-layer photomixing technique was used to locally modulate a semiconductor laser with a quantum well active region, it was found that the modulation efficiency was enhanced compared to what was normally observed for a semiconductor laser with a bulk active region, such as the TJS laser discussed in the previous chapter. In some instances, the quantum well laser could be optically modulated with greater than unity quantum efficiency, i.e., one input photon could generate more than one additional lasing photon. This enhancement in the modulation efficiency indicated the presence of a new effect — the gain lever [1], [2].

The gain lever arises in a quantum well because of the special behavior of the optical gain as a function of carrier density. Whereas, in a bulk active layer the optical gain (at the peak of the gain spectrum) is very nearly a linear function of the carrier concentration [3], in a quantum well the gain characteristic is highly sub-linear because of the step-like density of states of a quasi-two-dimensional electron gas [4]. A typical gain function for a 100 Å GaAs quantum well is shown in Fig. 3.1. This curve was calculated using a technique discussed in [5], where a confinement factor $\Gamma = 1/30$ was assumed. The important feature of the gain function is that it saturates at high carrier concentration. As a result, the slope, or differential gain is greater for low carrier density and tends to decrease at higher carrier densities. Therefore, by inhomogeneously pumping a quantum well laser it is possible to create regions in the active layer with unequal differential gain. This is the basis of the gain-lever mechanism. To explore the implications of a sub-linear gain characteristic, an intuitive model is first developed followed by a more rigorous description based on the small-signal rate equations. Finally, experimental results for a two-section GaAs/GaAlAs single quantum well laser show enhanced modulation efficiency and saturation behavior described by the gain-lever mechanism.

3.2 Intuitive model of the gain lever

Assume that we have a quantum well laser divided into two independent sections which comprise a single laser cavity. The two sections are referred to as the control and slave, where the choice of names will become clear presently. The rate equation

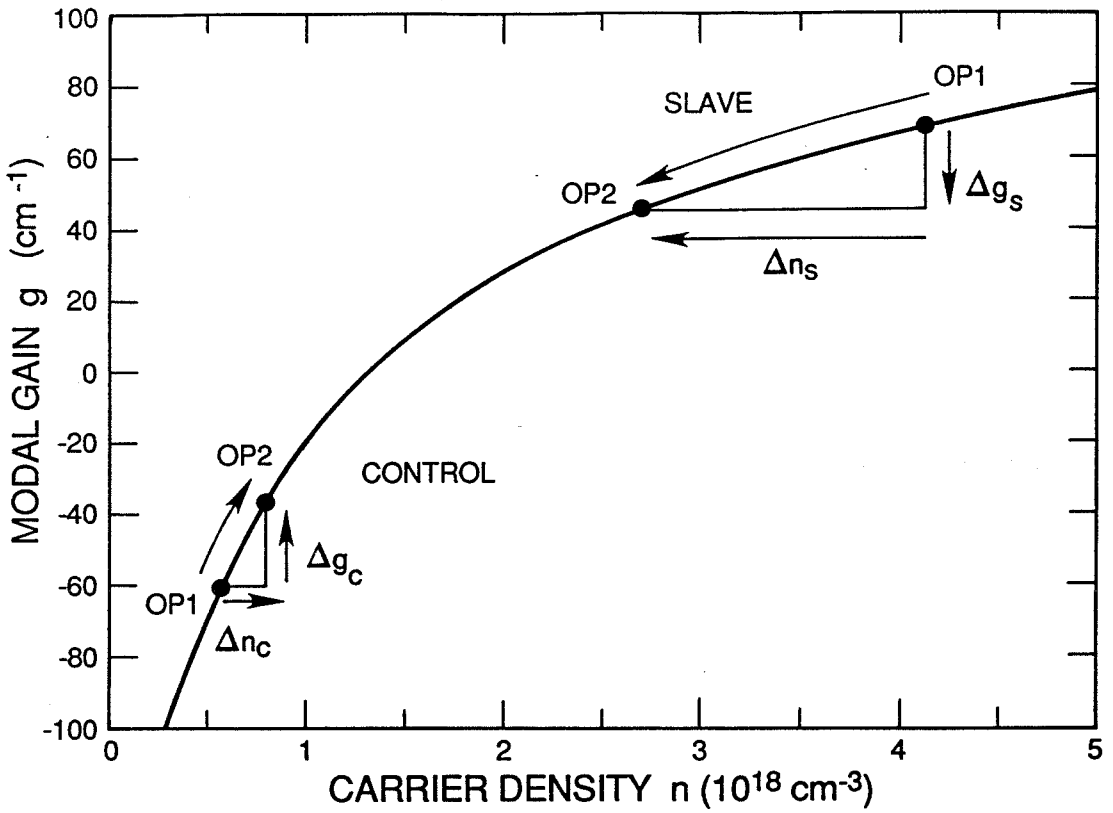

Figure 3.1: Modal gain vs. carrier concentration calculated for a 100 Å GaAs quantum well. This shows the origin of the gain-lever mechanism. When the control and slave regions operate at different excitation levels, a displacement along the gain characteristic in the control causes an enhanced change in the slave.

describing the laser photon dynamics is given by

$$\frac{dP}{dt} = \Gamma_c \Gamma G_c(N_c)P + \Gamma_s \Gamma G_s(N_s)P - \frac{P}{\tau_p} \tag{3.2.1}$$

where the subscript c or s denotes the control or slave section, respectively. In (3.2.1), P is the cavity photon density, G_c (G_s) is the material gain of the control (slave), and Γ is the transverse confinement factor of the optical mode. Γ_c (Γ_s) is the longitudinal confinement factor of the optical mode in the control (slave), accounting for the relative fraction of the total cavity length occupied by each section, so that $\Gamma_c + \Gamma_s = 1$. N_c (N_s) is the carrier density in the control (slave), and τ_p is the photon lifetime. In the final analysis, we will require that the control region occupy a much smaller volume than the slave region, i.e., $\Gamma_c \ll \Gamma_s$. When the control region is relatively small, it is reasonable to treat the photon density as uniform throughout the entire cavity, as in (3.2.1), even though the gain of the two regions may be very different (e.g., the control can be absorbing). Spontaneous emission is also neglected in (3.2.1) to simplify the analysis.

For steady-state conditions (i.e., $\frac{dP}{dt} \rightarrow 0$), we have from (3.2.1)

$$\Gamma_c \Gamma G_c(N_c) + \Gamma_s \Gamma G_s(N_s) - \frac{1}{\tau_p} = 0. \tag{3.2.2}$$

In terms of the modal gain of the control and slave, g_c and g_s, where $g_c \equiv \Gamma G_c$ and $g_s \equiv \Gamma G_s$, (3.2.2) becomes

$$\Gamma_c g_c(N_c) + \Gamma_s g_s(N_s) - \frac{1}{\tau_p} = 0 \tag{3.2.3}$$

which expresses the gain clamping condition for the two-section device. Because the cavity losses are fixed, the overall modal gain, given by the sum of the modal gain

in each region, is clamped to its threshold value. Thus any change in modal gain in the control region must be offset by a complementary change in slave modal gain, or $\Gamma_c \Delta g_c = -\Gamma_s \Delta g_s$. By linearizing the modal gain in each region about the operating point, we have the equivalent constraint

$$\Gamma_c g_c' \Delta n_c = -\Gamma_s g_s' \Delta n_s \tag{3.2.4}$$

where g_i' is the differential modal gain and Δn_i is a small-signal change in carrier density.

Returning to Fig. 3.1, we may intuitively illustrate the gain-lever effect in a two-section quantum well device. To make the figure readable, we assume that the two sections occupy the same volume, so that $\Gamma_c = \Gamma_s$ for the time being. In addition, the laser is above threshold, but is inhomogeneously pumped so that the control and slave regions operate at different excitation levels, shown by operating point 1 (OP1) in the figure. If the carrier density in the control region is now raised by an amount Δn_c, then the modal gain increases by $\Delta g_c = g_c' \Delta n_c$, and the control region operating point moves to OP2. Because of the clamping constraint given by (3.2.4), the slave modal gain must drop by an equal amount. As the slave moves from OP1 to OP2, however, there is an enhanced decrease in carrier density in this region due to the smaller differential gain. But because the carrier injection rate into the slave region is fixed, a decrease in carrier density in this region implies that there must be an increase in the stimulated emission rate into the lasing mode, and corresponding increase in optical output power. This is the basic physical mechanism responsible for the gain lever. Because of the larger differential gain in the control region, a change

in the control carrier density can lever a larger change in the slave region than would otherwise be possible.

3.3 Rate equation formulation of the gain lever

To describe the gain lever in a quantitative way, we write down the coupled rate equations for the photon density and carrier density in the control and slave regions, given by

$$\frac{dP}{dt} = \Gamma_c \Gamma G_c(N_c)P + \Gamma_s \Gamma G_s(N_s)P - \frac{P}{\tau_p} \tag{3.3.1}$$

$$\frac{dN_c}{dt} = -G_c(N_c)P - R_c(N_c) + \Pi_c \tag{3.3.2}$$

$$\frac{dN_s}{dt} = -G_s(N_s)P - R_s(N_s) + \Pi_s \tag{3.3.3}$$

where R_c (R_s) is the spontaneous recombination rate per unit volume in the control (slave), Π_c (Π_s) is the carrier injection rate into the control (slave) in units of carrier density per second, and the other terms are defined after (3.2.1). These equations are solved by first making the following small-signal expansions,

$$P(t) = P_o + p(t) \tag{3.3.4}$$

$$N_i(t) = N_i^o + n_i(t) \tag{3.3.5}$$

$$G_i(N_i) = G_i^o + g_i' n_i \tag{3.3.6}$$

$$R_i(N_i) = R_i^o + \frac{n_i}{\tau_i} \tag{3.3.7}$$

$$\Pi_c(t) = \Pi_c^o + \pi_c(t), \tag{3.3.8}$$

where τ_i is the small-signal spontaneous lifetime and the subscript i signifies c or s to denote the control or slave region, respectively. A small-signal expansion for Π_s

is not needed because the pumping to the slave region is constant. Substituting the above expansions into (3.3.1)–(3.3.3), the following small-signal equations result

$$\frac{dp}{dt} = \Gamma_c \Gamma g_c' P_o n_c + \Gamma_s \Gamma g_s' P_o n_s \tag{3.3.9}$$

$$\frac{dn_c}{dt} = -G_c^o p - g_c' P_o n_c - \frac{n_c}{\tau_c} + \pi_c \tag{3.3.10}$$

$$\frac{dn_s}{dt} = -G_s^o p - g_s' P_o n_s - \frac{n_s}{\tau_s} \tag{3.3.11}$$

where we view π_c as the driving term and p as the response. For steady-state conditions ($\frac{dp}{dt} \rightarrow 0$ and $\frac{dn_i}{dt} \rightarrow 0$), the slave region carrier density can be eliminated from the above equations using the clamping constraint $\Gamma_c g_c' n_c = -\Gamma_s g_s' n_s$. The resulting coupled equations for p and n_c can be written in matrix form as

$$\begin{pmatrix} G_s^o & -(\frac{1}{\tau_s} + g_s' P_o)\frac{\Gamma_c g_c'}{\Gamma_s g_s'} \\ G_c^o & (\frac{1}{\tau_c} + g_c' P_o) \end{pmatrix} \begin{pmatrix} p \\ n_c \end{pmatrix} = \begin{pmatrix} 0 \\ \pi_c \end{pmatrix}. \tag{3.3.12}$$

The 2×2 matrix can then be inverted to yield the response function

$$p = \left(\frac{\Gamma_c}{\Gamma_c G_c^o + \Gamma_s G_s^o \frac{(\frac{1}{\tau_c} + g_c' P_o) g_s'}{(\frac{1}{\tau_s} + g_s' P_o) g_c'}} \right) \pi_c \tag{3.3.13}$$

which describes the small-signal change in the cavity photon density resulting from a change in the control pumping rate.

The analysis is more revealing if (3.3.13) is expressed in terms of the control differential quantum efficiency η_c, i.e., the number of additional output photons produced for every additional carrier injected into the control. When cavity losses are dominated by facet loss (this is true for GaAs quantum well lasers, where internal losses ≤ 2 cm^{-1} are possible [6]), the number of additional output photons (per second) is

$pV/(\Gamma\tau_p) = p(\Gamma_s G_s^o + \Gamma_c G_c^o)V$, where V is the total volume of the active region and V/Γ is the volume of the lasing mode. Because the number of additional input carriers to the control (per second) is $\Gamma_c V \pi_c$, then η_c, the differential quantum efficiency, is given by

$$\eta_c = \frac{\frac{\Gamma_c G_c^o}{\Gamma_s G_s^o} + 1}{\frac{\Gamma_c G_c^o}{\Gamma_s G_s^o} + \frac{(\frac{1}{\tau_c} + g_c' P_o) g_s'}{(\frac{1}{\tau_s} + g_s' P_o) g_c'}}. \tag{3.3.14}$$

Equivalently,

$$\eta_c = \frac{\frac{\Gamma_c G_c^o}{\Gamma_s G_s^o} + 1}{\frac{\Gamma_c G_c^o}{\Gamma_s G_s^o} + \frac{(1 + \frac{P_o}{P_c^{sat}}) P_c^{sat}}{(1 + \frac{P_o}{P_s^{sat}}) P_s^{sat}}} \tag{3.3.15}$$

where the saturation photon density, $P_i^{sat} \equiv 1/(g_i' \tau_i)$. The saturation photon density is a useful quantity because it defines the photon density for which the carrier stimulated lifetime ($1/(g_i' P_o)$) equals the spontaneous lifetime (τ_i).

The gain lever in its most general form, apart from the effects of saturable absorption (see next section), is contained in (3.3.15). Enhancement in modulation efficiency is possible when the control and slave regions operate at unequal saturation photon densities. In particular, we see from (3.3.15) that if $P_c^{sat} < P_s^{sat}$, then η_c can be greater than unity. Conversely, if the control and slave regions operate at equal saturation photon densities, then $\eta_c = 1$, and no enhancement occurs.

3.4 The gain-lever limit and saturable absorption

Although the gain lever can occur in any two-section laser with $P_c^{sat} < P_s^{sat}$, we have not made any definite assumptions about the relative size of the two sections. If

the gain of the two regions is comparable, where $|\Gamma_c G_c^o| \sim |\Gamma_s G_s^o|$, then saturable absorption effects may occur in conjunction with the gain lever. In fact, saturable absorption may completely dominate the modulation behavior of the laser, especially near threshold. However, the gain lever is distinct from conventional saturable absorption. We show that in the gain-lever limit, where $|\Gamma_c G_c^o| \ll |\Gamma_s G_s^o|$, saturable absorption effects vanish, but the gain-lever mechanism persists.

To illustrate the effects of saturable absorption, assume that the control and slave regions are the same size ($\Gamma_c = \Gamma_s$), the control region is unpumped and absorbing ($G_c^o < 0$), the slave region is pumped above transparency ($G_s^o > 0$), but the laser is slightly below threshold. From (3.3.15), the differential quantum efficiency for modulation of the control is given by

$$\eta_c \sim \frac{\dfrac{-|G_c^o|}{G_s^o} + 1}{\dfrac{-|G_c^o|}{G_s^o} + \dfrac{P_c^{sat}}{P_s^{sat}}}. \tag{3.4.1}$$

If the control region saturates differently from the slave, or $P_c^{sat} \neq P_s^{sat}$, then η_c will become singular as the slave region is pumped harder and $\frac{|G_c^o|}{G_s^o} \rightarrow \frac{P_c^{sat}}{P_s^{sat}}$. Roughly speaking, this describes a discontinuous jump in the laser output power as the gain contributed by slave section bleaches the absorption of the control section [7]. Such a laser may be bistable, exhibiting hystersis in output power as a function of pumping to the slave section [8], [9]. It is true that η_c was derived assuming a uniform photon density throughout the cavity, and for the conditions stated above the photon density is certainly not uniform. Nevertheless, this example shows qualitatively how conventional saturable absorption effects may turn the laser into a device with a

highly non-linear transfer characteristic, akin to an optical flip-flop. The important point is that saturable absorption behavior may be predominant when the impact of the control region gain on the lasing mode is comparable to the impact of the slave gain.

In order to avoid effects due to conventional saturable absorption, we must require that any saturable loss from the control be insignificant compared to the nonsaturable losses in the cavity. This can be ensured by limiting the control region to a small fraction of the total cavity volume, so that $\Gamma_c \ll \Gamma_s$. In this case, the direct effect of the control region gain on the lasing is completely negligible. Thus in the gain-lever limit, where $\Gamma_c G_c^o / \Gamma_s G_s^o \to 0$, we have from (3.3.15)

$$\eta_c = \frac{P_s^{sat}(1 + \frac{P_o}{P_s^{sat}})}{P_c^{sat}(1 + \frac{P_o}{P_c^{sat}})}. \tag{3.4.2}$$

Equation (3.4.2) reveals the gain lever without the complications of conventional saturable absorption. There are three important features of this result. First, the modulation enhancement is seen to be independent of the actual size of the control and slave regions, so long as the condition $\Gamma_c G_c^o / \Gamma_s G_s^o \to 0$ is satisfied. Second, at low power, where $P_o \ll P_i^{sat}$, the modulation enhancement is governed by the ratio of the saturation photon densities in the two regions. The maximum enhancement is thus given by

$$\eta_c^{max} = \frac{P_s^{sat}}{P_c^{sat}} = \frac{g_c' \tau_c}{g_s' \tau_s}. \tag{3.4.3}$$

Although the the intuitive model (see Fig. 3.1) indicated that the amount of leverage depends on the ratio of differential gains in the two regions, (3.4.3) shows that the ratio of the saturation photon densities is the controlling variable. Third, at high

output power, where $P_o \gg P_i^{sat}$, the gain lever becomes less effective. Ultimately, the differential quantum efficiency approaches unity, describing a one-for-one conversion of input carriers to the control to output lasing photons. This negation of the gain lever at large intracavity photon densities is merely a lifetime effect. Quite simply, as $P_o \rightarrow \infty$, the control carrier lifetime is dominated by its stimulated component $(1/(g_c' P_o))$ which tends to saturate the inversion. It thus becomes more difficult to affect the control region carrier concentration, and hence the control gain, by modulating the pumping to this section.

3.5 Implementation of the gain lever

As stated above, the gain lever in its most general form (3.3.15) occurs in any two-section laser where $P_c^{sat} < P_s^{sat}$. However, a quantum well laser provides an ideal structure in which to implement the effect. In a quantum well, the two components of saturation photon density, carrier spontaneous lifetime and differential gain, are dependent on carrier concentration (more so for differential gain). It is thus a simple matter to force $P_c^{sat} < P_s^{sat}$ by inhomogeneously pumping the quantum well active layer.

Differential modal gain as a function of carrier concentration for a typical 100 Å GaAs quantum well appears in Fig. 3.2. This is the derivative of the gain characteristic in Fig. 3.1. As the carrier density is reduced, the differential gain rises considerably. By pumping the control region to low excitation compared to the slave, the ratio of differential gains in the two regions can be made rather large.

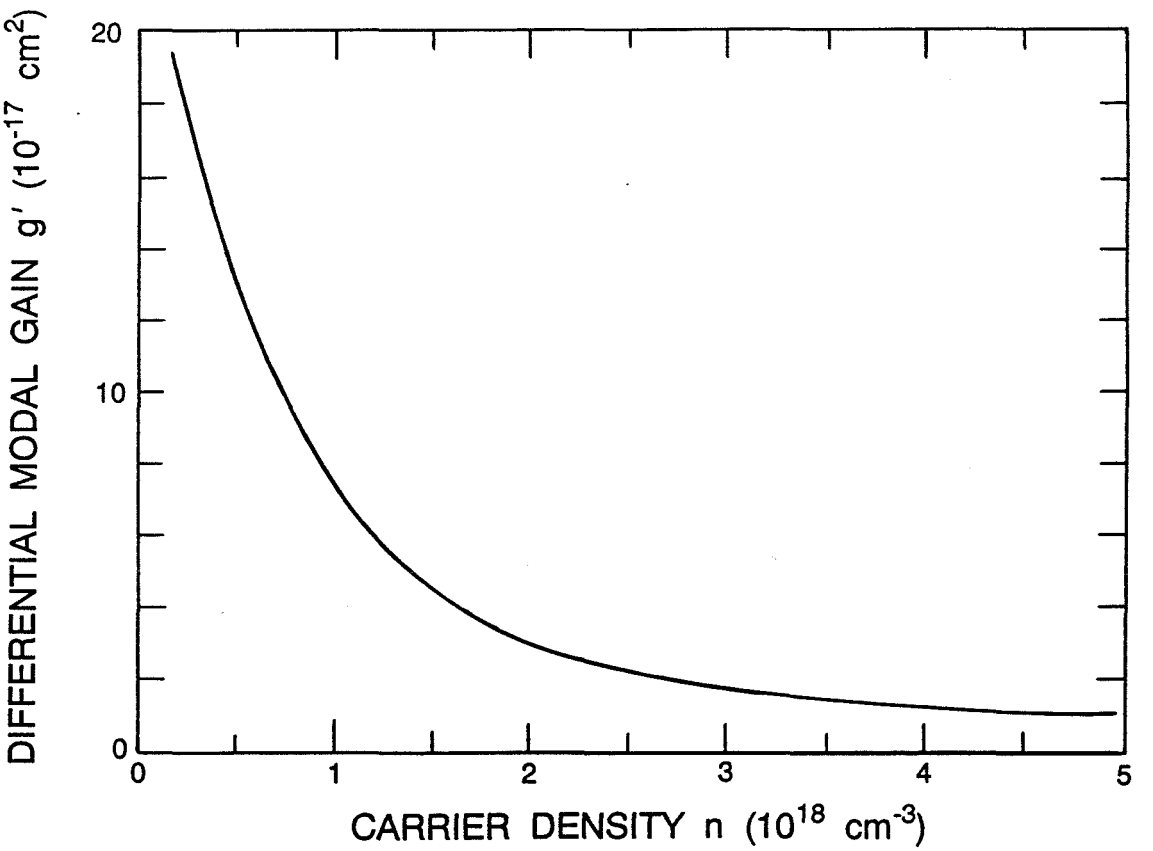

Figure 3.2: Differential modal gain as a function of carrier density for a 100 Å GaAs quantum well. This is the derivative of the gain function in Fig. 3.1.

However, the spontaneous carrier lifetime is also dependent on the carrier density, so this will affect the ratio of the saturation photon densities as well. The spontaneous recombination rate can be expressed as a power series in N,

$$R(N) = AN + BN^2 + CN^3 \tag{3.5.1}$$

where A, B, and C are the non-radiative, radiative, and Auger recombination coefficients for the semiconductor material, respectively. In terms of the small-signal spontaneous lifetime in the control and slave regions,

$$\frac{d}{dN}R(N)\Big|_{N=N_i^o} \equiv \frac{1}{\tau_i} = A + 2BN_i^o + 3C(N_i^o)^2, \tag{3.5.2}$$

so that the spontaneous lifetime is generally a decreasing function of carrier density. Experimentally, it is found that τ_i for an undoped GaAs quantum well at room temperature is dominated by band-to-band radiative recombination [10], so $\frac{1}{\tau_i}$ is nearly a linear function of N_i^o. $2B$ was determined to be 5×10^{-10} cm^3 sec^{-1} for a 100 Å well over a wide range of carrier densities (10^{16} cm^{-3} – 10^{18} cm^{-3}).

Thus, in a quantum well, both differential gain and spontaneous lifetime decrease as carrier density increases. Therefore, to ensure $P_c^{sat} < P_s^{sat}$, the control should be pumped to a lower level of excitation than the slave. In addition, the control section should be small so that saturable absorption effects do not occur. Figure 3.3 shows such a two-section laser with the small control section adjacent to one facet. The slave region is pumped by a dc injection current and the control region is separately modulated either optically or electrically.

In order to relate the theoretical gain-levered modulation enhancement to experiment, (3.4.2) can be expressed in terms of output power from the laser. Non-ideal

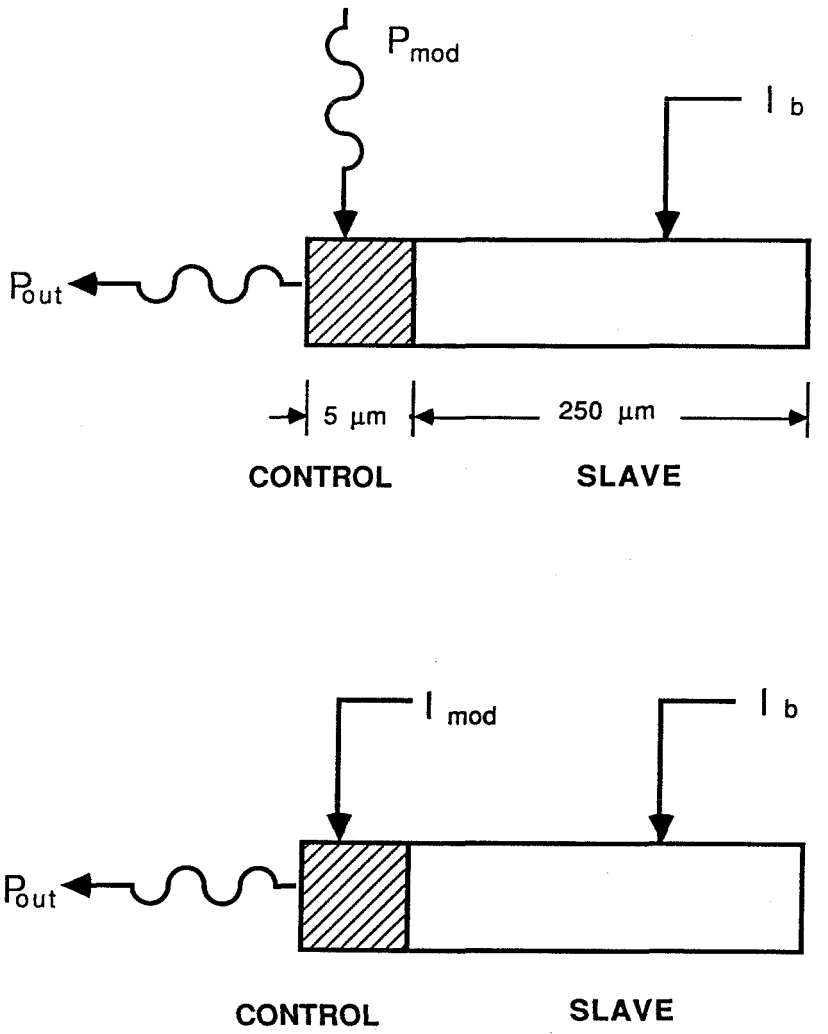

Figure 3.3: The laser is composed of two separate regions, the control and the slave, where the control is only a small fraction of the total cavity volume. A dc current I_b applied to the slave region biases the laser above threshold. The control region is modulated optically or electrically.

coupling should also be accounted for, because not all of the input modulation energy to the control will reach the active layer. For electrical modulation, the ratio of output power modulation to input current modulation is given by

$$\frac{\Delta P_o}{\Delta I_i} = \kappa_I \frac{hc}{\lambda_o q}\eta_c = \kappa_I \frac{hc}{\lambda_o q}\frac{P_s^{sat}(1+\frac{P_o}{P_s^{sat}})}{P_c^{sat}(1+\frac{P_o}{P_c^{sat}})} \tag{3.5.3}$$

where κ_I is the coupling efficiency for current into the control, h, c, and q are Planck's constant, the speed of light, and the electron charge, respectively. λ_o is the laser wavelength, and η_c is the differential quantum efficiency defined in (3.4.2). For optical modulation of the control, the ratio of output power modulation to input power modulation is

$$\frac{\Delta P_o}{\Delta P_i} = \kappa_P \frac{\lambda_i}{\lambda_o}\eta_c = \kappa_P \frac{\lambda_i}{\lambda_o}\frac{P_s^{sat}(1+\frac{P_o}{P_s^{sat}})}{P_c^{sat}(1+\frac{P_o}{P_c^{sat}})} \tag{3.5.4}$$

where λ_i is the input wavelength and κ_P is the coupling efficiency for the input light. Thus, for optical modulation, κ_P carriers are created through optical absorption for every input photon to the control. Also, the power gain $\frac{\Delta P_o}{\Delta P_i}$ is decreased by the ratio $\frac{\lambda_i}{\lambda_o}$, where $\lambda_i < \lambda_o$ in order that the input photons are above the bandgap of the active layer material and therefore absorbed.

3.6 Experimental results

To demonstrate the gain-lever effect, we study a GaAs/GaAlAs laser with a 100 Å single quantum well (SQW). The experimental setup is shown in Fig. 3.4. The laser is biased above threshold by a dc injection current applied through a metal contact over nearly the full cavity length. This defines the slave region. A small opening in

the metal contact adjacent to one of the facets defines the control region which is unpumped by the bias current. This opening permits the control region to be optically modulated. Figure 3.5 shows the top surface of the laser diode. For this laser, the control region is 5 μm long compared to a slave region 250 μm in length. The control thus forms 2% of the cavity volume—a very small slice—so we are definitely operating in the gain-lever limit where saturable absorption is not a factor (see (3.4.2)). For argument's sake, even if the control region has an absorption coefficient of approximately 50 cm^{-1}, as depicted in Fig. 3.1, then the impact of 50 cm^{-1} absorption over a 5 μm length is miniscule.

For optical pumping of the control we use a cw Kr laser operating at 676 nm. Although the gain-lever effect was initially discovered while photomixing two lasers in the control section (modulation enhancement was observed out to several GHz), for the experiment discussed here only one laser is used to provide the control input. This allows the gain lever to be characterized in the steady-state regime ($\frac{dn_c}{dt} \rightarrow 0$) simply by varying the incident Kr power. The output power from one (or both) of the SQW laser facets is then monitored with a *p-i-n* detector.

A cross section of the SQW laser is shown in Fig. 3.6. The quantum well active layer is embedded in a graded index separate confinement heterostructure (GRINSCH). Although the GRINSCH is a standard component of a high-performance quantum well laser [11], the presence of the GRINSCH is important for efficient optical modulation of the control. Even though the input light at 676 nm is well above the bandgap of GaAs, very little ($\sim$ 1%) of the input is directly absorbed by the active

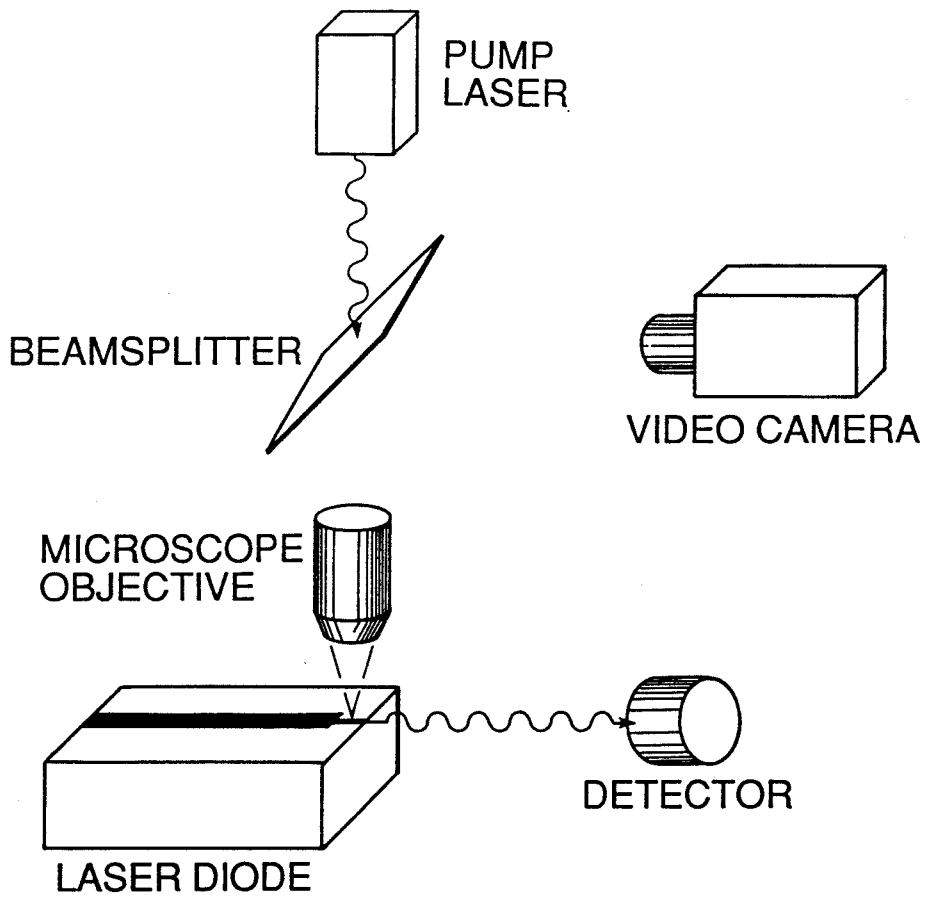

Figure 3.4: Schematic diagram of the experimental setup. The quantum well laser diode is biased above threshold by a dc injection current, while a small region of the active layer is optically pumped by a Kr laser. The change in ouput power is monitored by a photodetector.

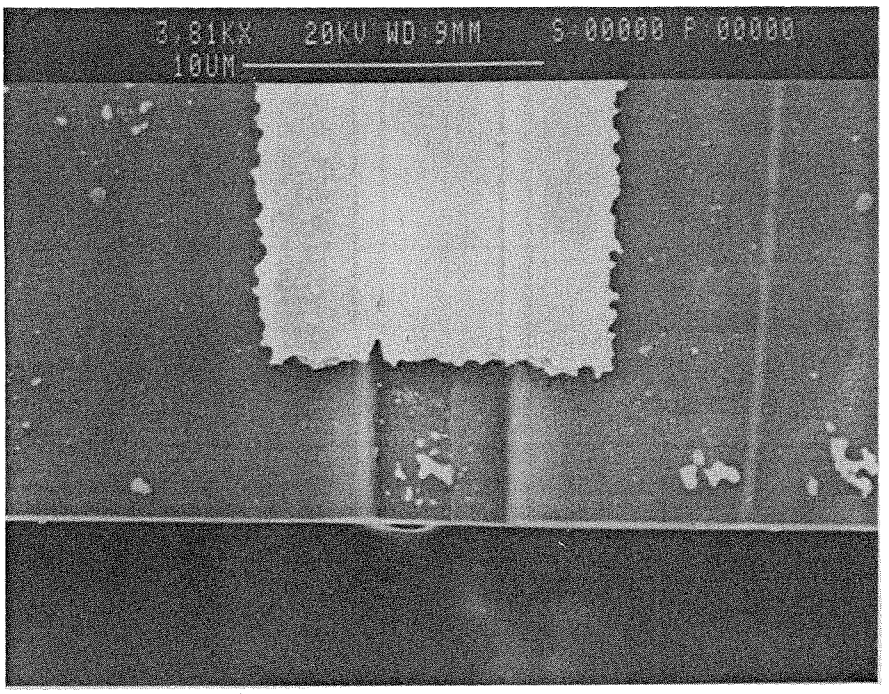

Figure 3.5: Scanning electron micrograph of the top surface of the quantum well laser. A 5 μm opening in the metal contact adjacent to the facet defines the control region which may be optically modulated.

region since it has a thickness of only 100 Å. Fortunately, most of the input absorption occurs in the GRINSCH, and the photocarriers are then quickly swept into the well by the built-in electric field arising from the GRINSCH's graded bandgap. In fact, the carrier capture time (GRINSCH $\rightarrow$ quantum well) is on the order of ps, as recent photoluminescence studies have shown [12]. Based on a 30% Fresnel reflection from the top surface, and an estimated 30% absorption by the GRINSCH and SQW, approximately 20% of the incident Kr photons are converted into control carriers.

Figure 3.7 shows data from the modulation experiment, where the change in total output power (both facets) from the SQW laser is plotted as a function of the absorbed input power in the control (ΔP_o vs. $\kappa_P \Delta P_i$ from (3.5.4)). The SQW laser had a threshold current of 27 mA and lasing wavelength of 850 nm. Characteristics are shown for slave bias currents (I_b) from 28 mA up to 45 mA, where the output power from the SQW with no control input (P_b) ranges from 1.4 mW to 14.5 mW. At low laser bias, the ratio of output power modulation to input Kr power is as high as four. As the bias level increases the modulation enhancement decreases, but for $I_b > 45$ mA the characteristics were no different from the $I_b = 45$ mA characteristic. However, this form of saturation is predicted by (3.4.2). At high slave bias current, the large P_o limit of (3.4.2) is approached, where the gain lever is negated by the lifetime-related saturation of the control population. There is no power gain, merely a one-for-one conversion of absorbed input photons to output photons. In the high-power limit, (3.5.4) predicts $\frac{\Delta P_o}{\kappa_P \Delta P_i} = \frac{\lambda_i}{\lambda_o}$. The measured slope of the characteristic at high bias is in satisfactory agreement with this value, with $\frac{\lambda_i}{\lambda_o} = \frac{676\,\text{nm}}{850\,\text{nm}} = 0.79$.

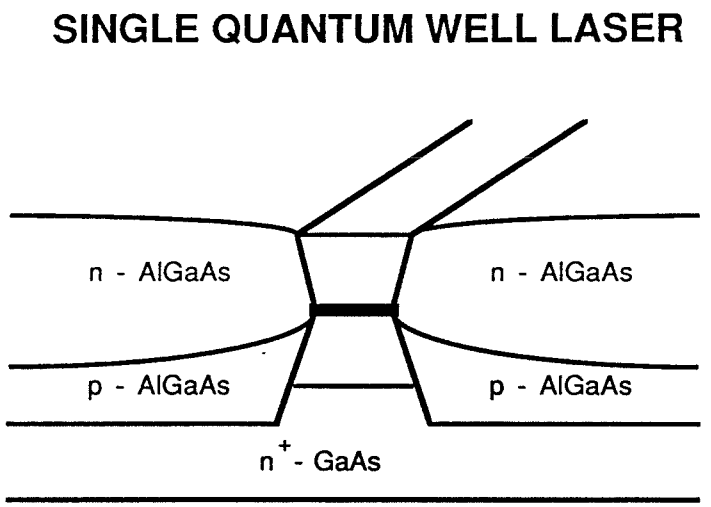

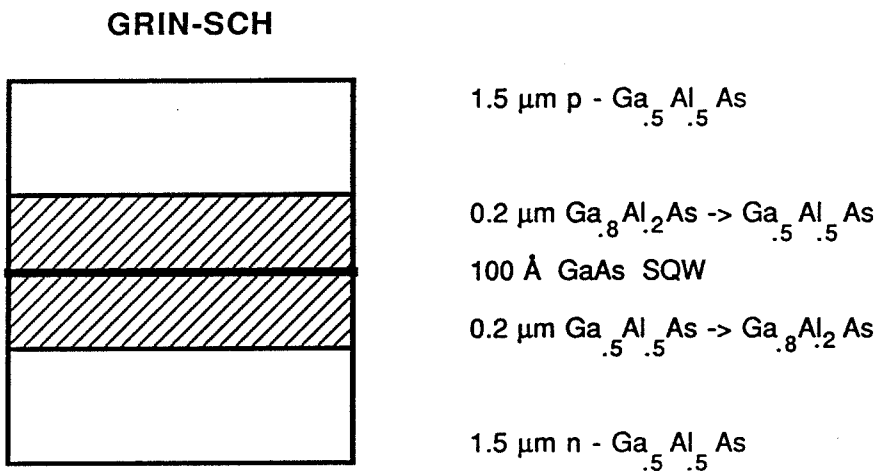

Figure 3.6: Schematic cross section of the GaAs/GaAlAs laser with a single 100 Å quantum well. The active layer is surrounded by a graded index separate confinement heterostructure (GRINSCH), wherein most of the absorption of input light occurs.

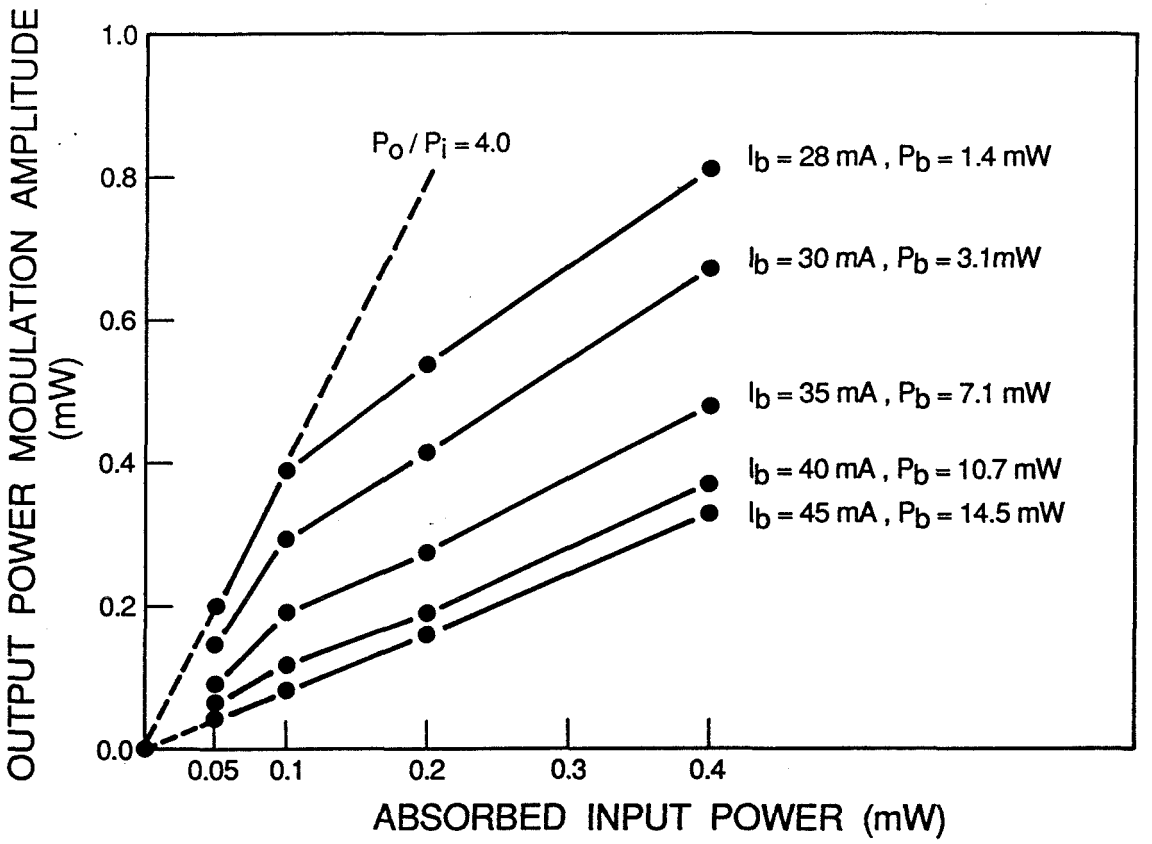

Figure 3.7: Change in the output power (both facets) from the laser diode vs. absorbed optical input power for different slave region bias levels.

The measured factor of four enhancement in modulation efficiency is reasonable in view of the following argument. Because the control region is unbiased, the control junction voltage, and hence the control carrier density N_c^o, is floating. The control is thus easily bleached by the lasing mode, pushing this region close to transparency. The transparency point in Fig. 3.1 corresponds to a control carrier density of about 1.3×10^{18} cm^{-3}. The location of OP1 for the slave is most likely near 50 cm^{-1}, which is a reasonable threshold gain for a 255 μm long GaAs SQW laser with uncoated facets (threshold gain $= \frac{1}{L}\ln(\frac{1}{r})$ insofar as internal loss is negligible, where L is the cavity length and r is the facet reflectivity, $\sim 30\%$ for GaAs). The slave carrier density N_s^o thus lies near 3.0×10^{18} cm^{-3}. As a result, from Fig. 3.2, the ratio of the differential gains in the control and slave is about 2.5, while the ratio of the spontaneous lifetimes in the two regions is about 2.3, assuming the lifetime is inversely proportional to the carrier density (see (3.5.2)). This gives $P_c^{sat}/P_s^{sat} = 5.8$ for the maximum modulation enhancement, not far from the measured factor of 4.0. It is also true that the control was not electrically isolated from the slave. Consequently, there may have been some leakage of slave carriers into the control which would further diminish the amount of modulation enhancement that could be obtained.

In addition to the photon density related saturation discussed above, another form of saturation is apparent in the data in Fig. 3.7. A characteristic for a fixed slave bias will saturate as the input power to the control increases. This is most visible in the low bias characteristic ($I_b = 28$ mA) where the modulation enhancement decreases for input powers above about 0.1 mW. This type of saturation must be distinct from

the photon density related saturation. The reason is that the slope of the $I_b = 28$ mA characteristic is reduced to about 1.4 when the device output power is 1.8 mW, yet the slope of the next characteristic ($I_b = 30$ mA) is as large as 3.0 when the output power is increased to 3.1 mW. The saturation displayed by the $I_b = 28$ mA characteristic is most likely due to band filling, whereby the carrier density in the control region increases enough to increase the effective saturation photon density of this region. In other words, as the control is pumped harder by the Kr laser, the operating point OP2 in Fig. 3.1 moves up the gain curve to such a degree that the differential gain and carrier lifetime are decreased. Thus the ratio of saturation photon densities of the two regions is reduced, resulting in a less effective gain lever. This form of saturation is not contained in the theoretical results, because it must be remembered that (3.4.2) was derived by separately linearizing the gain in the control and slave regions. If the control is modulated too hard, then the linear approximation for the control gain must be modified. In fact, for a control volume of 3 μm $\times$ 5 μm $\times$ 100 Å and spontaneous lifetime of 1.5 ns (in accordance with (3.5.2)), then only 0.03 mW of absorbed Kr power is needed to boost the control carrier density by 1×10^{18} cm^{-3}. The lesson is that to avoid band-filling saturation of the control region, the modulation to this section must definitely be small-signal.

3.7 Improvements and future applications

There are many possible ways to improve the performance of the gain lever. To enhance the intensity modulation efficiency, one should consider ways to increase the

ratio of saturation photon density of the control and slave regions. This may be accomplished by forcing the slave to run at higher excitation, thus pushing the slave operating point further out on the gain characteristic, or by n-type doping the slave region, which tends to further flatten the gain characteristic compared to the undoped case [5]. To increase the saturation power due to band-filling effects, one could put multiple quantum wells in the control section, so that the carrier density in each well is reduced in proportion to the number of wells. For optical modulation, the overall quantum efficiency could be improved by increasing the absorption cross-section of the control region and by eliminating the Fresnel reflection from the control region surface. Furthermore, the control and slave sections should be electrically isolated so they form independent carrier populations.

While optical modulation of the control section provided a convenient means to initially demonstrate the gain lever, it should be clear that a more practical way to implement the effect is by current pumping both the control and slave sections through separate electrical contacts, as in Fig. 3.3. In this case, the two regions may be individually biased to force $P_c^{sat} \ll P_s^{sat}$. Indeed, this approach was demonstrated by Moore and Lau [13] subsequently to, and independently of, our gain-lever experiments [1], [2]. They observed up to 23 dB enhancement in the intensity modulation efficiency of a two-section SQW GaAs/GaAlAs laser similar to our device. Gajic and Lau found that intensity noise from gain-levered lasers is only marginally increased compared to homogeneous pumping [14].

Finally, although this aspect of the gain lever was not pursued in our laboratory,

the gain lever may also enhance the tunability of semiconductor lasers. Because the slave region carrier concentration can be controlled by gain-levering (unlike a homogeneously pumped laser where the carrier density is clamped), the longitudinal cavity resonances, and hence the lasing frequency, may easily be tuned by way of the carrier-density dependent refractive index. With this in mind, a gain-levered multiple quantum well DFB laser with 6.1 nm tuning range was fabricated by Wu and co-workers [15]. Very recently, Lau reported enhanced FM response [16], up to 20 GHz per mA of control current, and large tunability [17], over 90 Å, for a gain-levered SQW laser. This feature of the gain lever may prove to be important for the future development of tunable semiconductor lasers.

3.8 Conclusion

The gain lever is an effect, discovered in our laboratory, which enhances the modulation efficiency of quantum well semiconductor lasers. Intuitively, the effect occurs in quantum wells because of the sub-linear dependence of optical gain on carrier concentration. Thus, by inhomogeneously pumping the laser, it is possible to create two regions with unequal differential gain. If the laser is above threshold, then the overall modal gain is clamped, and by modulating the pumping to the section with higher differential gain, the output power from the laser can be modulated with greater than unity quantum efficiency. The gain lever was explained theoretically using simple rate equations describing a two section laser. It was found in the general case that the only requirement for a gain lever is that the two regions have unequal saturation

photon densities (the saturation photon density is the inverse of the product of differential gain and carrier spontaneous lifetime). Furthermore, in order that conventional saturable absorption effects do not occur, it is necessary that the region with smaller saturation photon density (the control section) occupy a small fraction of the total cavity volume. Finally, experimental results for a two-section GaAs/GaAlAs single quantum well laser show modulation enhancement and saturation behavior described by the gain-lever mechanism.

Bibliography

[1] M. A. Newkirk, K. J. Vahala, T. R. Chen, and A. Yariv, "A novel gain mechanism in an optically modulated single quantum well semiconductor laser," presented at Conf. on Lasers and Electro-Optics, April 24-28, 1989, Baltimore, MD, paper WG1.

[2] K. J. Vahala, M. A. Newkirk, and T. R. Chen, "The optical gain lever: A novel gain mechanism in the direct modulation of quantum well semiconductor lasers," *Appl. Phys. Lett.*, vol. 54, pp. 2506-2508, 1989.

[3] C. H. Henry, R. A. Logan, and F. R. Merritt, "Measurement of gain and absorption spectra in AlGaAs buried heterostructure lasers," *J. Appl. Phys.*, vol. 51, pp. 3042-3050, 1980.

[4] Y. Arakawa and A. Yariv, "Theory of gain, modulation response, and spectral linewidth in AlGaAs quantum well lasers," *IEEE J. Quantum Electron.*, vol. QE-21, pp. 1666-1674, 1985.

[5] K. J. Vahala and C. E. Zah, "Effect of doping on the optical gain and the spontaneous noise enhancement factor in quantum well amplifiers and lasers studied by simple analytical expressions," *Appl. Phys. Lett.*, vol. 52, pp. 1945-1947, 1988.

[6] M. Mittelstein, Y. Arakawa, A. Larsson, and A. Yariv, "Second quantized state lasing of a current pumped single quantum well laser," *Appl. Phys. Lett.*, vol. 49, pp. 1689-1691, 1986.

[7] A. E. Siegman, *Lasers*, Mill Valley, CA: University Science Books, 1986, p. 538.

[8] C. S. Harder, "Bistability, high-speed modulation, noise, and pulsation in GaAlAs semiconductor lasers," Ph.D. dissertation, California Instit. Technol., Pasadena, CA, 1983, ch. 4.

[9] H. Kawaguchi, "Bistable operation of semiconductor lasers by optical injection," *Electron. Lett.*, vol. 17, pp. 741-742, 1981.

[10] Y. Arakawa, H. Sakaki, M. Nishioka, J. Yoshino, and T. Kamiya, "Recombination lifetime of carriers in GaAs-GaAlAs quantum wells near room temperature," *Appl. Phys. Lett.*, vol. 46, pp. 519-521, 1985.

[11] P. L. Derry, "Properties of buried heterostructure single quantum well (Al,Ga)As lasers," Ph.D. dissertation, California Instit. Technol., Pasadena, CA, 1989, ch. 2.

[12] B. Deveaud, F. Clerot, A. Regreny, K. Fujiwara, K. Mitsunaga, and J. Ohta, "Capture of photoexcited carriers by a laser structure," *Appl. Phys. Lett.*, vol. 55, pp. 2646-2648, 1989.

[13] N. Moore and K. Y. Lau, "Ultrahigh efficiency microwave signal transmission using tandem-contact single quantum well GaAlAs lasers," *Appl. Phys. Lett.*, vol. 55, pp. 936-938, 1989.

[14] D. Gajic and K. Y. Lau, "Intensity noise reduction in the ultrahigh efficiency tandem-contact quantum well lasers," *Appl. Phys. Lett.*, vol. 57, pp. 1837-1839, 1990.

[15] M. C. Wu, Y. K. Chen, T. Tanbun-Ek, R. A. Logan, and A. M. Sergent, "Gain-levering enhanced continuous wavelength tuning (6.1 nm) in two-section strained multiquantum well DFB lasers," presented at Conf. on Lasers and Electro-Optics, May 21-25, 1990, Anaheim, CA, postdeadline paper CPDP30.

[16] K. Y. Lau, "Frequency modulation and linewidth of gain-levered two-section single quantum well lasers," *Appl. Phys. Lett.*, vol. 57, pp. 2068-2070, 1990.

[17] K. Y. Lau, "Broad wavelength tunability in gain-levered quantum well semiconductor lasers," *Appl. Phys. Lett.*, vol. 57, pp. 2632-2634, 1990.

Chapter 4

Amplitude-phase decorrelation: Reduction of semiconductor laser intensity noise

4.1 Introduction

The α parameter, or linewidth enhancement factor, has been studied extensively in research on semiconductor lasers. It governs many of the the important features of semiconductor laser dynamics, among them enhanced linewidth [1] and frequency chirp under direct modulation (dynamic line broadening) [2], [3].

In a semiconductor laser, the resonant refractive index and the gain are functions of carrier concentration. The amplitude and phase of the lasing field are therefore strongly coupled through the carrier population in the active region. The α parameter is simply a measure of the coupling strength. However, the coupling is not symmetric.

Field amplitude fluctuations are coupled into phase fluctuations, but not the reverse. With regard to laser noise, this one-way coupling causes excess phase noise which enhances the fundamental laser linewidth by a factor of $1 + \alpha^2$, but the fundamental intensity noise level is unaffected. Nevertheless, the coupling further implies that the amplitude and phase fluctuations are *correlated.* Because of the inherent correlation between the fluctuations, an "image" of the intensity noise lies in the phase noise. We propose that this image can be recovered from the phase fluctuation (more precisely, the time derivative of the phase fluctuation, or instantaneous frequency fluctuation) and used to reduce the intensity noise far below its intrinsic level. When the intensity noise is maximally reduced, the fluctuations become decorrelated.

In this chapter, a discussion of two methods to achieve intensity noise reduction is presented [4]. The first approach employs a passive element with a frequency-dependent transmission which is external to the laser cavity [5], [6]. The theoretical basis of this method is outlined, and the theory is applied to calculate the spectrum of noise reduction, as well as the correlation properties of the transformed field fluctuations. The effects of a power-independent component of laser linewidth on the noise reduction are also considered. In the second approach, a frequency-dependent loss is placed inside the laser cavity. Many of the effects due to such a dispersive intracavity loss have been considered previously in the context of "detuned loading" [17], but application to intensity noise reduction was not developed. Both methods may potentially reduce the fundamental intensity noise floor by the factor $1/(1+\alpha^2)$, well over an order of magnitude for typical values of α. Finally, results of an experiment

which verify the first approach are discussed. The intensity noise level of a DFB laser at low bias is passively reduced as much as a factor of 28 (14.5 dB) below its intrinsic level by amplitude-phase decorrelation.

4.2 Semiconductor laser noise

In this section, the main features of intrinsic noise in semiconductor lasers which will be important for later discussion of noise reduction are outlined. A semiclassical description of the field fluctuations incorporating Langevin noise sources is used to derive the relevant noise spectra and their dependence on laser power. At the center of this discussion is the α parameter, which characterizes the coupling between amplitude and phase fluctuations in the field.

The electric field from a single mode laser can be described as follows,

$$E(t) = \sqrt{p_o + p(t)}\; e^{i(\omega_L t + \varphi(t))} \tag{4.2.1}$$

where p_o is the average photon density in the lasing mode, $p(t)$ is the fluctuating part of the photon density, ω_L is the cw oscillation frequency, and $\varphi(t)$ is the fluctuating phase deviation. When $p(t)/p_o \ll 1$ the field can be represented in terms of a dimensionless fluctuating amplitude

$$E(t) = \sqrt{p_o}\,(1 + \rho(t))\, e^{i(\omega_L t + \varphi(t))} \tag{4.2.2}$$

where $\rho(t) = p(t)/2p_o$. As depicted in the intuitive model of Henry [7], the fluctuations arise from spontaneous emission which randomly perturbs the amplitude and phase of the field phasor. Since a semiconductor laser operates as a detuned oscillator–i.e.,

the gain peak lies at a frequency different from the zero dispersion point of the resonant refractive index–the amplitude fluctuations cause enhanced phase fluctuations by modulating the carrier density-dependent refractive index of the gain medium. This phase noise enhancement is measured by the α parameter, given in terms of the real and imaginary parts of the complex susceptibility function as

$$\alpha = \frac{d\chi_R(n)/dn}{d\chi_I(n)/dn} \tag{4.2.3}$$

where n is the carrier density. As defined above, α is a negative number. For DFB semiconductor lasers, α may range from -2 to -7 depending on device design [8].

Each of the quantities $\rho(t)$, $\varphi(t)$, and $n(t)$, the deviation of carrier density from the steady-state value, evolves according to the small-signal rate equations, given by

$$\dot{\rho}(t) = G'n/2 + \Delta_R \tag{4.2.4}$$

$$\dot{\varphi}(t) = -\alpha G'n/2 + \Delta_I \tag{4.2.5}$$

$$\dot{n}(t) = -n/\tau_R - 2p_o G\rho \tag{4.2.6}$$

where G is the optical gain, G' is the derivative of gain with respect to carrier density, τ_R is the relaxation oscillation damping time, and Δ_R and Δ_I are real and imaginary parts of the Langevin force accounting for spontaneous emission into the lasing mode [9]. We omit a noise term in the carrier density equation because it has a negligible effect on the dynamics of $\rho(t)$ and $\varphi(t)$ when the laser operates at low bias in the excess noise regime, described below [10], [11]. The Langevin forcing terms are assumed to come from a zero-mean Gaussian probability distribution and have the

correlation relations [12]

$$\langle \Delta_R(t+\tau)\Delta_R(t)\rangle = \frac{S}{2P}\delta(\tau) \tag{4.2.7}$$

$$\langle \Delta_I(t+\tau)\Delta_I(t)\rangle = \frac{S}{2P}\delta(\tau) \tag{4.2.8}$$

$$\langle \Delta_R(t+\tau)\Delta_I(t)\rangle = 0 \tag{4.2.9}$$

where S is the spontaneous emission rate into the lasing mode, P is the average photon number in the mode, and $\delta(\tau)$ is the Dirac delta function. The angle brackets denote ensemble averaging. By Fourier transforming the above rate equations with respect to frequency Ω, the dynamics of n can be absorbed into equations for ρ and $\dot{\varphi}$, the instantaneous frequency deviation, to obtain the fluctuation spectra

$$\rho(\Omega) = \frac{\frac{1}{\tau_R} + i\Omega}{(\omega_R^2 - \Omega^2) + \frac{i\Omega}{\tau_R}}\tilde{\Delta}_R \tag{4.2.10}$$

$$\dot{\varphi}(\Omega) = \tilde{\Delta}_I + \frac{\alpha\omega_R^2}{(\omega_R^2 - \Omega^2) + \frac{i\Omega}{\tau_R}}\tilde{\Delta}_R. \tag{4.2.11}$$

Here, $GG'p_o$ has been replaced by ω_R^2, the relaxation oscillation frequency squared. By Parseval's theorem, the transformed Langevin terms, $\tilde{\Delta}_R$ and $\tilde{\Delta}_I$, are delta-correlated in frequency with the same normalizations given in (4.2.7)–(4.2.9).

Equations (4.2.10) and (4.2.11) will provide the foundation for the following discussion of noise reduction. In these equations, the role of α is seen more clearly as providing the coupling of amplitude fluctuations into instantaneous frequency fluctuations. It should be emphasized that this is a one-way coupling, from ρ to $\dot{\varphi}$. The amplitude fluctuation spectrum is not affected by the α parameter.

One consequence of a nonzero α, however, is enhancement of the fundamental linewidth over its Schawlow-Townes value. Using the low-frequency limit of (4.2.11), one finds that the power spectrum of the field is a Lorentzian with a linewidth [7]

$$\Delta\omega = \Delta\omega_{ST}(1+\alpha^2) \tag{4.2.12}$$

where

$$\Delta\omega_{ST} = \frac{S}{2P} \tag{4.2.13}$$

is the modified Schawlow-Townes linewidth. In the ideal case, linewidth is inversely proportional to laser power. However, at high power, it is often observed that the linewidth reaches a constant value and thereafter remains independent of power. To account for this extra component of linewidth, a power-independent term will be added to (4.2.12), so that

$$\Delta\omega = \Delta\omega_{ST}(1+\alpha^2) + \Delta\omega_o. \tag{4.2.14}$$

The origin of this extraneous linewidth is not known, but several potential mechanisms have been discussed in the literature. These include carrier number fluctuations [13], thermal fluctuations [14], and spatial hole burning [15]. In any case, the existence of a power-independent source of linewidth can be incorporated into the instantaneous frequency fluctuation spectrum by adding a phenomenological noise source $\tilde{\Delta}_o$, such that $\Delta\omega_o$ is the spectral density of $\tilde{\Delta}_o$. Equation (4.2.11) then becomes

$$\dot{\varphi}(\Omega) = \tilde{\Delta}_I + \frac{\alpha\omega_R^2}{(\omega_R^2 - \Omega^2) + \dfrac{i\Omega}{\tau_R}}\tilde{\Delta}_R + \tilde{\Delta}_o. \tag{4.2.15}$$

It is assumed that $\tilde{\Delta}_o$ is uncorrelated with the other Langevin sources arising from

spontaneous emission. The presence of this term will later illustrate how an independent source of linewidth influences our ability to reduce intensity noise.

For a directly detected field, the relative intensity noise (RIN) is defined as the ratio of the mean square power per unit bandwidth of the fluctuating photocurrent to the average photocurrent power. By this definition, the RIN spectrum is directly proportional to the spectral density of the amplitude fluctuations, given by

$$W_{\rho\rho}(\Omega) = \langle \rho^*(\Omega)\rho(\Omega)\rangle = \frac{\frac{1}{\tau_R^2} + \Omega^2}{(\omega_R^2 - \Omega^2)^2 + \frac{\Omega^2}{\tau_R^2}} \quad \Delta\omega_{ST}. \tag{4.2.16}$$

Since the proportionality constant is of no consequence when direct comparisons of RIN are made, hereafter we will define relative intensity noise as

$$\text{RIN} \equiv W_{\rho\rho}(\Omega). \tag{4.2.17}$$

The way in which the RIN varies as a function of laser power can be divided into two regimes. For the moment, consider fluctuation frequencies $\Omega \ll 1/\tau_R, \omega_R$, so that the intensity noise has a flat spectrum given by

$$\text{RIN} = \frac{S}{2P\tau_R^2\omega_R^4}. \tag{4.2.18}$$

At low power, τ_R is essentially power-independent while ω_R^2 is always linearly proportional to P. This characterizes the excess noise regime, where the RIN falls as $1/P^3$. In the high-power limit, $\tau_R\omega_R^2$ saturates to a constant value, so the RIN falls as $1/P$, which is defined as the shot noise regime. In practice, both regimes may be observed by directly detecting the intensity noise with a photodiode followed by a high-gain amplifier (see chapter 5). However, in this chapter we assume that the

laser is operating in the excess noise regime. The fluctuations are then dominated by spontaneous emission, and the noise level is sufficiently far above the level of photon shot noise (or vacuum noise) that a semiclassical treatment of the laser noise and noise reduction is appropriate.

4.3 Intensity noise reduction with a passive, external transmission function

In this section we discuss a scheme to reduce semiconductor laser intensity noise which exploits the fundamental amplitude/phase coupling in the field fluctuations [5], [6]. The technique relies on the observation that although the intensity noise level is independent of α, the enhanced instantaneous frequency fluctuations measured by α contain an image of the intensity noise. It is this image resulting from the correlation between $\rho(\Omega)$ and $\dot{\varphi}(\Omega)$ which can be recovered to reduce the intensity noise below its intrinsic level. In what follows, we show that an external, passive element with a frequency dependent transmission (see Fig. 4.1) can accomplish this task by transforming the field in the desired way. We emphasize that no feedback to the laser source is involved in this scheme. The fluctuating field is passively processed after leaving the laser cavity. For an ideal laser source with no extraneous component of linewidth, the intensity noise can potentially be reduced by the amount $1/(1+\alpha^2)$, the inverse of the linewidth broadening term. This reduction is independent of laser power, and is achieved by altering the correlation between the fluctuations. We quantify the effect of the transmission function on the field's correlation properties by calculating

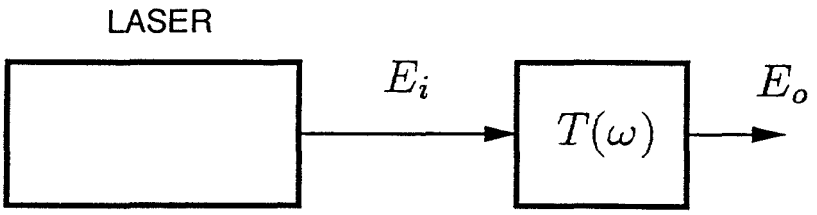

Figure 4.1: Free-running laser and passive, external transmission function $T(\omega)$. The intrinsic intensity noise in the input light can be reduced when $T(\omega)$ has the right slope.

the cross-spectral density of the fluctuations. For the ideal laser mentioned above, maximum intensity noise reduction coincides with decorrelation of amplitude and instantaneous frequency fluctuations. Even in the case of a laser with an extraneous linewidth component, large reduction in intensity noise exceeding an order of magnitude is possible. The dependence of noise reduction on output power will then be discussed.

4.3.1 Transformation of field fluctuations

Before analyzing the noise reduction method quantitatively, we can form an intuitive picture of how a frequency dependent transmission function affects the field fluctuations. Suppose that the radiation goes through such a function $T(\omega)$, as shown in Fig. 4.2. The fluctuations in instantaneous frequency may be viewed as the lasing

frequency jittering about the lasing linecenter ω_L. Assuming that $T(\omega)$ has nonzero slope in the vicinity of ω_L, the frequency jitter is converted into jitter in the transmitted amplitude. Since these new amplitude fluctuations are correlated with the existing amplitude fluctuations in the field, they can be made to cancel each other when they are superposed. Thus, the intensity noise can potentially be reduced by choosing a transmission function with a proper slope.

It is straightforward to evaluate the effect of the transmission function on the fluctuations [6]. Assume that $T(\omega)$ is slowly-varying over the range of fluctuation frequencies we are interested in. It will be seen that this is an excellent assumption when $T(\omega)$ is realized by a Michelson interferometer. A Taylor expansion of $T(\omega)$ about the lasing linecenter becomes possible, yielding

$$T(\omega_L + \Omega) \approx T(\omega_L) + \Omega T'(\omega_L) \tag{4.3.1}$$

where T' is the derivative of the transmission with respect to frequency. Let the slowly-varying complex amplitude of the input field be defined as

$$A_i(t) = (1 + \rho_i(t))e^{i\varphi_i(t)} \tag{4.3.2}$$

so that $E(t) \equiv A(t)\sqrt{p_o}\exp(i\omega_L t)$ (see (4.2.2)). In terms of a Fourier component of the input and output fields, (4.3.1) gives

$$\begin{aligned} \tilde{A}_o(\Omega) &= T(\omega_L + \Omega)\tilde{A}_i(\Omega) \\ &= T(\omega_L)\tilde{A}_i(\Omega) + \Omega T'(\omega_L)\tilde{A}_i(\Omega). \end{aligned} \tag{4.3.3}$$

By inspection, (4.3.3) is the Fourier transform of the equation

$$A_o(t) = T(\omega_L)A_i(t) - iT'(\omega_L)\dot{A}_i(t) \tag{4.3.4}$$

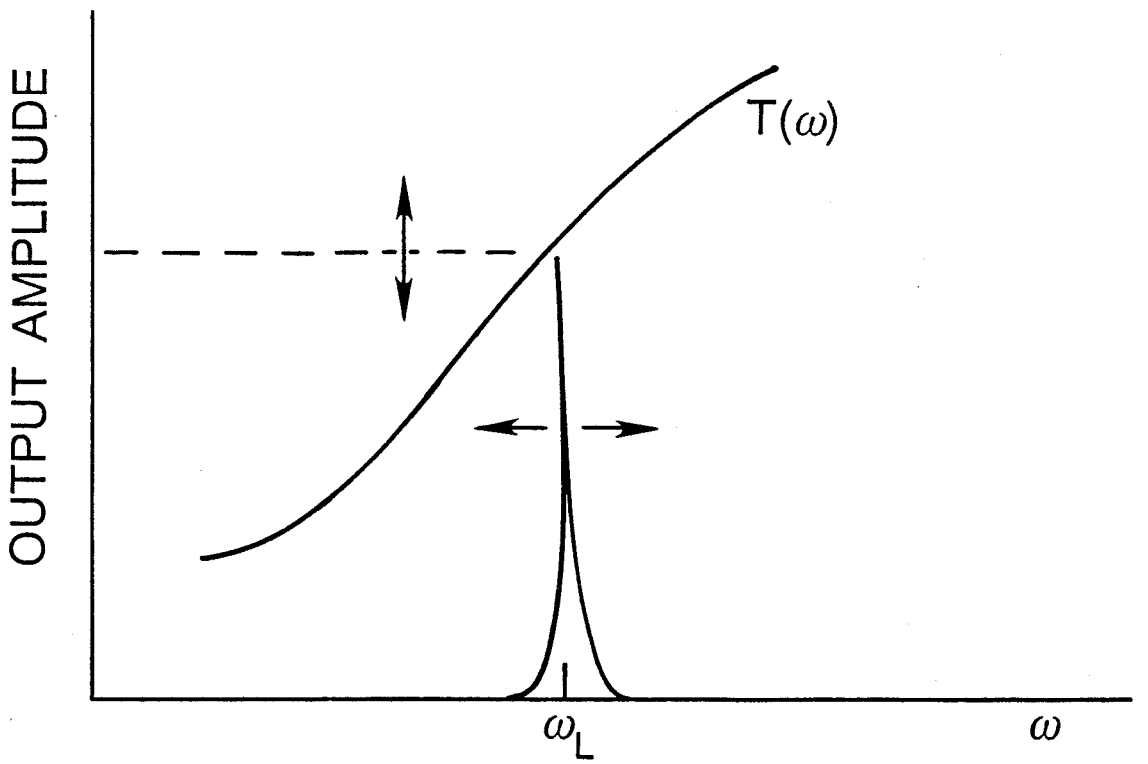

Figure 4.2: The transmission function, $T(\omega)$, converts instantaneous frequency noise in the input field to amplitude noise. $T(\omega)$ is acting as a frequency discriminator.

which can be used to derive the effect of $T(\omega)$ on the amplitude fluctuation of the output field, with the result,

$$\rho_o(t) = T_R\rho_i(t) + T'_R(\dot{\varphi}_i(t) - i\dot{\rho}_i(t)). \tag{4.3.5}$$

where the subscript R denotes the the real part of T. Similarly, the derivative with respect to time of (4.3.4) in conjunction with (4.3.5) gives

$$\dot{\varphi}_o(t) = \dot{\varphi}_i(t). \tag{4.3.6}$$

Products of small-signal quantities have been neglected in writing the above relations. Transforming back to the frequency domain, we find

$$\rho_o(\Omega) = (T_R + \Omega T'_R)\rho_i(\Omega) + T'_R\dot{\varphi}_i(\Omega) \tag{4.3.7}$$

$$\dot{\varphi}_o(\Omega) = \dot{\varphi}_i(\Omega). \tag{4.3.8}$$

Equation (4.3.7) shows that $\rho_o(\Omega)$ is the sum of two parts depending on both the amplitude fluctuation and instantaneous frequency fluctuation of the input field. The inherent correlation between ρ_i and $\dot{\varphi}_i$ will enable intensity noise reduction in the output field by controlling T_R and T'_R. The instantaneous frequency fluctuation of the output field, on the other hand, is not affected by the transmission function, as (4.3.8) shows. Consequently, it often will not be necessary to make a distinction between $\dot{\varphi}_i$ and $\dot{\varphi}_o$.

To account for the fact that $T(\omega)$ attenuates the mean field in addition to transforming the fluctuations, we normalize $\rho_o(\Omega)$ by T_R and so obtain

$$\rho_o(\Omega) = (1 + \Omega\xi)\rho_i(\Omega) + \xi\dot{\varphi}_i(\Omega) \tag{4.3.9}$$

where $\xi \equiv T_R'/T_R$ and will hereafter be referred to as the "slope" of T. By making this definition, the RIN spectra of the input and output are simply

$$\text{RIN}_i = W_{\rho_i\rho_i}(\Omega) \tag{4.3.10}$$

$$\text{RIN}_o = W_{\rho_o\rho_o}(\Omega) \tag{4.3.11}$$

and we see that $\text{RIN}_o \rightarrow \text{RIN}_i$ as $\xi \rightarrow 0$, that is, in the limit of zero transmission function slope.

In reality, the factor $\Omega\xi$ appearing in the transformation equation (4.3.9) is usually much smaller than unity and can be neglected for the range of frequencies and slopes that will be encountered. In particular, the results of section 4.5 show that to achieve noise reduction, ξ will typically be 0.03 GHz^{-1} or less, so $\Omega\xi \ll 1$ for all frequencies of interest. With this observation, (4.3.9) becomes

$$\rho_o(\Omega) = \rho_i(\Omega) + \xi\dot{\varphi}_i(\Omega) \tag{4.3.12}$$

which is the final transformation equation.

4.3.2 Spectral density of transformed fluctuations

If we assume for now that we have an ideal laser source, that is, one without an extraneous linewidth component, then the spectral density of the output amplitude fluctuation may be computed using (4.2.10), (4.2.11), and (4.3.12).

$$W_{\rho_o\rho_o}(\Omega,\xi) = \text{RIN}_o = \left[\xi^2 + \frac{(1/\tau_R + \alpha\xi\omega_R^2)^2 + \Omega^2}{(\omega_R^2 - \Omega^2)^2 + \frac{\Omega^2}{\tau_R^2}}\right]\Delta\omega_{ST} \tag{4.3.13}$$

This expression simplifies if we restrict our attention to frequencies $\Omega \ll 1/\tau_R, \omega_R$, where the RIN spectrum is flat. In this case

$$\mathrm{RIN}_o = \left[\xi^2 + \frac{(1/\tau_R + \alpha\xi\omega_R^2)^2}{\omega_R^4}\right] \Delta\omega_{ST} \tag{4.3.14}$$

and using

$$\mathrm{RIN}_i = \frac{\Delta\omega_{ST}}{\tau_R^2\omega_R^4} \tag{4.3.15}$$

the RIN of the input and output fields may be easily related.

$$\mathrm{RIN}_o = [(\tau_R\omega_R^2\xi)^2 + (1 + \alpha\tau_R\omega_R^2\xi)^2]\mathrm{RIN}_i \tag{4.3.16}$$

By minimizing this function with respect to ξ, the optimum slope is found to be

$$\xi_{opt} = \frac{-1}{\tau_R\omega_R^2}\frac{\alpha}{1+\alpha^2} \tag{4.3.17}$$

which gives the maximum noise reduction

$$\mathrm{RIN}_o = \frac{1}{1+\alpha^2}\mathrm{RIN}_i. \tag{4.3.18}$$

For a typical α = -5, the intensity noise floor can thus be reduced below its intrinsic level by a factor of 26. This lower limit on noise reduction is governed by the factor $(1+\alpha^2)$, the same factor which enhances the fundamental linewidth of the laser over its Schawlow-Townes value. As the slope is changed from the optimum, different amounts of noise reduction (or enhancement) will occur in accordance with (4.3.16). This is shown in Fig. 4.3 where the output noise is seen to vary quadratically with slope about the minimum. According to (4.3.17), the optimum slope is a function of $\tau_R\omega_R^2$ and generally will vary with the laser power level. Even so, the maximum reduction (4.3.18) remains independent of laser power.

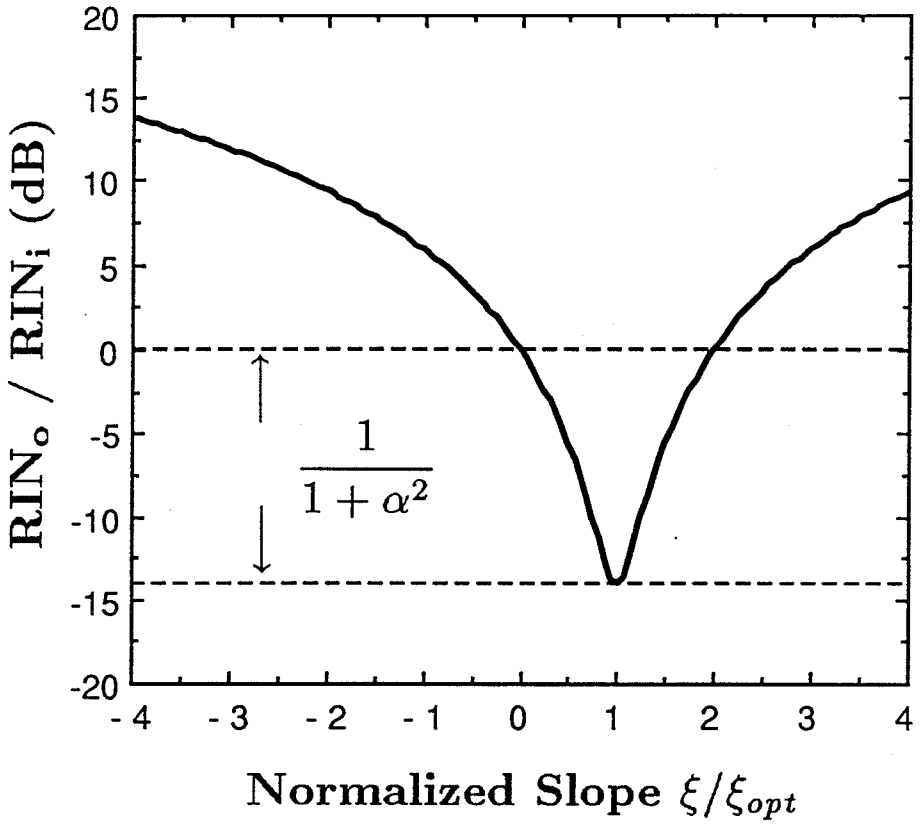

Figure 4.3: Relative level of output intensity noise vs. normalized slope. For the optimum slope (4.3.17), noise is reduced below its intrinsic level by $1/(1+\alpha^2)$, where α = -5 is assumed. This figure characterizes noise reduction in the flat part of the intensity noise spectrum.

The complete RIN spectrum of the output field is given by (4.3.13). For a given value of ξ, the amount of noise reduction is a function of frequency. Figure 4.4 shows the RIN spectrum calculated from (4.3.13) for several values of transmission slope. Typical values for τ_R (2.6×10^{-10} sec rad^{-1}) and ω_R (9.4×10^9 rad sec^{-1}) characteristic of a DFB laser at low bias are taken from the literature [16]. An α of -5 is also used. The heavy curve is the intrinsic intensity noise level of the input field, corresponding to $\xi = 0$. When ξ is at the optimum value given by (4.3.17), the low-frequency noise is reduced by $1/(1+\alpha^2)$ in accordance with (4.3.18), but the amount of reduction diminishes at higher frequencies. If the slope is too large, $3\xi_{opt}$ for this example, then the low-frequency noise is enhanced over its intrinsic value, in agreement with (4.3.16) and Fig. 4.3. For the range of slopes in Fig. 4.4, the noise level at the resonance is not significantly affected. We also see that the high-frequency noise beyond the resonance is enhanced even when the low-frequency noise is reduced. This is not surprising because at high frequencies the phase noise is dominated by its independent component ($\tilde{\Delta}_I$ term in (4.2.11)) which is being converted by $T(\omega)$ to an additive component of intensity noise.

The optimum slope which minimizes the output intensity noise at frequency Ω is

$$\xi_{opt}(\Omega) = \frac{-1}{\tau_R \omega_R^2} \frac{\alpha D(\Omega)}{1+\alpha^2 D(\Omega)} \tag{4.3.19}$$

where

$$D(\Omega) = \frac{\omega_R^4}{(\omega_R^2 - \Omega^2)^2 + \dfrac{\Omega^2}{\tau_R^2}}. \tag{4.3.20}$$

The variation in optimum slope is shown in Fig. 4.5, where $\xi_{opt}(\Omega)$ is plotted normalized by the optimum low-frequency slope ξ_{opt} from (4.3.17). Noise reduction at higher

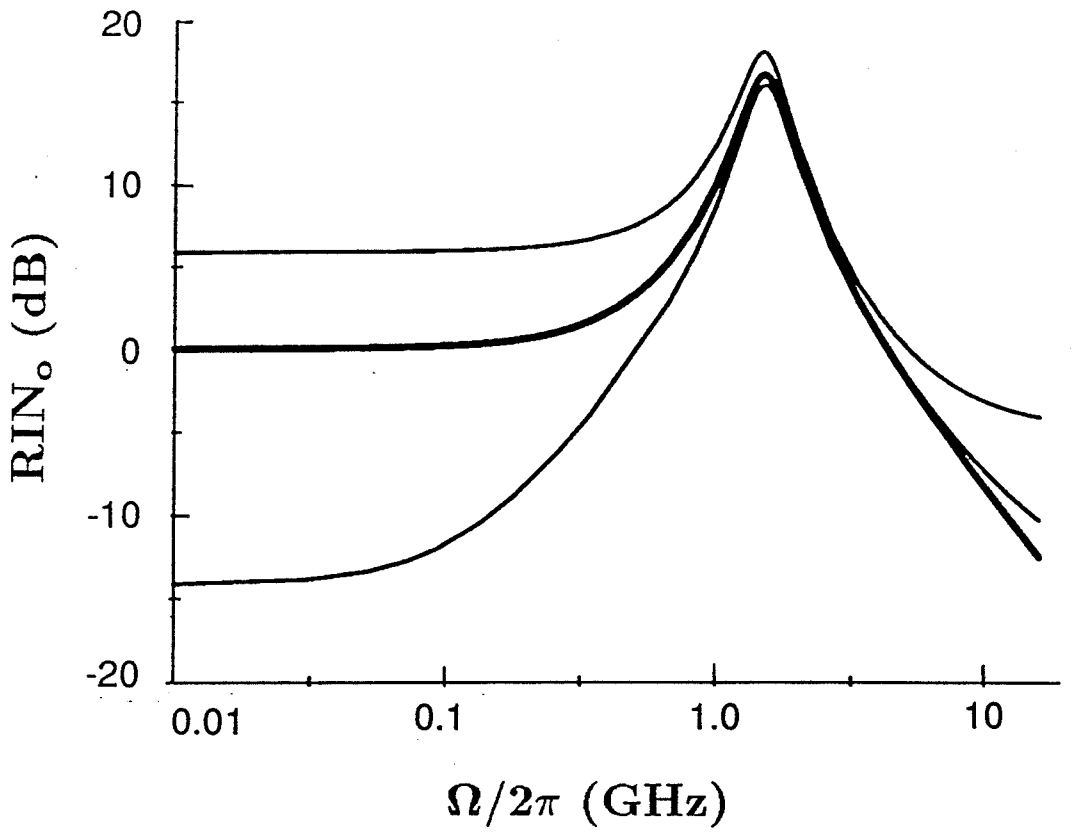

Figure 4.4: Output intensity noise spectrum for different slopes calculated from (4.3.13). The heavy curve is the intrinsic noise level ($\xi = 0$). Spectra are measured relative to the intrinsic noise level at low frequency. Noise is reduced in the flat region by $1/(1+\alpha^2)$ when $\xi = \xi_{opt}$, or enhanced ($\xi = 3\xi_{opt}$) as the slope is varied. High-frequency noise is enhanced for all slopes.

frequencies therefore requires a fairly constant slope as Ω approaches ω_R. Beyond the resonance the optimum slope tends to zero, which indicates that noise reduction is becoming impossible at these high frequencies.

A plot of the spectrum of maximum possible noise reduction also appears in Fig. 4.5. This function is obtained by evaluating RIN_o (4.3.13) at the optimum slope for each frequency (4.3.19), and is the envelope of minimum noise levels in the progression of noise spectra in Fig. 4.4, normalized by the intrinsic noise spectrum, i.e.,

$$\text{maximum noise reduction spectrum} = \frac{W_{\rho_o\rho_o}(\Omega, \xi_{opt}(\Omega))}{W_{\rho_i\rho_i}(\Omega)}. \tag{4.3.21}$$

The left-hand side of Fig. 4.5 shows that the noise can be reduced by $1/(1+\alpha^2)$ at low frequency, the magnitude of reduction decreases as the resonance frequency is approached, and no reduction is possible at frequencies beyond the resonance.

4.3.3 Correlation properties

To further illustrate the effect of the transmission function $T(\omega)$ on the field fluctuations, it is useful to compute the symmetric cross-spectral density of ρ and $\dot{\varphi}$, defined as

$$W_{\rho\dot{\varphi}}(\Omega) = \frac{1}{2}\left[\langle\rho(\Omega)\dot{\varphi}^*(\Omega)\rangle + \langle\rho^*(\Omega)\dot{\varphi}(\Omega)\rangle\right]. \tag{4.3.22}$$

Using (4.3.22), (4.2.10), and (4.2.11), the cross-spectral density of the input field is

$$W_{\rho_i\dot{\varphi}}(\Omega) = \frac{\dfrac{\alpha\omega_R^2}{\tau_R}}{(\omega_R^2 - \Omega^2)^2 + \dfrac{\Omega^2}{\tau_R^2}}\Delta\omega_{ST}. \tag{4.3.23}$$

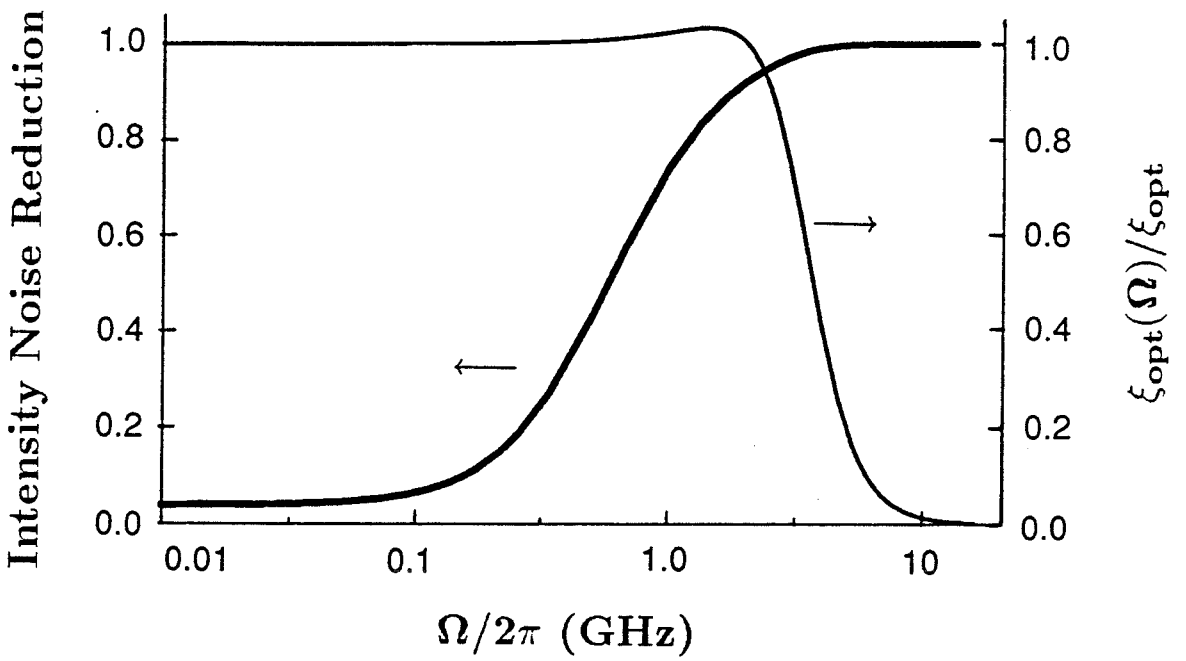

Figure 4.5: Left-hand side: Maximum intensity noise reduction as a function of frequency. Noise is reduced by $1/(1+\alpha^2)$ where the noise spectrum is flat. Beyond the resonance, noise cannot be reduced below the intrinsic level.

Right-hand side: Normalized optimum slope to achieve intensity noise reduction vs. frequency. $\xi_{opt}(\Omega)$ tends to zero at high frequency where noise reduction is not possible.

This function gives the degree of correlation between the Fourier components of the field's intrinsic amplitude and instantaneous frequency fluctuations. For the input field, a logarithmic plot of the magnitude of (4.3.23) in Fig. 4.6 shows that there is always correlation except in the high-frequency limit, which fits with the intuitive model of [7]. Since the fluctuations are coupled through perturbations to the carrier density, there can't be any significant correlation at timescales much shorter than the characteristic response time τ_R. As expected, the above function is directly proportional to α. To be precise, the fact that α is negative means that ρ_i and $\dot{\varphi}$ are anticorrelated.

After passing through the transmission function, the amplitude fluctuation is transformed according to (4.3.12), and the cross-spectral density of the output field becomes

$$W_{\rho_o\dot{\varphi}}(\Omega,\xi) = \left[\xi + \frac{\alpha^2\omega_R^4\xi + \dfrac{\alpha\omega_R^2}{\tau_R}}{(\omega_R^2-\Omega^2)^2 + \dfrac{\Omega^2}{\tau_R^2}}\right]\Delta\omega_{ST}. \tag{4.3.24}$$

The correlation is now a function of ξ, the transmission function slope. Figure 4.6 also shows the magnitude of this function evaluated at the optimum value of ξ used to generate the normalized noise reduction spectrum in Fig. 4.4. By comparing these two figures we see that noise reduction coincides with reduced correlation in the fluctuations. In fact, when the noise is maximally reduced at low frequency, the cross-spectral density approaches zero, indicating that the low-frequency fluctuations have been decorrelated by the transmission function. (Note: It is useful to take the log of the magnitude of (4.3.24), as in Fig. 4.6, because the large dynamic range at low frequencies is clearly seen, but an artifact of this is a sharp feature after the

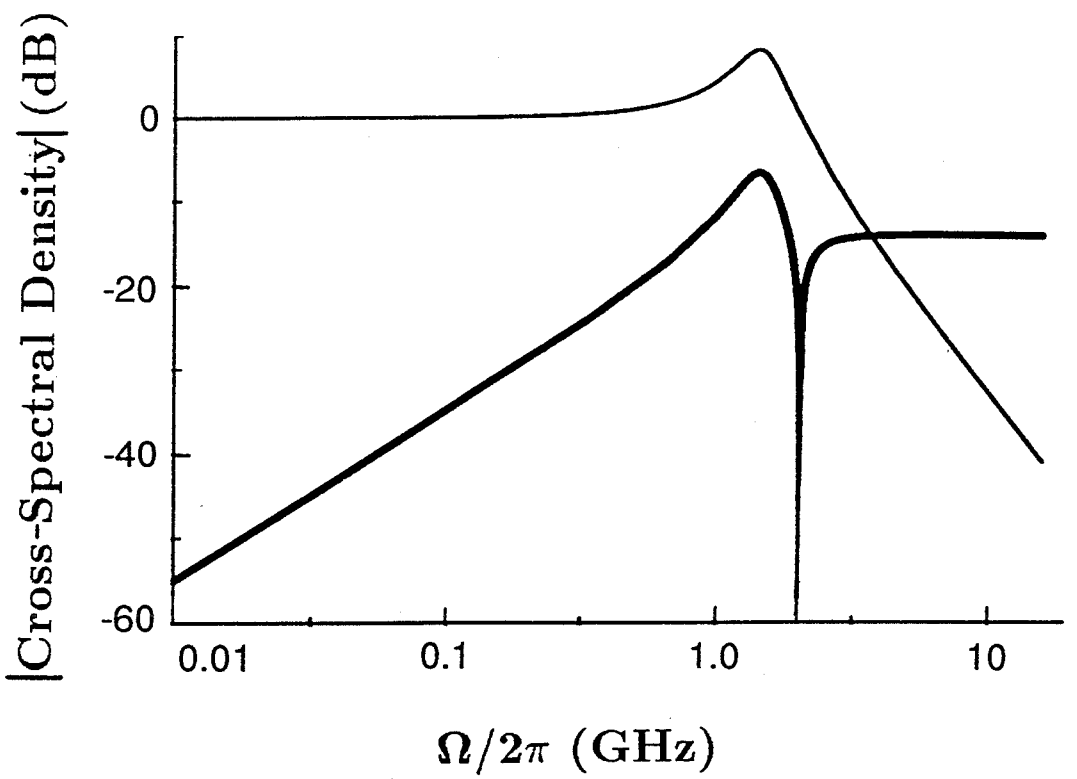

Figure 4.6: Magnitude of the cross-spectral density of $\rho(\Omega)$ and $\dot{\varphi}(\Omega)$ of the input field (normalized by the low-frequency value), and of the output field (heavy curve) for $\xi = \xi_{opt}$, showing decorrelation of the fluctuations at low frequency. The function changes sign after the resonance, appearing as a sharp feature in this logarithmic plot.

resonance where the function changes sign). In addition, a new correlation at high frequency arises from the independent source of phase noise ($\tilde{\Delta}_I$ term in (4.2.11)) which is being converted to additive intensity noise by the transmission function.

The fact that the cross-spectral density is driven to zero at low frequencies when $\xi = \xi_{opt}$ can be understood by considering the fluctuations in the time domain. In the low-frequency limit, we have from (4.2.4) - (4.2.6)

$$\hat{\rho}(t) = \Delta_R \tag{4.3.25}$$

$$\dot{\varphi}(t) = \Delta_I + \alpha\Delta_R \tag{4.3.26}$$

where $\hat{\rho}(t) = \tau_R\omega_R^2\rho(t)$ is a rescaled amplitude fluctuation in order that $\hat{\rho}(t)$ and $\dot{\varphi}(t)$ be dimensionally equivalent. Let $\sigma^2 = \langle\Delta_R^2\rangle = \langle\Delta_I^2\rangle$ be the variance of the Langevin terms (directly proportional to the integration bandwidth, since the Langevin forces have a flat spectral density) so that

$$\langle\hat{\rho}_i(t)^2\rangle = \sigma^2 \tag{4.3.27}$$

$$\langle\dot{\varphi}_i(t)^2\rangle = \sigma^2(1+\alpha^2) \tag{4.3.28}$$

are the variances of the input field variables $\hat{\rho}_i(t)$ and $\dot{\varphi}_i(t)$.

If the laser were operating in the tuned condition, corresponding to $\alpha = 0$, then contours of constant probability density would be circular, as shown in Fig. 4.7. For the detuned case, the contours are ellipses tilted with respect to the coordinate axes. As a result of detuning, the variance of the instantaneous frequency fluctuation is enhanced by $1+\alpha^2$ but the variance of the amplitude fluctuation is unchanged. This tilted ellipse represents the state of the fluctuating input field, where the degree of

tilt, and corresponding thinness of the ellipse, indicates the correlation between the fluctuations.

Using (4.3.12),(4.3.25) and (4.3.26), when $\xi = \xi_{opt}$, the output field variables are

$$\hat{\rho}_o(t) = \frac{\Delta_R}{1+\alpha^2} - \frac{\alpha\Delta_I}{1+\alpha^2} \tag{4.3.29}$$

$$\dot{\varphi}_o(t) = \Delta_I + \alpha\Delta_R \tag{4.3.30}$$

which are clearly uncorrelated. The variances are given by

$$\langle\hat{\rho}_o(t)^2\rangle = \frac{\sigma^2}{1+\alpha^2} \tag{4.3.31}$$

$$\langle\dot{\varphi}_o(t)^2\rangle = \sigma^2(1+\alpha^2). \tag{4.3.32}$$

The output field ellipse is also shown in Fig. 4.7. For the optimum slope, we see that the transmission function has rotated the ellipse to align it with the coordinate axes. As a result of the rotation, the output field variables $\hat{\rho}_o(t)$ and $\dot{\varphi}_o(t)$ are decorrelated while the variance of the amplitude fluctuation is simultaneously reduced by the factor $1/(1+\alpha^2)$. Decorrelation of the fluctuations by $T(\omega)$ therefore coincides with intensity noise reduction.

4.3.4 Effect of a power-independent linewidth

To complete this discussion, we must consider the effect of an extra, non-Schawlow-Townes, component of linewidth on the RIN of the output field. We can foresee that, in general, the amount of noise reduction will diminish, since the extraneous linewidth is presumed to come from a phase noise source ($\tilde{\Delta}_o$ term in (4.2.15)) which is not correlated with the other noise sources. It is straightforward to substitute

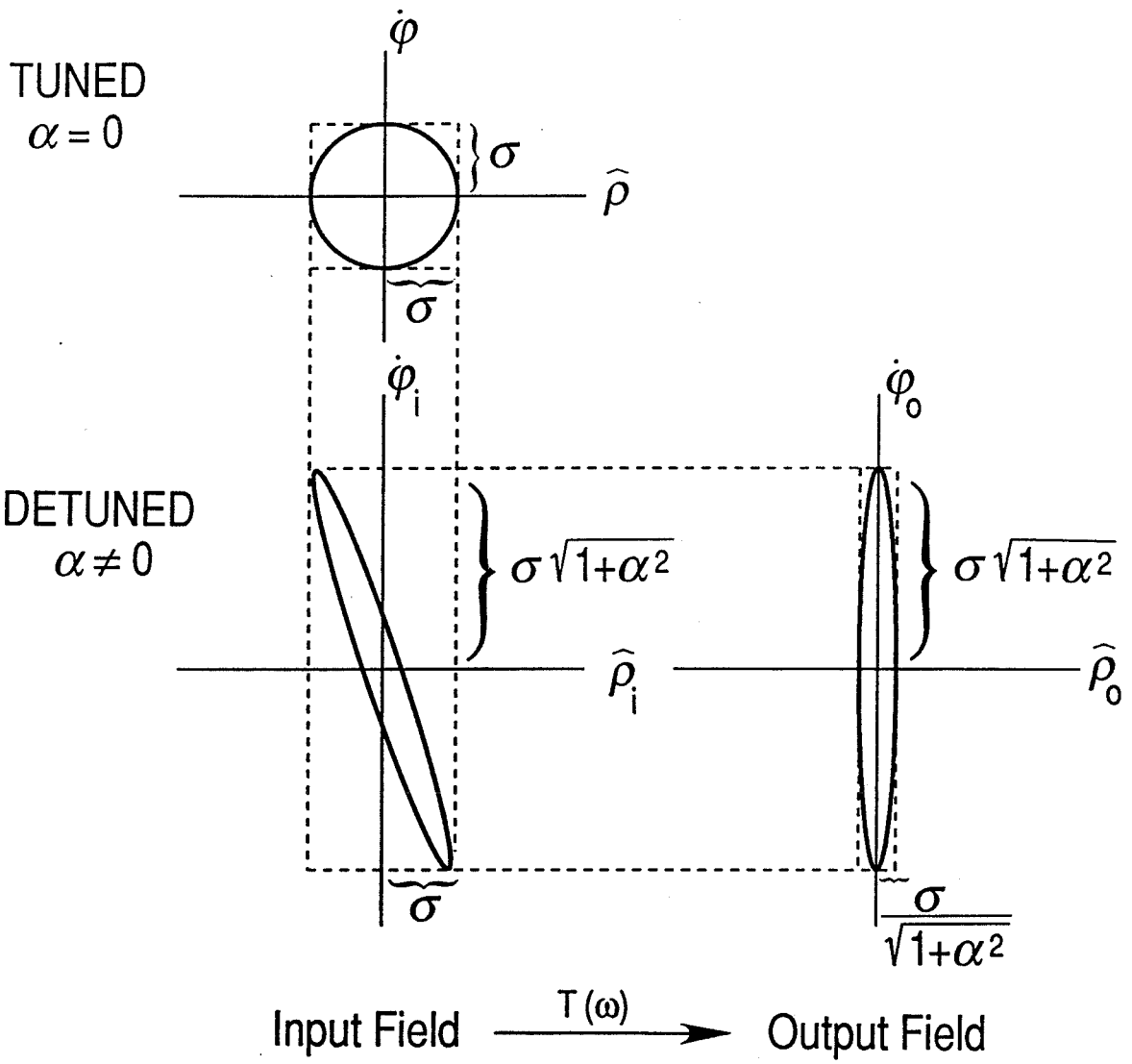

Figure 4.7: Contours of constant probability density for tuned ($\alpha = 0$) and detuned ($\alpha \neq 0$) operation. For the detuned case, the tilted ellipse of the input field is rotated by $T(\omega)$ to decorrelate the variables and reduce the variance of $\hat{\rho}_o(t)$ by $1/(1+\alpha^2)$.

this augmented instantaneous frequency fluctuation spectrum into the transformation equation (4.3.12) to compute the output RIN. In the low-frequency limit, we find analagous to (4.3.16)

$$\mathrm{RIN}_o = [(\tau_R\omega_R^2\xi)^2(1+\beta) + (1+\alpha\tau_R\omega_R^2\xi)^2]\mathrm{RIN}_i \tag{4.3.33}$$

where $\beta \equiv \Delta\omega_o/\Delta\omega_{ST}$ is the ratio of the power-independent linewidth to the Schawlow-Townes linewidth. β increases linearly with laser power, since $\Delta\omega_{ST}$ has inverse power dependence. Evaluating the above relation at the slope which minimizes the output intensity noise,

$$\xi_{opt} = \frac{-1}{\tau_R\omega_R^2}\frac{\alpha}{1+\alpha^2+\beta}, \tag{4.3.34}$$

the maximum reduction is now given by

$$\mathrm{RIN}_o = \frac{1+\beta}{1+\alpha^2+\beta}\mathrm{RIN}_i. \tag{4.3.35}$$

Thus, for nonzero β, the ability to reduce intensity noise is diminished compared to the ideal case (4.3.18). Furthermore, the amount of reduction is now a function of laser power, the net reduction becoming smaller as output power increases. This behavior will be shown to agree with measurements on a DFB laser diode in section 4.5.

For the complete output spectrum it can be easily seen that the presence of the extra linewidth component will add a uniform offset to the noise level by the amount $\xi^2\beta\Delta\omega_{ST}$ (see (4.3.13)). Thus the magnitude of reduction at any frequency will decrease as the laser is run at higher bias.

To summarize the results of this section, we have studied the effects of an external, passive transmission function on the intensity noise of the laser field and found that

large reductions below the intrinsic level are possible when the transmission function has the correct slope. The method works by exploiting the inherent correlation between the field fluctuations. Optimum intensity noise reduction simultaneously decorrelates the amplitude and phase fluctuations at the output.

4.4 Intensity noise reduction with a dispersive, intracavity loss element

A dispersive transmission function external to the laser cavity may reduce intensity noise, as was just shown. The same is true if the element is placed inside the cavity, where it then constitutes a dispersive loss. Contrary to the external case where the element acts on the field but does not affect the laser, the internal loss element influences the laser dynamics, and must be incorporated into the rate equations. The underlying mechanism for intensity noise reduction is similar in both cases, however, and the maximum amount of reduction is again given by the factor $1/(1+\alpha^2)$.

This method for noise reduction will only be discussed briefly, because the effects of such an intracavity dispersive loss have been studied in work on "detuned loading" in semiconductor lasers [17], [18]. In fact, it was shown experimentally that phase noise (linewidth) reduction and modulation speed enhancement could be achieved simultaneously through such an approach [19]. The application to intensity noise reduction was not pursued in the literature. Here, our intent is to quantify how well the intensity noise is reduced when the loss element has the right slope. Intuitively, this mechanism for noise reduction relies on amplitude/phase correlation, but contrary

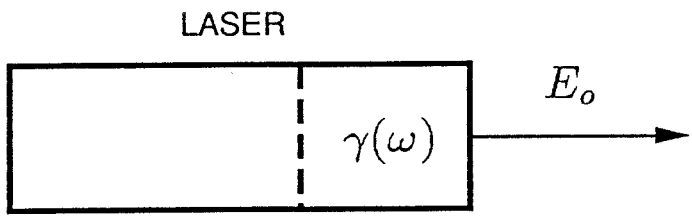

Figure 4.8: Laser with frequency-dependent intracavity loss $\gamma(\omega)$. The intrinsic intensity noise can be reduced when $\gamma(\omega)$ has the right slope.

to the passive case there is a feedback mechanism through the optical gain. In other words, the enhanced phase noise (frequency jitter), which contains an image of the intensity noise, causes jitter in the instantaneous cavity loss owing to the dispersive loss function. The gain dynamically adjusts to compensate the fluctuating loss and so quiets the intensity noise, assuming the loss function has the right slope. As mentioned above, there may reduction in the phase noise as well, but we will focus on the intensity noise here.

The dispersive intracavity loss $\gamma(\omega)$ is shown schematically in Fig. 4.8. The equation of motion for the slowly varying field amplitude (4.3.2) is given by [18]

$$\dot{A} = \frac{1}{2}(G - \gamma(\omega))(1 - i\alpha)A + \Delta \tag{4.4.1}$$

where $\Delta = \Delta_R + i\Delta_I$ is the Langevin noise source. A linear expansion of γ about the

lasing frequency is assumed possible, so that

$$\gamma(\omega) = \gamma(\omega_L) + 2\xi\delta\omega \tag{4.4.2}$$

where ξ is the slope of γ and $\delta\omega$ is the complex instantaneous frequency deviation, given by

$$\delta\omega = -i\frac{\dot{A}}{A}. \tag{4.4.3}$$

The small-signal equation of motion then results

$$\dot{A} = \frac{G'n(t)}{2}\frac{(1-i\alpha)A}{1-i\xi} + \frac{\Delta}{1-i\xi} \tag{4.4.4}$$

where G' is the differential gain and $n(t)$ is the carrier density deviation. Substituting the expression (4.3.2) for A in terms of ρ and φ, we find

$$\dot{\rho} = \frac{G'n(t)}{2}\frac{1+\alpha\xi}{1+\xi^2} + \frac{\Delta_R - \xi\Delta_I}{1+\xi^2}. \tag{4.4.5}$$

At low frequencies where $n(t)$ and $\rho(t)$ track each other, this becomes (using 4.2.6)

$$\rho(t) = \frac{1}{\tau_R\omega_R^2}\frac{\Delta_R - \xi\Delta_I}{1+\alpha\xi} \tag{4.4.6}$$

where $\dot{\rho} \to 0$ in this low-frequency limit. The spectral density can then be found using the normalizations given in (4.2.7) - (4.2.9).

$$W_{\rho\rho} = \frac{1}{\tau_R^2\omega_R^4}\frac{1+\xi^2}{(1+\alpha\xi)^2}\Delta\omega_{ST} \tag{4.4.7}$$

Minimizing the above expression with respect to ξ gives $\xi_{opt} = \alpha$ for the optimum slope, so compared to the intrinsic RIN (spectral density when $\xi = 0$), the optimum RIN is

$$\mathrm{RIN}_{opt} = \frac{1}{1+\alpha^2}\mathrm{RIN}_{intrinsic} \tag{4.4.8}$$

which agrees with the theoretical minimum for the passive case (4.3.18). If the laser has an extraneous component of linewidth not due to spontaneous emission, then the remarks of section 4.3 would apply here as well, and the maximum reduction would be diminished.

In summary, we have shown that an intracavity dispersive loss can potentially achieve the same level of intensity noise reduction as the passive transmission function studied in section 4.3. In the flat part of the noise spectrum, both methods predict that reduction by the factor $1/(1+\alpha^2)$ is possible, assuming the laser does not possess a significant power-independent component of linewidth.

4.5 Experimental results

We have described two ways to reduce laser intensity noise below the intrinsic floor: an extra-cavity approach using a passive transmission element and an intra-cavity approach which incorporates a dispersive loss. In this section experimental results which verify the first approach are presented [4]–[6]. The transmission function is implemented with a Michelson interferometer. Intensity noise from a DFB laser shows significant reduction which requires only a small optical path difference in the Michelson. The level of noise reduction as a function of frequency, laser bias, and transmission function slope agree with the theoretical predictions.

We note that Michelson interferometers are often used to characterize phase noise in semiconductor lasers [20], [21]. In these experiments, however, the interferometer is said to be strongly unbalanced, where the path difference is on the order of 10 cm.

In our experiment the interferometer is only slightly unbalanced, as optimum path differences for noise reduction are on the order of millimeters.

A schematic diagram of the experimental setup appears in Fig. 4.9. The single-mode laser source used in this experiment is an InGaAsP distributed feedback laser made by Ortel Corporation operating at 1.3 μm. The threshold current is 21.8 mA. The light is collimated by an antireflection coated lens and sent through an optical isolator (Newport ISO-13H) with 60 dB isolation to prevent feedback effects. After passing through a Michelson interferometer with a maximum 87% intensity transmission, the output light is focused onto a high quantum efficiency (90%) *p-i-n* detector. The noise photocurrent is amplified by a low noise, high gain (52 dB) amplifier over the frequency band .01 - 1 GHz, and input to a microwave spectrum analyzer (HP 8558B). Lock-in detection is also employed to improve the sensitivity. With this arrangement, the intrinsic intensity noise from the DFB laser can be measured in both the excess and shot noise regimes, well above the thermal noise level of the detection system.

A linewidth versus power measurement was taken for the DFB laser which appears in Fig. 4.10. It shows that the linewidth varies inversely with power until it saturates at high power to a value of 7 MHz. This represents the power-independent linewidth component which will be shown to affect the magnitude of noise reduction that can be obtained.

The transmission function for a Michelson interferometer is given by

$$T(\omega) = \frac{1}{2} - \frac{m}{2} e^{\frac{i\omega\delta}{c}} \tag{4.5.1}$$

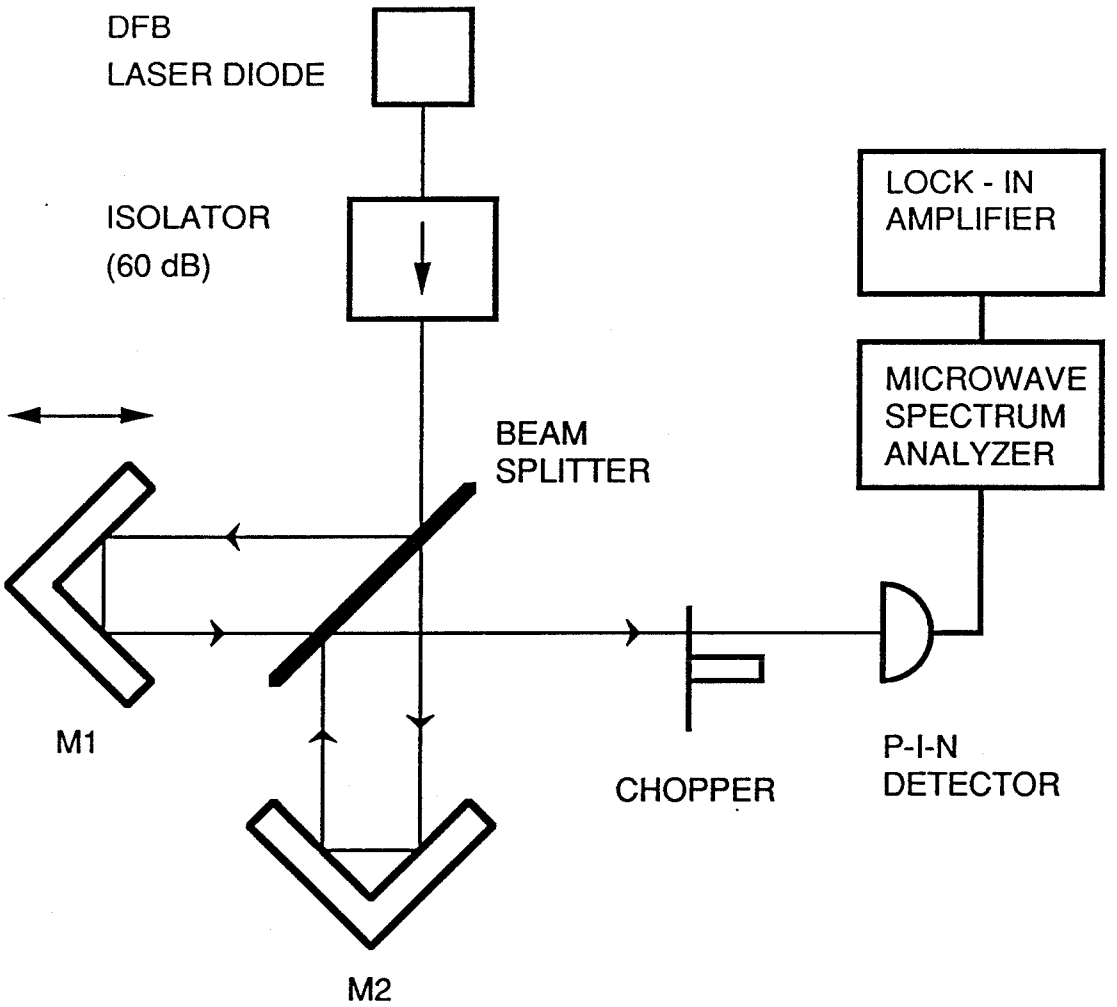

Figure 4.9: Schematic diagram of the experimental arrangement including a Michelson interferometer.

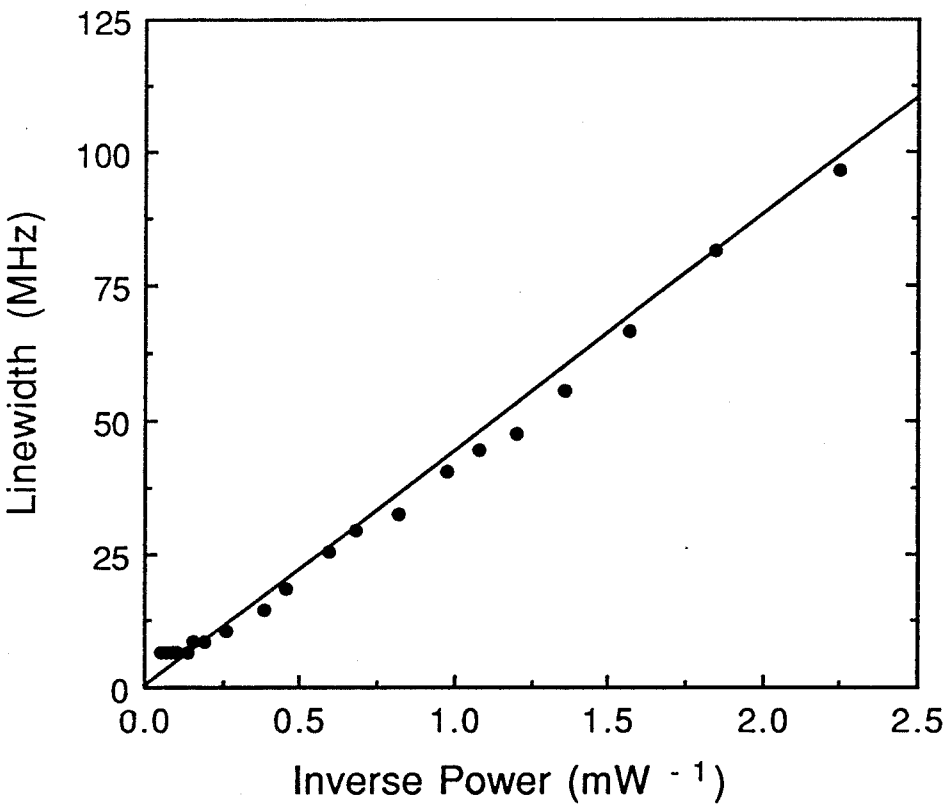

Figure 4.10: Measured linewidth vs. inverse power for the DFB laser used in the experiment. The high-power linewidth saturates at 7 MHz.

where δ is the optical path difference, c is the speed of light, and m (< 1), the amplitude visibility, accounts for the imperfect extinction of the interferometer. m is related to the intensity visibility v as follows

$$v \equiv \frac{|T|^2_{max} - |T|^2_{min}}{|T|^2_{max} + |T|^2_{min}} = \frac{2m}{m^2 + 1}. \tag{4.5.2}$$

The real part of the Michelson transmission function is given by

$$T_R(\omega) = \frac{1}{2}\left(1 - m\cos(\frac{\omega\delta}{c})\right) \tag{4.5.3}$$

and the derivative is

$$T'_R(\omega) = \frac{m\delta}{2c}\sin(\frac{\omega\delta}{c}). \tag{4.5.4}$$

One arm of the Michelson is controlled by both a micrometer for coarse positioning and a piezoelectric transducer (PZT) for submicron motion. The dependence of intensity noise on interferometer slope is characterized by setting the path difference using the micrometer, scanning the Michelson by one wavelength using the PZT, and measuring the noise power of the transmitted light at a given frequency and bandwidth. Figure 4.11 shows $T_R(\omega)$ in relation to the lasing frequency ω_L for two path differences δ_1 and δ_2 ($> \delta_1$). If the scan begins at maximum transmission, for instance, then during the scan the input field samples a transmission slope T'_R (4.5.4) which changes smoothly from 0 to $m\delta/2c$ to 0 to $-m\delta/2c$ to 0. In this way, a continuous range of slopes, both positive and negative, can be tested in one scan, and the extremes of this range are set by the amount of path difference, δ.

Figure 4.12 shows the results of an intensity noise measurement for a series of path differences at a laser bias of 23.3 mA. The output power is 0.34 mW and the

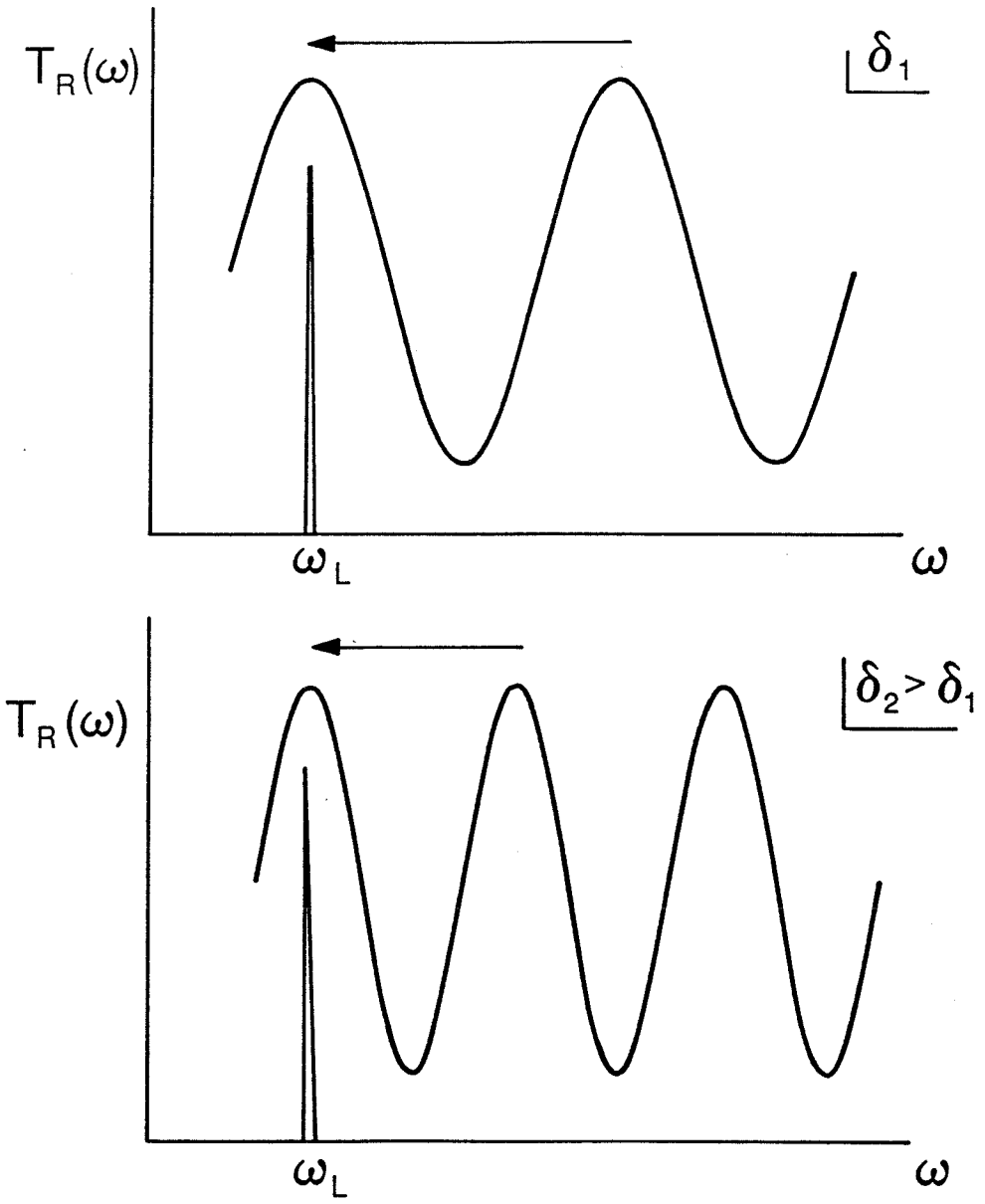

Figure 4.11: Measuring intensity noise as a function of interferometer slope. The Michelson is unbalanced by a path difference δ_1, so that the lasing field at ω_L encounters a range of positive and negative slopes as T_R is scanned by one fringe. For a larger delay δ_2, the fringes are pushed closer together, and the field encounters a wider range of slopes as T_R is scanned.

intrinsic RIN level is -130 dB/Hz. The noise was measured in a 100 kHz band at 130 MHz, within the flat region of the noise spectrum. Noise power is plotted as a function of transmitted intensity, proportional to the mean detector photocurrent. This is not the RIN, but the directly detected noise power which is related to RIN_o by multiplying the rhs of (4.3.33) by $|T|^4$. At zero path difference we see the intrinsic noise power level as the light is merely attenuated by the Michelson during the scan. If the Michelson is unbalanced, then the dependence of noise level on transmission slope becomes apparent. "Loops" of noise are observed whereby the noise is reduced below the intrinsic level for positive slopes and enhanced when the slope is negative. At the extremes of transmitted intensity for a given loop, the noise level returns to the intrinsic value as it should since this corresponds to zero slope. As the path difference increases, the loops grow in area and the noise reduction switches to noise enhancement at some transmitted intensities.

With (4.3.33), (4.5.3), and (4.5.4), theoretical noise loops may be calculated. Using α = -2.3, a value which is consistent with our data, $\tau_R\omega_R^2 = 34 \times 10^9$ rad sec^{-1} (ω_R measured experimentally and τ_R taken from the literature [22]), and $\beta = 0.35$ from the linewidth data, the calculated loops in Fig. 4.13 agree well with the measured loops.

In Fig. 4.14, cross-sections of the experimental and theoretical loops at the half intensity transmission point are shown in terms of noise power, normalized by the intrinsic noise level, versus path difference. The optimum reduction is 7 dB for a 4 mm differential delay, which agrees with the theoretical calculation. Also shown

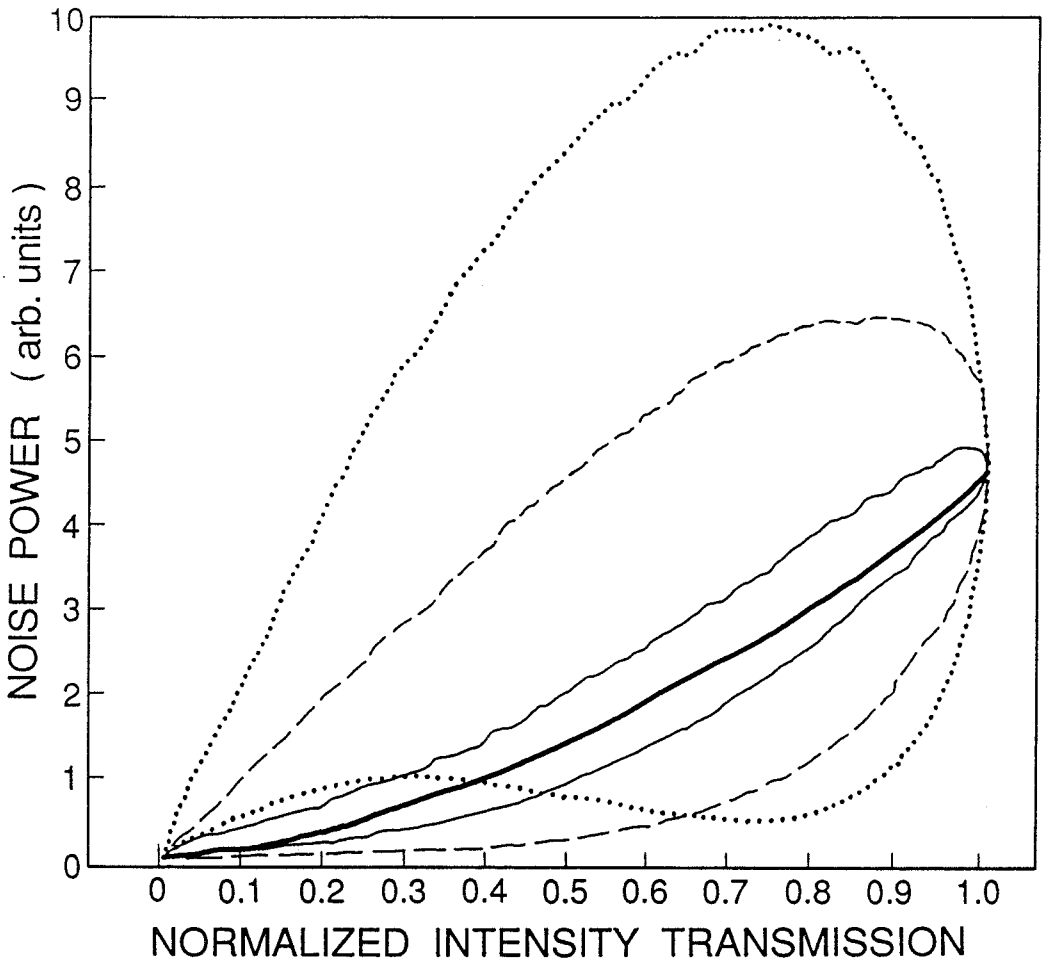

Figure 4.12: Measured intensity noise power vs. normalized intensity transmission through the Michelson for optical path differences of 0 mm (intrinsic noise level), 1, 4, and 7 mm. Loop areas increase with increasing path difference. Both reduction and enhancement of the noise level are apparent.

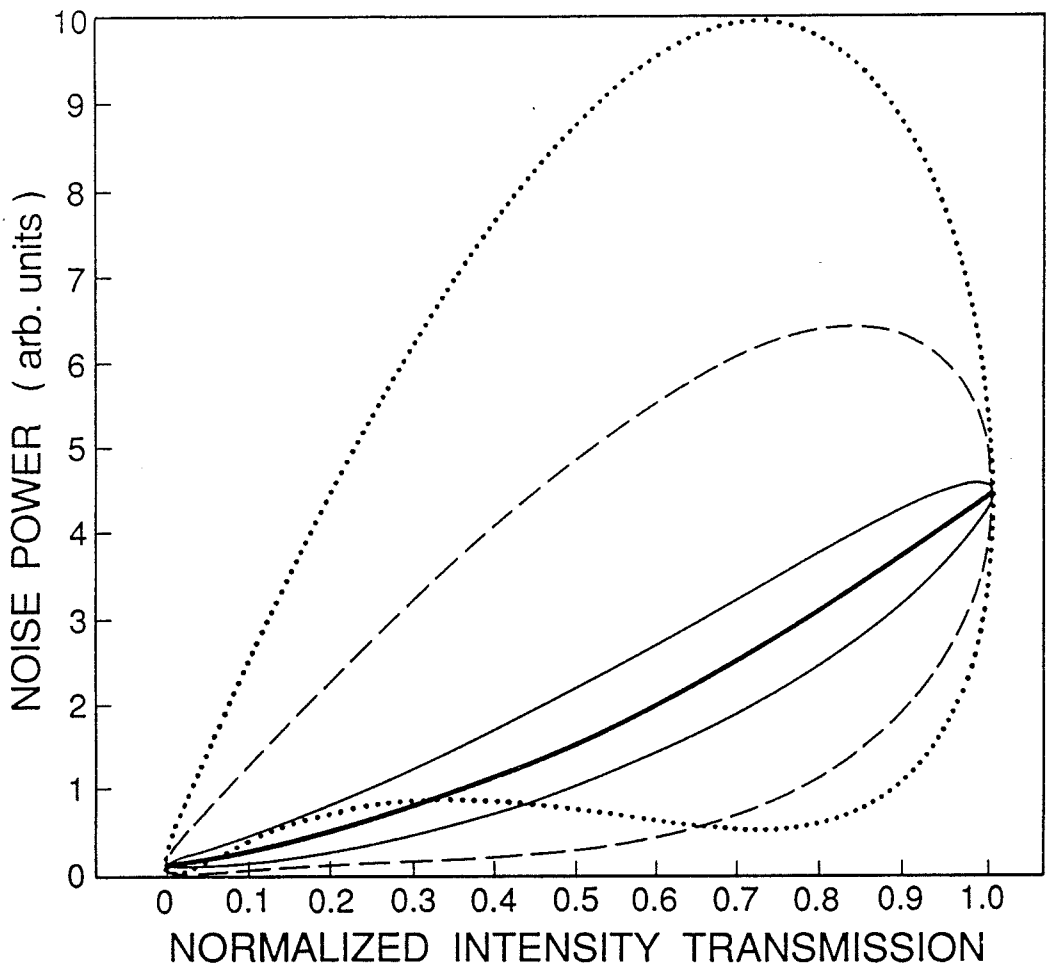

Figure 4.13: Theoretical noise loops for optical path differences of 0 mm (intrinsic noise level), 1, 4, and 7 mm. Loop areas increase with increasing path difference.

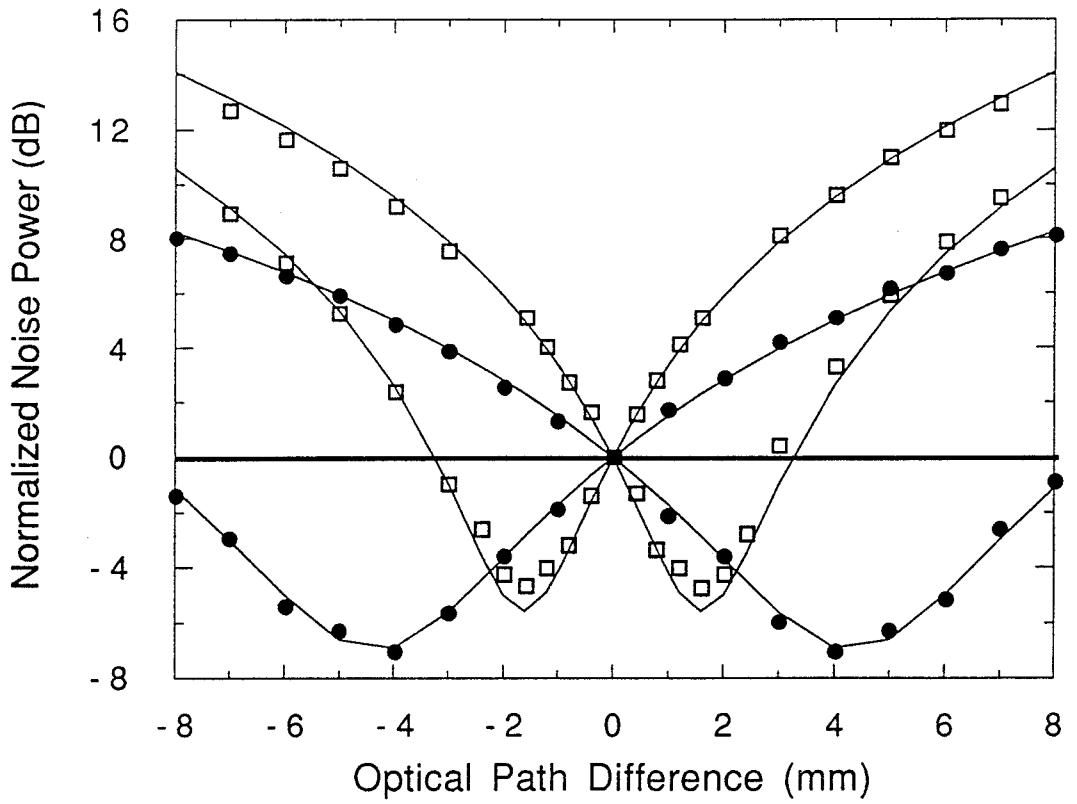

Figure 4.14: Measured noise power at half-intensity transmission through Michelson vs. optical path difference for laser bias of 23.3 mA (filled circles) and 25.7 mA (open squares). Power is normalized by its intrinsic value at zero path difference. Low bias data show 7 dB noise reduction at 4 mm path difference. Theoretical calculations of noise power (lines) from (4.3.33) also appear.

are data from measurements at a higher bias of 25.7 mA, where β is 1.08, $\tau_R\omega_R^2 = 82\times10^9$ rad sec^{-1}, output power = 0.83 mW, and the intrinsic RIN level is -140 dB/Hz. Because β is larger at higher bias, the amount of noise reduction decreases as predicted by (4.3.35). Also, the increase in $\tau_R\omega_R^2$ means the optimum slope is decreased and occurs at a shorter path difference of 1.6 mm, in accordance with (4.3.34). These data agree well with the theoretical plots. Note that the free spectral range of the Michelson is 75 GHz for a path difference of 4 mm. The linear approximation of the transmission function (4.3.1), on which the theoretical analysis of section 4.3 is based, is therefore justified.

The amount of noise reduction continued to diminish as laser power increased. It can be seen however that for a laser having a smaller excess linewidth (smaller β at a given output power), larger amounts of noise reduction are possible at higher powers and at shorter path differences. These small path differences needed to achieve noise reduction suggest that a monolithically integrated version of this technique may be feasible.

For the low bias case at 23.3 mA, Fig. 4.15 shows the maximum measured noise reduction as a function of frequency. The theoretical curve calulated from (4.3.21) and the known value of β also appears. As predicted, the amount of reduction diminishes at higher frequencies where the intrinsic noise spectrum is no longer flat. Note that an additional benefit from a laser with a smaller component of excess linewidth is that noise reduction becomes possible at higher bias levels. The resonance frequency is therefore pushed out to higher frequencies, leading to noise reduction over a wider

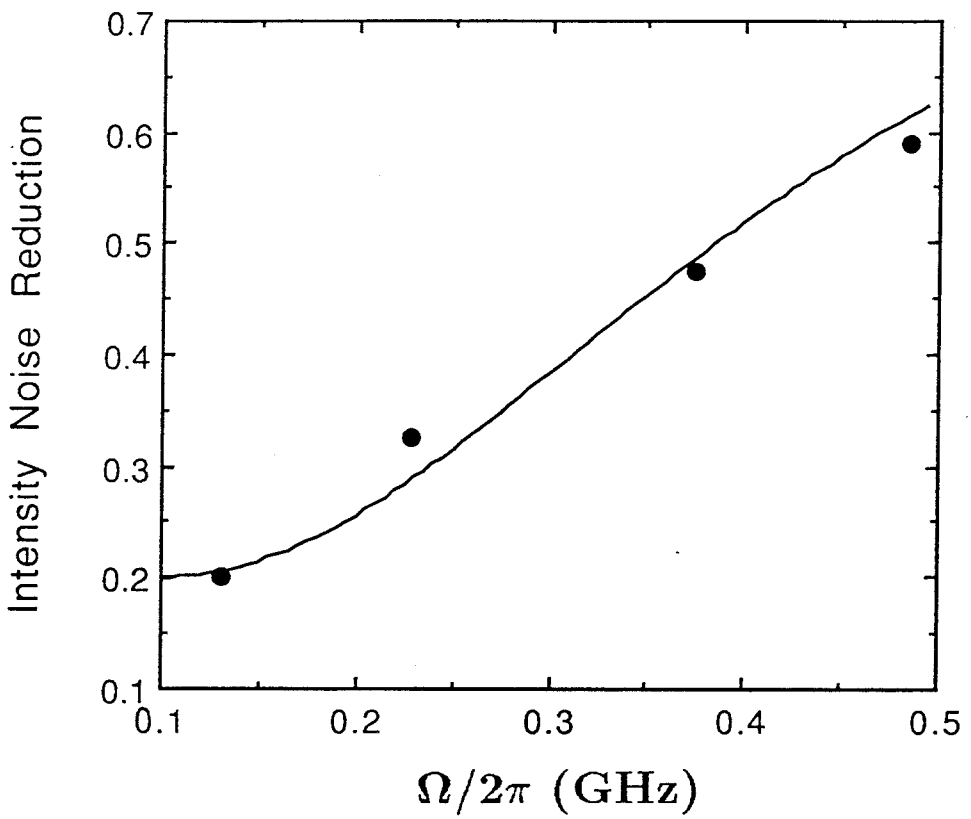

Figure 4.15: Maximum noise power reduction vs. frequency for 23.3 mA laser bias. Measured (dots) and theoretical (line) values are shown. The magnitude of reduction decreases at higher frequencies in accordance with (4.3.21) and Fig. 4.5

bandwidth.

Finally, Fig. 4.16 shows several noise loops for a second InGaAsP DFB laser with a larger α parameter than the DFB laser described above. Noise power was measured at 17.8 MHz (in the flat part of the noise spectrum) in a 100 kHz bandwidth. The laser was biased slightly above threshold for the measurement (bias level = 15.5 mA and threshold current = 14.5 mA), where the output power was 0.22 mW and the intrinsic RIN level was -119 dB/Hz. For a 6.6 mm differential delay in the Michelson, the noise is reduced below the intrinsic level as much as a factor of 28 (14.5 dB). Although the β parameter was not directly measured for this device, a factor of 28 reduction in the intensity noise implies that $|\alpha| \geq 5.2$ (see 4.3.35). Additional measurements on the level of noise reduction for this device in relation to the photon shot noise level appear in chapter 5.

4.6 Conclusion

In conclusion, we have discussed a simple technique, amplitude-phase decorrelation, for reducing the intensity noise floor in a free-running semiconductor laser. Taking advantage of the inherent correlation between the amplitude and phase fluctuations in the laser field, the intensity noise can potentially be reduced by the factor $1/(1+\alpha^2)$, independent of laser power, by using a passive external element with a frequency-dependent transmission. Optimum intensity noise reduction results in decorrelation of the fluctuations. This technique was shown to share some conceptual similarities with detuned loading, where a dispersive loss function is placed inside the laser cavity.

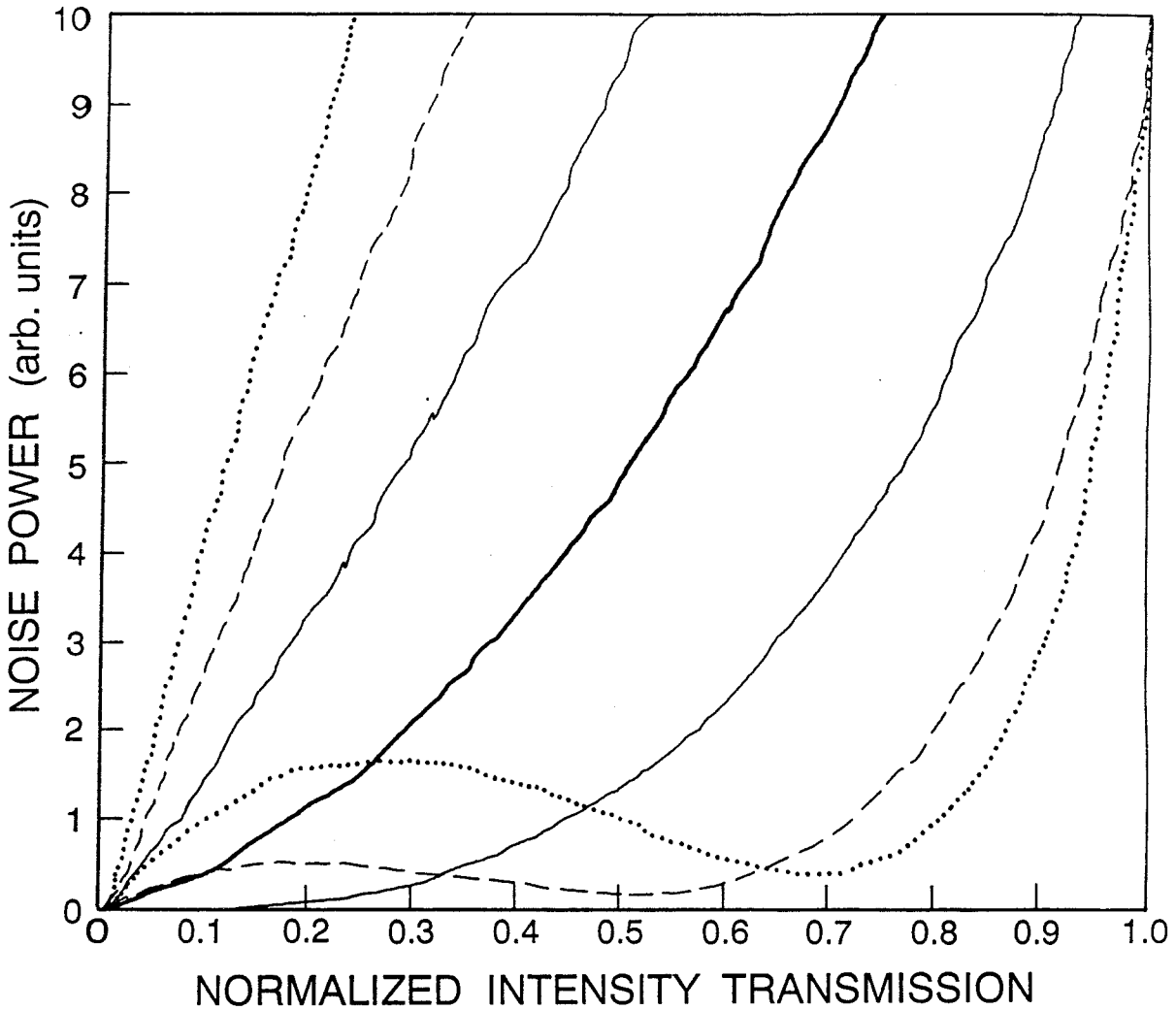

Figure 4.16: Measured noise loops for a different DFB laser (with a larger $|\alpha|$) for path differences of 0.0 mm (intrinsic noise level), 3.0, 6.6, and 9.0 mm. Loop areas increase with increasing path difference. The loop at 6.6 mm delay (dashed line) shows a factor of 28 reduction in noise power at half-intensity transmission.

In that case the maximum intensity noise reduction is also $1/(1+\alpha^2)$. In practice, the presence of a power-independent component of linewidth will limit the amount of reduction that can be achieved. The magnitude of reduction will thus diminish as laser power increases. However, we verify that the intensity noise from a DFB laser diode at low bias can be reduced by as much as 14.5 dB when the passive technique is implemented with a Michelson interferometer. The measured dependence of the noise level on interferometer slope, laser bias, and frequency are in agreement with theory.

Bibliography

[1] D. Welford and A. Mooradian, "Output power and temperature dependence of the linewidth of single frequency cw (GaAl)As diode lasers," *Appl. Phys. Lett.*, vol. 40, pp. 865-867, 1982.

[2] Ch. Harder, K. Vahala, and A. Yariv, "Measurement of the linewidth enhancement factor α of semiconductor lasers," *Appl. Phys. Lett.*, vol. 42, pp. 328-330, 1983.

[3] T. L. Koch and J. E. Bowers, "Nature of wavelength chirping in directly modulated semiconductor lasers," *Electron. Lett.*, vol. 20, pp. 1038-1040, 1984.

[4] M. A. Newkirk and K. J. Vahala, "Amplitude-phase decorrelation: A method for reducing intensity noise in semiconductor lasers," *IEEE J. Quantum Electron.*, vol. QE-27, pp. 13-22, 1991.

[5] K. J. Vahala and M. A. Newkirk, "Intensity noise reduction in semiconductor lasers by amplitude-phase decorrelation," presented at XVII Int. Quantum Electron. Conf., May 21-25, 1990, Anaheim, CA, postdeadline paper QPDP29.

[6] K. J. Vahala and M. A. Newkirk, "Intensity noise reduction in semiconductor lasers by amplitude-phase decorrelation," *Appl. Phys. Lett.*, vol. 57, pp. 974-976, 1990.

[7] C. H. Henry, "Theory of the linewidth of semiconductor lasers," *IEEE J. Quantum Electron.*, vol. QE-18, pp. 259-264, 1982.

[8] M. Osinski and J. Buus, "Linewidth broadening factor in semiconductor lasers – An overview," *IEEE J. Quantum Electron.*, vol. QE-23, pp. 9-29, 1987.

[9] K. Vahala and A. Yariv, "Semiclassical theory of noise in semiconductor lasers – part I," *IEEE J. Quantum Electron.*, vol. QE-19, pp. 1096-1101, 1983.

[10] K. Vahala and A. Yariv, "Semiclassical theory of noise in semiconductor lasers – part II," *IEEE J. Quantum Electron.*, vol. QE-19, pp. 1102-1109, 1983.

[11] R. J. Lang, K. J. Vahala, and A. Yariv, "The effect of spatially dependent temperature and carrier fluctuations on noise in semiconductor lasers," *IEEE J. Quantum Electron.*, vol. QE-21, pp. 443-451, 1985.

[12] C. H. Henry, "Theory of the phase noise and power spectrum of a single mode injection laser," *IEEE J. Quantum Electron.*, vol. QE-19, pp. 1391-1397, 1983.

[13] D. Welford and A. Mooradian, "Observation of linewidth broadening in (GaAl)As diode lasers due to electron number fluctuations," *Appl. Phys. Lett.*, vol. 40, pp. 560-562, 1982.

[14] K. Vahala and A. Yariv, "Occupation fluctuation noise: a fundamental source of linewidth broadening in semiconductor lasers," *Appl. Phys. Lett.*, vol. 43, pp. 140-142, 1983.

[15] K. Uomi, S. Sasaki, T. Tsuchiya, M. Okai, M. Aoki, and N. Chinone, "Spectral linewidth reduction by low spatial hole burning in 1.5 μm multi-quantum-well $\lambda/4$-shifted DFB lasers," *Electron. Lett.*, vol. 26, pp. 52-53, 1990.

[16] K. Kikuchi and T. Okoshi, "Measurement of FM noise, AM noise, and field spectra of 1.3 μm InGaAsP DFB lasers and determination of the linewidth enhancement factor," *IEEE J. Quantum Electron.*, vol. QE-21, pp. 1814-1819, 1985.

[17] K. Vahala and A. Yariv, "Detuned loading in coupled cavity semiconductor lasers-effect on quantum noise and dynamics," *Appl. Phys. Lett.*, vol. 45, pp. 501-503, 1984.

[18] K. Vahala,"Dynamic and spectral features of semiconductor lasers," Ph.D. dissertation, California Instit. Technol., Pasadena, CA, 1985.

[19] K. Vahala, J. Paslaski, and A. Yariv, "Observation of modulation speed enhancement, frequency modulation suppression, and phase noise reduction by detuned loading in a coupled-cavity semiconductor laser," *Appl. Phys. Lett.*, vol. 46, pp. 1025-1027, 1985.

[20] B. Daino, P. Spano, M. Tamburrini, and S. Piazzolla, "Phase noise and spectral lineshape in semiconductor lasers," *IEEE J. Quantum Electron.*, vol. QE-19, pp. 266-270, 1983.

[21] P. Spano, S. Piazzolla, and M. Tamburrini, "Phase noise in semiconductor lasers: A theoretical approach," *IEEE J. Quantum Electron.*, vol. QE-19, pp. 1195-1199, 1983.

[22] R. J. Lang, H. P. Mayer, H. Schweizer, and A. P. Moser, "Measurement of the relaxation resonance, damping, and nonlinear gain coefficient from the sidebands in the field spectrum of a 1.3 μm InGaAsP distributed feedback laser," *Appl. Phys. Lett.*, vol. 54, pp. 1845-1847, 1989.

Chapter 5

Semiconductor laser intensity noise reduction and the photon shot noise floor

5.1 Introduction

In chapter 4 it was shown that the amplitude-phase decorrelation technique may potentially reduce the intensity noise of semiconductor laser light by a factor of $1/(1+\alpha^2)$ below its intrinsic level, where α is the linewidth enhancement factor. This represents a substantial reduction for typical values of α ($\sim$ -5). The question naturally arises: can amplitude-phase decorrelation reduce intensity noise below the level of the photon shot noise? The shot noise level represents a fundamental floor for intensity noise, and the issue of noise reduction below the shot noise level (standard quantum limit) has been the subject of many theoretical and experimental investigations regarding

the generation of sub-Poissonian (squeezed) light [1]–[6].

Because it can be difficult to experimentally establish the photon shot noise level (SNL) with confidence, a balanced homodyne detector (BHD) is used to accurately determine the intensity noise level of the lasing mode in relation to the SNL. First, the performance of the BHD is demonstrated by measuring the intrinsic noise level of a laser diode and SNL as a function of laser power. Measurements on a distributed Bragg reflector (DBR) laser show that at high power, the intrinsic intensity noise level at the device's output facet is only 0.8 dB above the quantum-limited shot noise floor. The theoretical dependence of the measured SNL on optical attenuation is also verified. Second, the BHD is used to complement the amplitude-phase decorrelation experiments of the previous chapter by measuring the noise reduction in relation to the SNL. For the DFB laser studied in chapter 4, the decorrelated noise can be reduced to within 1.3 dB of the SNL. Reduction below the SNL appears to be inhibited by uncorrelated phase noise in the instantaneous frequency fluctuation spectrum.

5.2 Laser intensity noise measurement with a balanced homodyne detector

At low frequencies (i.e., in the flat region of the noise spectrum), the intensity noise spectral density for single mode operation has the form

$$S(I) = 2\hbar\omega_L(\frac{A}{I} + B + CI) \tag{5.2.1}$$

where $\hbar\omega_L$ is the lasing photon energy and I is average output power [7]. (Note: $S(I)$ represents the directly detected noise power which would be measured by a detector and electronic spectrum analyzer, not the RIN, which is proportional to $S(I)/I^2$). The coefficients A, B, and C depend on fundamental laser quantities such as differential gain and spontaneous lifetime, but for now we only wish to consider the qualitative features of $S(I)$. At low power, where the fluctuations are dominated by spontaneous emission, the laser operates in the excess noise regime, where $S(I)$ has a $1/I$ dependence. As I increases, the noise level eventually begins to rise as the laser enters the shot noise regime. It thus becomes important to relate $S(I)$ to the fundamental, quantum-limited spectral density of shot noise, given by $2\hbar\omega_L I$ [8].

5.2.1 Balanced homodyne detection

Many experimental approaches to establish the SNL involve a fair degree of uncertainty. One may measure the noise power of an incoherent, shot-noise-limited light source, such as an incandescent filament [9], LED [10], or a highly attenuated laser beam [11]. This reading of the SNL is then compared to the measured laser noise level for the same dc photocurrent induced in the detector. However, this approach has a major drawback. Although the detector dc photocurrents for the SNL calibration and laser noise measurement may be equal, this does not imply that the frequency response of the detector is the same in both cases. In particular, a typical high-performance *p-i-n* photodiode has both a dc and ac response which separately depends on the location of the focused spot, the optical intensity, and the spectral distribution of the radiation. If any of these quantities changes between the SNL cal-

ibration and the laser noise measurement, then the meaning of the SNL calibration is questionable. These issues are not trivial. In our laboratory, we have seen as much as 4 dB variation in the measured laser intensity noise power as the beam focus on the detector is adjusted, even though the dc photocurrent remains constant to within a percent.

Another approach to establish the SNL is to measure the detector current and calculate the shot noise spectral density using the well-known $2q\langle I\rangle$ formula, where q and $\langle I\rangle$ are the electron charge and dc photocurrent, respectively. This is an indirect method, however, which requires precise knowledge of detector response, amplifier gain and noise figure, losses in the detection system, and the effective integration bandwidth of the spectrum analyzer. Several dB's of uncertainty in the location of the SNL may easily accumulate.

A better approach is to use the laser itself to directly establish the SNL. This may be accomplished with a balanced homodyne detector (BHD), as shown in Fig. 5.1 [12]. The physical principles of balanced detection are discussed in [13] and [14]. In a generalized balanced detection scheme, two input modes a and b are coupled by a beam splitter into output modes c and d. In terms of the beam splitter scattering matrix [14], we have

$$e^{i\delta}\begin{pmatrix} \sqrt{R}\,e^{i\phi} & \sqrt{1-R} \\ \sqrt{1-R} & -\sqrt{R}\,e^{-i\phi} \end{pmatrix}\begin{pmatrix} a \\ b \end{pmatrix} = \begin{pmatrix} c \\ d \end{pmatrix} \tag{5.2.2}$$

where R is the power reflectivity of the beam splitter. The phase angles δ and ϕ depend on the beam splitter material and coatings, but their actual values are not important, as shown below.

For noise measurements, the laser light constitutes one input to a 50/50 beam splitter ($R = 1/2$ in (5.2.2)), as seen in Fig. 5.1. In a quantum field description, the laser field is represented by the sum of mean amplitude A_l and noise component Δa_l. The laser field forms input a in (5.2.2). A vacuum field, with zero mean amplitude and noise component Δa_v, enters the open beam splitter port, forming input b. These fields are mixed by the beam splitter and the output fields c and d are detected by two ideal (unity quantum efficiency) photodetectors, generating currents $I_1 \sim |c|^2$ and $I_2 \sim |d|^2$. Using (5.2.2), the photocurrents I_1 and I_2 may be expressed as

$$I_1 \sim \frac{1}{2}|A_l + \Delta a_l + \Delta a_v|^2 \tag{5.2.3}$$

$$I_2 \sim \frac{1}{2}|A_l + \Delta a_l - \Delta a_v|^2 \tag{5.2.4}$$

which are independent of the phase shifts intrinsic to the beam splitter. To highest order, the noise-carrying parts of I_1 and I_2 are given by

$$I_1 \sim A_l(\Delta a_l + \Delta a_v) \tag{5.2.5}$$

$$I_2 \sim A_l(\Delta a_l - \Delta a_v). \tag{5.2.6}$$

Thus, by coherently adding or subtracting I_1 and I_2, followed by detection with a spectrum analyzer, the measured noise spectra are

$$\langle (I_1 + I_2)^2 \rangle \sim 4A_l^2 \langle (\Delta a_l)^2 \rangle \tag{5.2.7}$$

$$\langle (I_1 - I_2)^2 \rangle \sim 4A_l^2 \langle (\Delta a_v)^2 \rangle \tag{5.2.8}$$

which represent the laser's intrinsic intensity noise level and the quantum SNL, respectively.

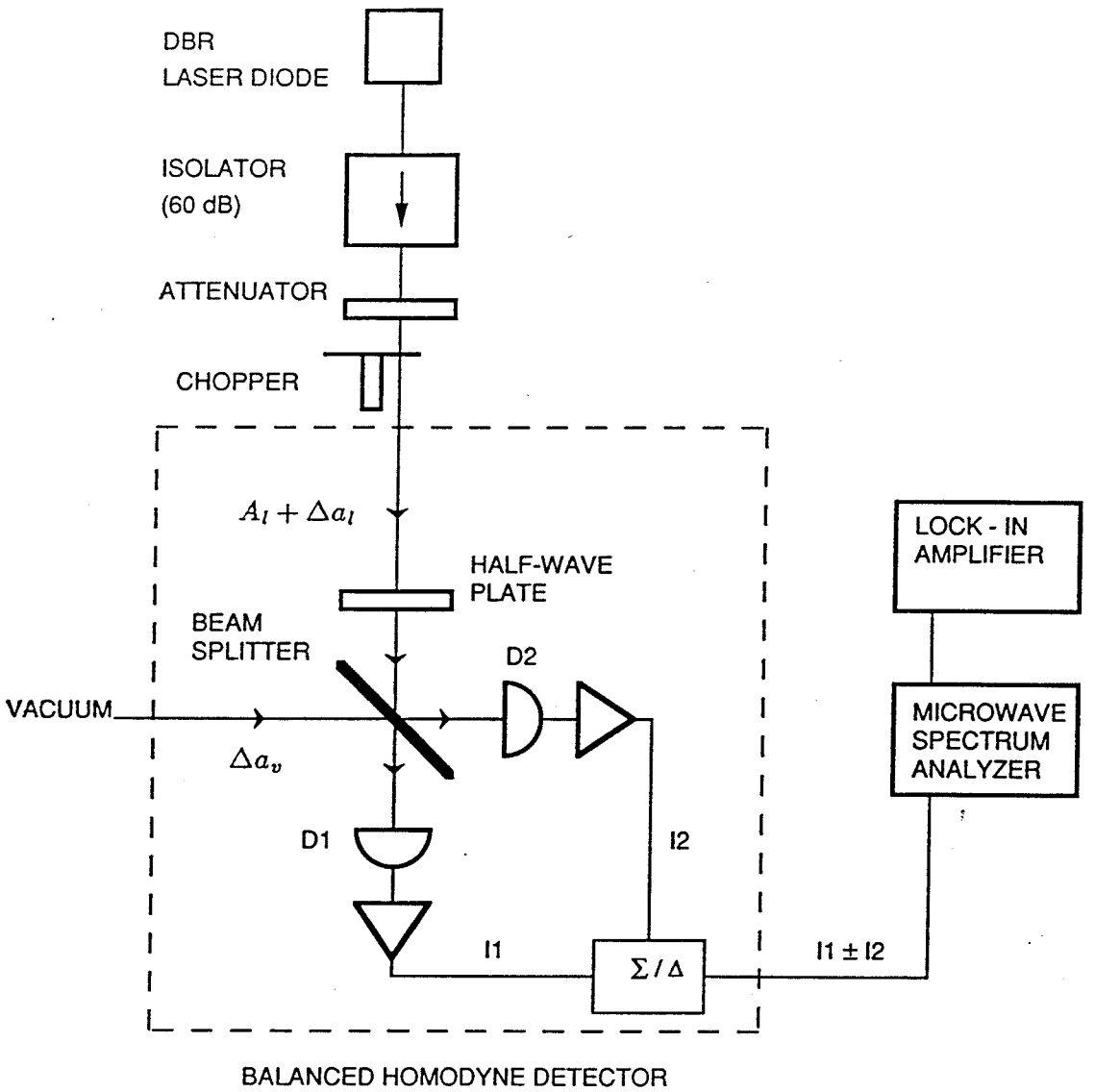

Figure 5.1: Schematic diagram of the intensity noise measurement setup including the balanced homodyne detector.

5.2.2 Experimental details

In the experimental arrangement shown in Fig. 5.1, the laser output is sent through an optical isolator with 60 dB isolation to prevent feedback effects. The input light to the BHD is divided by a half-wave plate and polarization-sensitive beam splitter. Two matched InGaAs/InP *p-i-n* photodiodes (BT&D PDH0004) with 0.90 quantum efficiency are used in conjunction with a bias tee and a high-gain, low-noise amplifier (Avantek ACT10-213-1). The amplified ac currents are combined in a broadband hybrid junction [15] which may coherently add or subtract the two inputs. The combined noise photocurrents are sent to a microwave spectrum analyzer (HP 8558B) to measure noise power. Lock-in detection is also used to improve the sensitivity and to filter thermal noise.

The optical powers in the two detector arms are balanced by rotating the half-wave plate. It is also important that the path lengths of the two arms be made equal [15]. This is accomplished by current modulating the laser diode at the measurement frequency, subtracting the two photocurrents with the hybrid junction, and adjusting the differential path length until the modulation peak seen on the spectrum analyzer is minimized. By this approach, a common mode rejection of 60 dB could be obtained. Once the BHD is balanced, the noise level of the lasing mode or the SNL may be observed by switching between the summing and differencing output ports of the hybrid junction, respectively. No other change to the system is required. Thus, the uncertainties in establishing the SNL as discussed above are not a factor.

5.2.3 Experimental results

The BHD is used to study the intensity noise level of a 1.5 μm InGaAs/InGaAsP strained-layer multi-quantum well distributed Bragg reflector (DBR) laser [16], [17]. Measured noise power at 130 MHz (within the flat part of the spectrum) versus laser output power is shown in Fig. 5.2. When the detector photocurrents are subtracted, the SNL is measured, which appears as a line intercepting at zero power, as it should. When the photocurrents are added, the intrinsic noise level of the lasing mode is measured. Both the excess noise regime at low power, where the noise level falls with increasing power, and the shot noise regime at higher power, where the noise level increases with power, are apparent. A numerical fit to the intrinsic noise data of the form of (5.2.1) and a linear fit to the SNL data are also shown. This laser appears to operate extremely close to the SNL even for modest output power. However, the effect of loss between the laser and detectors, including the non-unity detector quantum efficiency [14], must be accounted for to relate measured noise to the true noise level at the output facet.

A lossy optical channel attenuates the mean photon number as follows: $\langle N \rangle_{in} \xrightarrow{\text{loss}} \langle N \rangle_{out} = \eta \langle N \rangle_{in}$ where η is the coupling efficiency. The noise statistics are altered in a less straightforward way. In terms of photon number variance, proportional to measured noise power, this relationship is [10]

$$\frac{\langle (\Delta N)^2 \rangle_{out}}{\langle N \rangle_{out}} = \eta \frac{\langle (\Delta N)^2 \rangle_{in}}{\langle N \rangle_{in}} + 1 - \eta. \tag{5.2.9}$$

Equation (5.2.9) is merely an instance of the quantum-mechanical fluctuation dissipation theorem, whereby leakage from a system to a reservoir (loss) necessarily couples

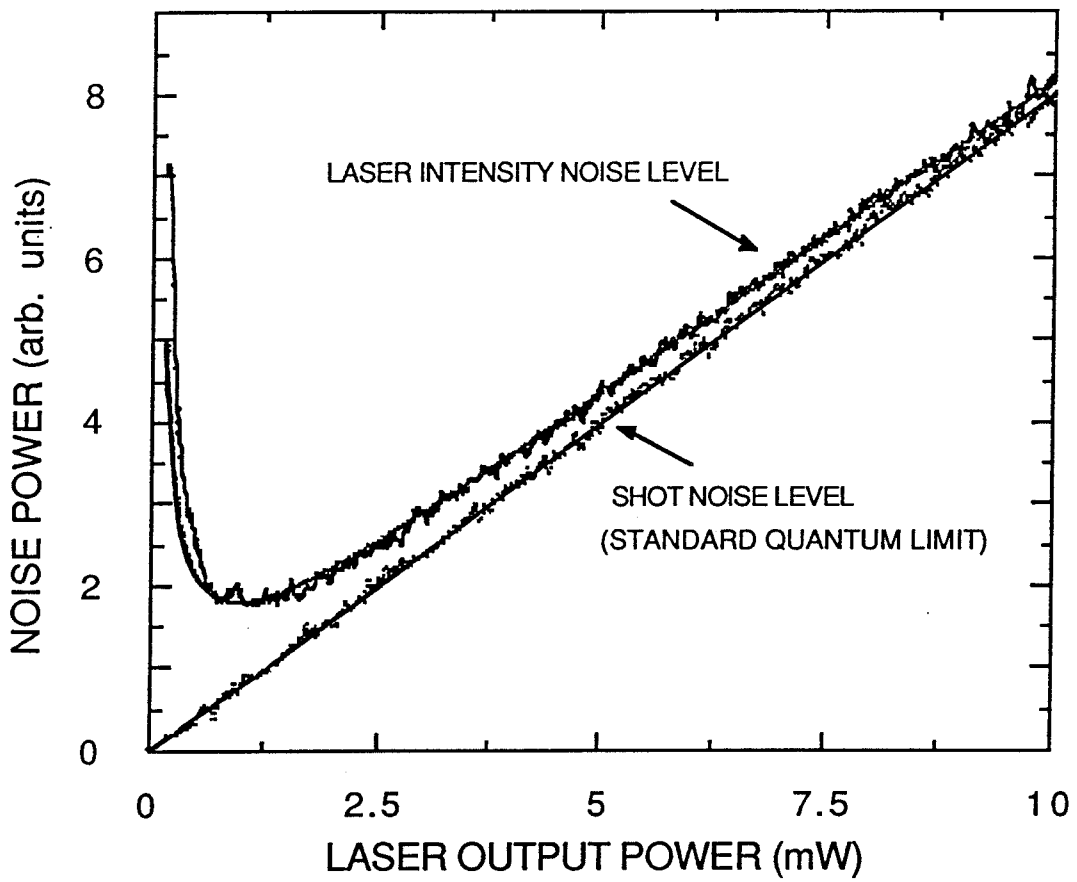

Figure 5.2: DBR laser intensity noise (at 130 MHz) vs. output power measured with a balanced homodyne detector. Both the laser's intrinsic noise level and shot noise level (SNL) are shown. A theoretical fit to the intrinsic noise of the form of (5.2.1) and a linear fit to the SNL are superimposed on the data.

reservoir fluctuations into the system. In this case, the reservoir is the vacuum, and the impact of the vacuum fluctuations is described by the $1 - \eta$ term in the above relation.

We see from (5.2.9) that loss affects shot noise and excess noise in fundamentally different ways. First of all, shot noise has Poissonian statistics, where $\langle(\Delta N)^2\rangle_{in} = \langle N\rangle_{in}$, and hence, when there is loss, the SNL versus incident power is unchanged, i.e., $\langle(\Delta N)^2\rangle_{out}/\langle N\rangle_{out} = \langle(\Delta N)^2\rangle_{in}/\langle N\rangle_{in}$. In contrast, light with excess noise, where $\langle(\Delta N)^2\rangle_{in} > \langle N\rangle_{in}$, will appear relatively less noisy after experiencing loss, i.e., $\langle(\Delta N)^2\rangle_{out}/\langle N\rangle_{out} < \langle(\Delta N)^2\rangle_{in}/\langle N\rangle_{in}$.

Equation (5.2.9) may be used to verify that the balanced detector is actually measuring the SNL. Fig. 5.3 shows the measured SNL versus mean detector photocurrent when the currents are subtracted by the hybrid junction. When the laser power is changed by ramping the laser bias current down to threshold, measured noise power follows a line which intercepts at zero power, indicative of shot noise, as in Fig. 5.2. Alternatively, when the laser bias is fixed and the incident optical power to the BHD is reduced by putting neutral density filters in the beam, the measured noise falls exactly on the same line. Thus, for a given incident optical power, the measured SNL is independent of loss before the detector—a fundamental property of photon shot noise.

Equation (5.2.9) may also be used to factor out the effect of loss on the DBR laser noise measurement. For the data in Fig. 5.2, $\eta = 0.10$, which includes losses from the optical components, a neutral density filter to keep the dc photocurrents below 1 mA,

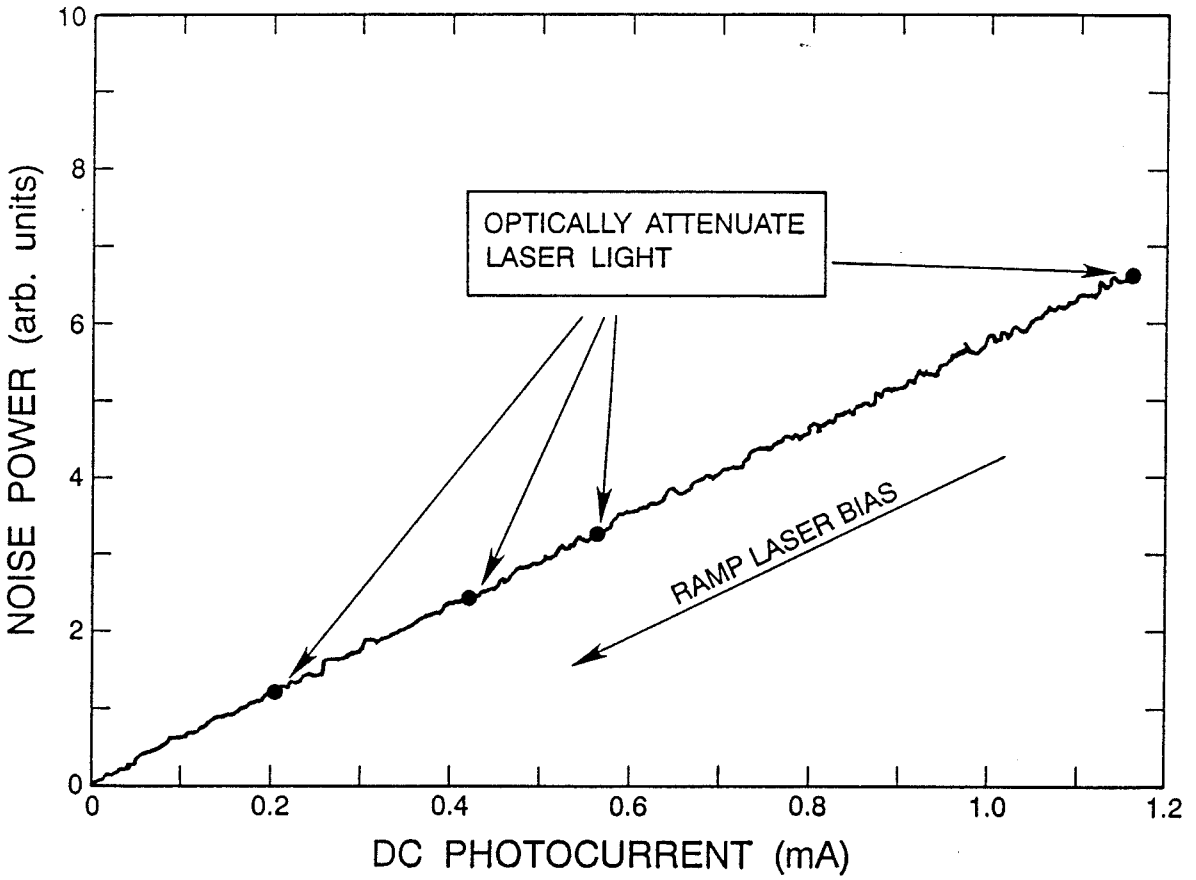

Figure 5.3: Measurement of the shot noise level (SNL) vs. average detector photocurrent. To confirm shot noise behavior, the SNL is seen to be a linear function of incident optical power independent of optical loss before the detector. The incident optical power is varied either by changing the laser bias or by inserting neutral density filters in the beam.

and the non-unity detector quantum efficiency. Fig. 5.4 shows relative intensity noise (RIN) versus incident laser power where, by definition,

$$\mathrm{RIN} = \frac{\langle (\Delta N)^2 \rangle}{\langle N \rangle^2}. \tag{5.2.10}$$

Because of loss, the measured RIN appears closer to the SNL than the true RIN at the output facet. Even so, at 10 mW output power, the DBR laser's intrinsic intensity noise level at the output facet is seen to be only 0.8 dB above the SNL (a very quiet laser).

From these results, we see that the balanced detector provides an ideal tool with which to study laser intensity noise near the quantum level.

5.3 Amplitude-phase decorrelation in relation to the photon shot noise floor

Using the BHD at the output of the Michelson interferometer (see Fig. 4.9), amplitude-phase decorrelation experiments were performed on the DFB laser discussed at the end of chapter 4. Noise loops and the SNL could be measured for a particular laser bias point by scanning the Michelson (see Fig. 4.11) and either adding or subtracting the detector photocurrents. Again, because no adjustments are made to the detectors or laser during the measurement, the balanced detector can unambiguously determine where the intensity noise reduction stands in relation to the fundamental photon shot noise level.

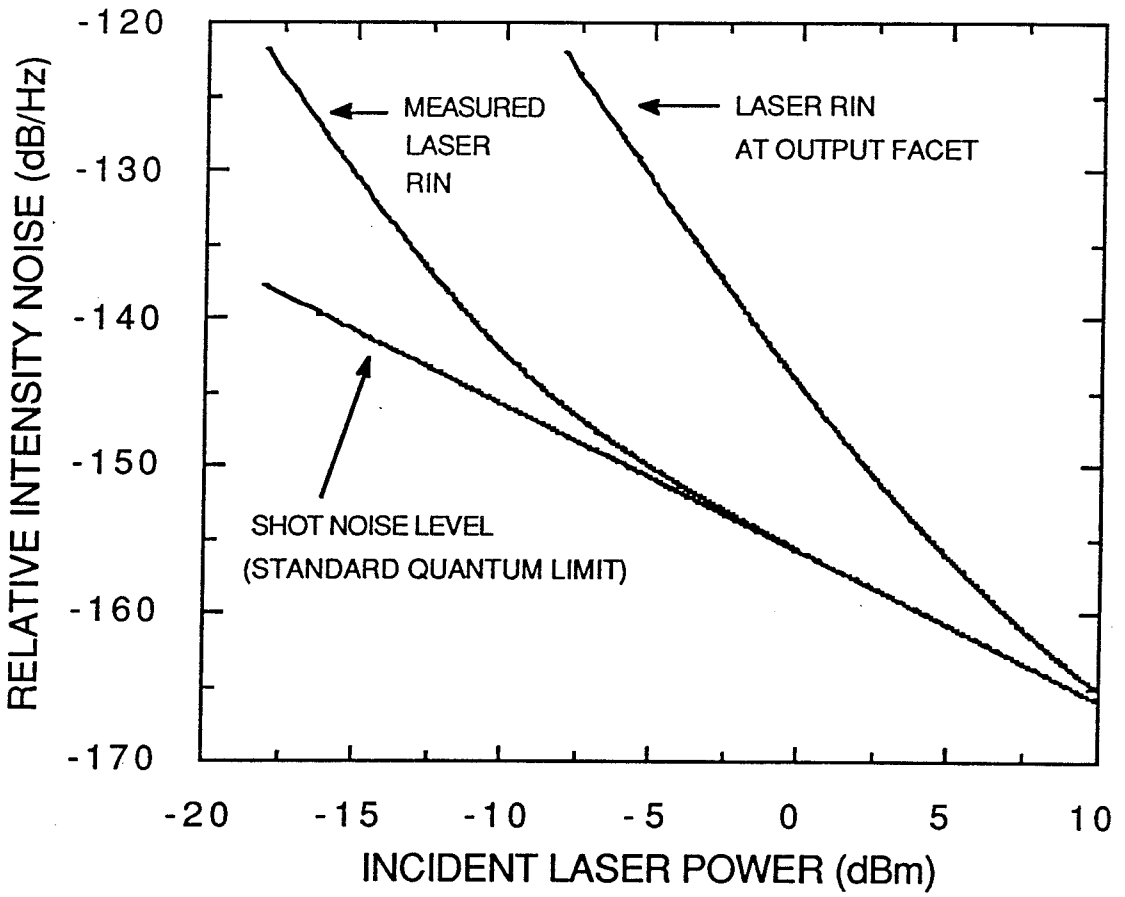

Figure 5.4: Relative intensity noise (RIN) of the DBR lasing mode and the SNL vs. incident optical power. The effect of loss on the measured noise is factored out to give the true RIN at the output facet. The RIN falls with increasing power and comes within 0.8 dB of the SNL at 10 mW output power.

5.3.1 Experimental results

Measurements were performed on the DFB laser for a range of bias points from 15.5 mA (near threshold) up to 40.0 mA. Noise power was measured at 17.8 MHz (in the flat region of the spectrum) in a 100 kHz bandwidth. Figures 5.5 and 5.6 show a representative series of loops and the SNL, as a function of detector dc photocurrent, for two different laser bias points. It can be seen that although the noise power may show a substantial reduction below the intrinsic level, the reduced noise remains above the shot noise floor. In Fig. 5.7 noise power, as a function of incident laser power, is shown in terms of RIN for the range of bias points tested. For each bias point the shot noise level, intrinsic noise level, and maximally reduced noise level are shown. The intrinsic RIN and reduced RIN describe the noise level at the output of the Michelson interferometer, where the effect of loss between the Michelson output and *p-i-n* detectors has been factored out in accordance with (5.2.9). The detection quantum efficiency *after* the Michelson is 0.82, so there is very little difference between the measured noise level and the true level at the Michelson output. At 15.5 mA bias (-12 dBm incident power), the noise is reduced by a factor of 28.6 (14.5 dB), as described in section 4.5. As the bias level increases, the intrinsic noise level falls, in accordance with (5.2.1), and the amount of reduction decreases as the reduced noise level approaches the SNL. At 40.0 mA bias (3.7 dBm incident power), the noise level can only be reduced by 3.4 dB below the intrinsic level, and the reduced noise is within 1.3 dB of the SNL.

The observed power dependence of the magnitude of reduction is consistent with

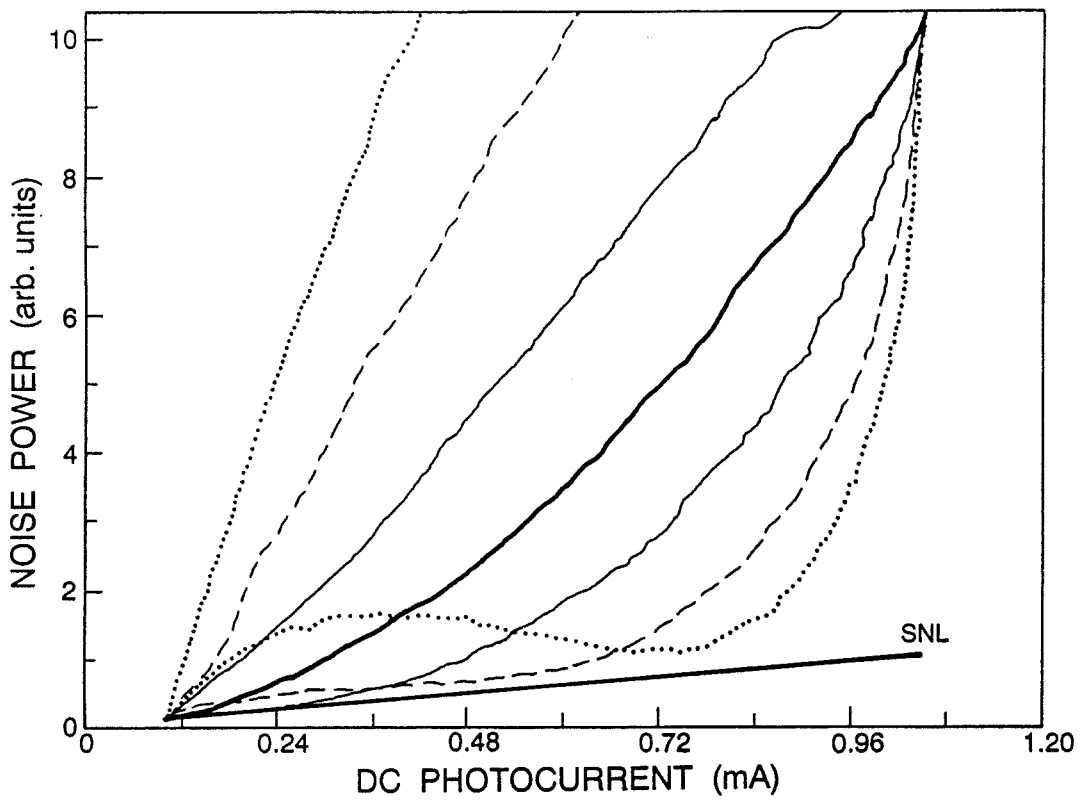

Figure 5.5: Noise loops and the shot noise level vs. detector dc current. DFB laser bias is 24.0 mA (threshold is 14.5 mA). Loops correspond to interferometer path differences of 0.0 mm (intrinsic noise level), 0.4, 0.8, and 1.2 mm. Loop areas increase with increasing path difference.

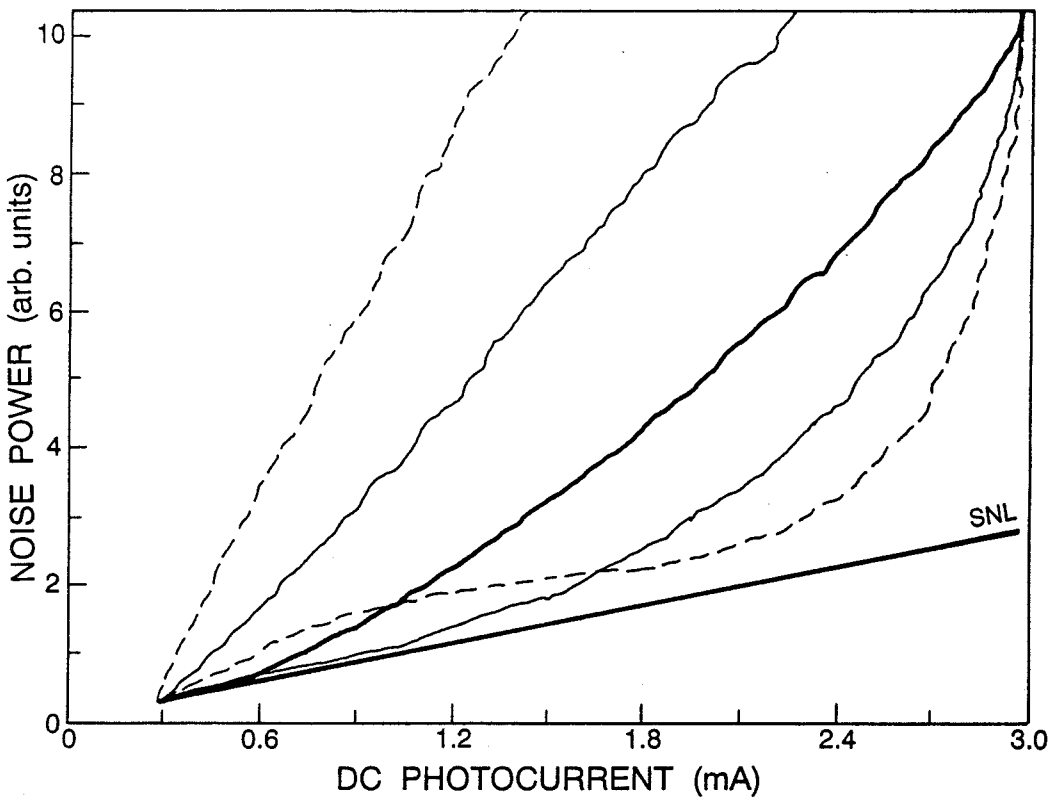

Figure 5.6: Noise loops and the shot noise level vs. detector dc current. DFB laser bias is 40.0 mA (threshold is 14.5 mA). Loops correspond to interferometer path differences of 0.0 mm (intrinsic noise level), 0.26, and 0.46 mm. Loop areas increase with increasing path difference.

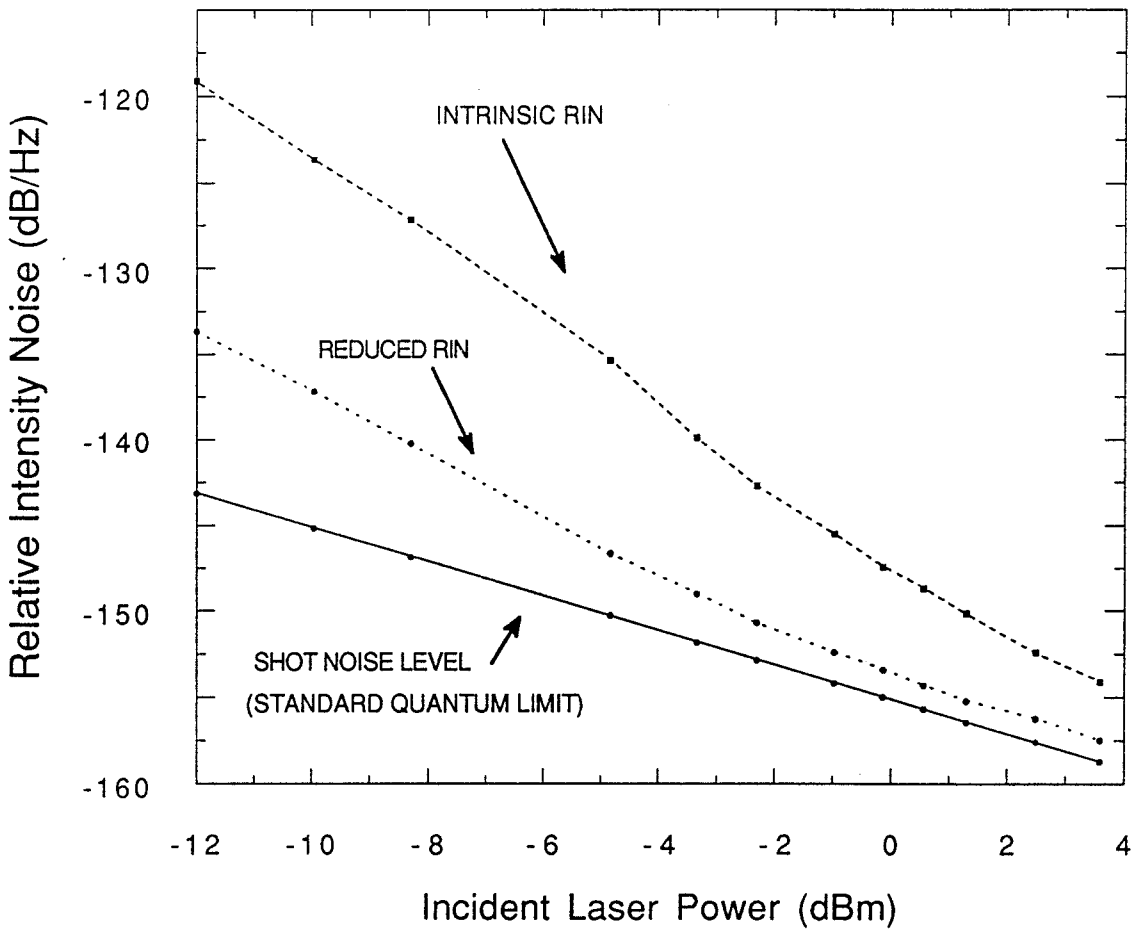

Figure 5.7: Intrinsic RIN, reduced RIN, and the shot noise level vs. incident power to the balanced detector. Laser bias points range from 15.5 mA to 40.0 mA. Intensity noise is reduced by 14.5 dB at low bias. At high bias, the noise is reduced to within 1.3 dB of the SNL, but the magnitude of reduction decreases.

the presence of an uncorrelated, power-independent source of phase noise ($\tilde{\Delta}_o$) in the instantaneous frequency fluctuation spectrum (see 4.2.15). The Michelson converts $\tilde{\Delta}_o$ into additive intensity noise, giving a maximum reduction (4.3.35)

$$\frac{\mathrm{RIN}_o}{\mathrm{RIN}_i} = \frac{1+\beta}{1+\alpha^2+\beta} \tag{5.3.1}$$

where β is the ratio of the power-independent linewidth (the spectral density of $\tilde{\Delta}_o$) to the Schawlow-Townes linewidth, so that β is proportional to output power. For this DFB laser, it was not possible to directly determine β from a linewidth measurement, because the laser could not be taken to high enough power to observe linewidth saturation. However, from (5.3.1), β may be written as

$$\beta = \frac{\alpha^2}{\frac{\mathrm{RIN}_i}{\mathrm{RIN}_o} - 1} - 1. \tag{5.3.2}$$

From the maximum measured noise reduction RIN_o / RIN_i for each power level (the data in Fig. 5.7), the power dependence of β may be determined. We take $|\alpha|$ to be 5.25, consistent with the factor of 28.6 reduction near threshold. In Fig. 5.8, we see that β as a function of laser power fits to a reasonable line, in agreement with the simple model incorporating a power-independent source of phase noise in the rate equations.

Similar measurements with the balanced detector on a variety of DFB lasers and the DBR laser discussed above showed in all cases that amplitude-phase decorrelation could reduce the intensity noise to a level very near, but not below the SNL. Insofar as noise reduction is inhibited by the power-independent linewidth, a specialized DFB laser with a narrow high-power linewidth, such as described in [18], may provide an

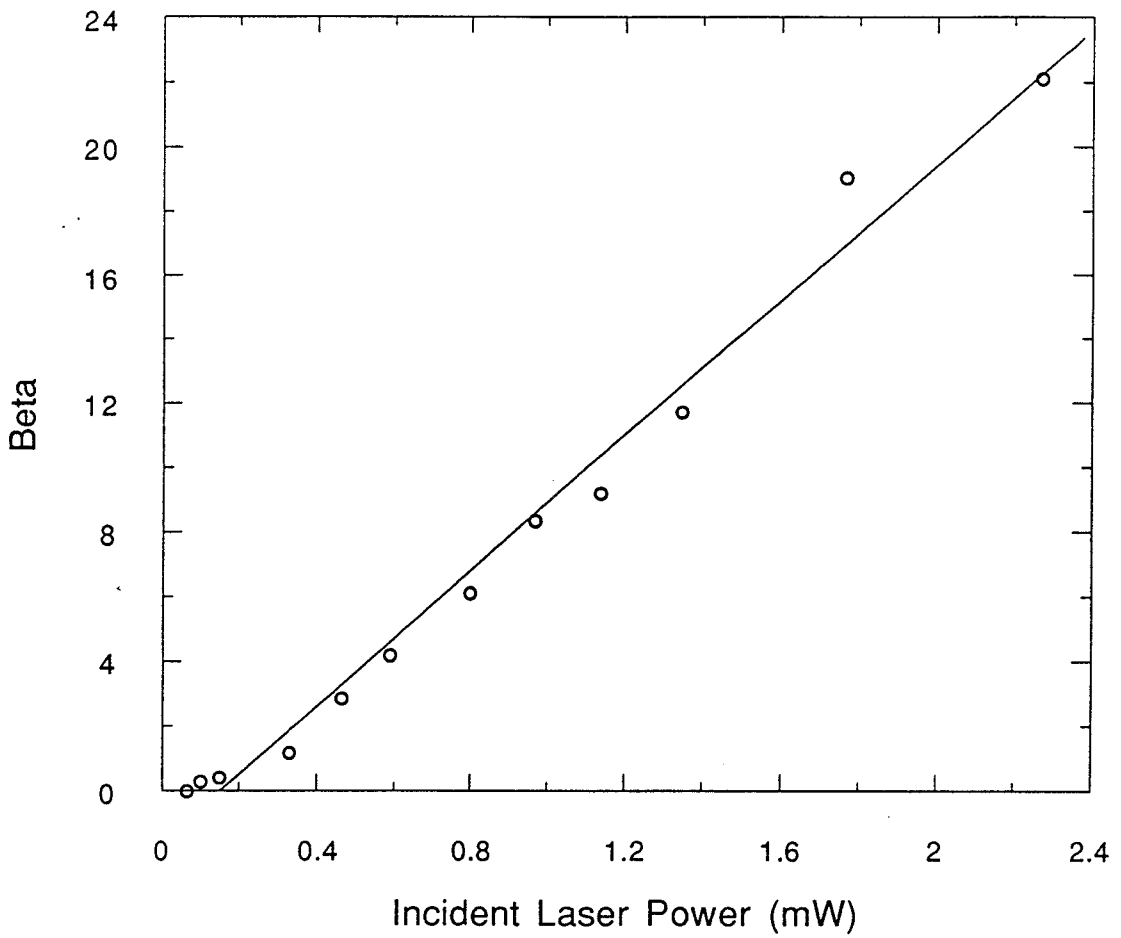

Figure 5.8: Beta, from (5.3.2), vs. incident laser power. A linear relationship, consistent with the presence of a power-independent source of phase noise in the rate equations, is observed.

ideal source with which to demonstrate amplitude-phase decorrelation below the SNL.

5.3.2 Amplitude-phase decorrelation at the quantum level

Although the semiclassical formulation of amplitude-phase decorrelation agrees with all aspects of the observed noise reduction, the issue of reduction below the shot noise level properly requires a quantum-mechanical treatment. The shot noise level is a manifestation of the zero-point (vacuum) fluctuations of a quantized radiation field, and reduction below this level is tantamount to reducing the variance of the amplitude quadrature of the field below this quantum-mechanical minimum.

Some new issues which would arise in a quantum treatment are briefly discussed here. Because the Michelson, in order to have a finite slope at the lasing frequency, must be detuned from maximum transmission, this allows vacuum fluctuations to couple into the Michelson's open port. These fluctuations, being uncorrelated with the lasing mode, dilute the inherent correlation between the lasing mode fluctuations, inhibiting noise reduction by the decorrelation technique. Sources of loss other than the Michelson will also couple vacuum into the lasing mode, further diluting the correlation.

The semiclassical rate equations (4.2.4)–(4.2.6) describe the field fluctuations within the laser cavity. The output field, the one accessible to measurement, is a replica of the intra-cavity field. At the quantum level this is no longer true. There are differences between the intra-cavity and output fields. For instance, a vacuum field which couples into the cavity can interfere with itself at the laser facet [19]. Furthermore, pump fluctuations should be taken into account, as these will affect the lasing field

fluctuations [20]. Indeed, it has been argued that by suppressing pump noise in a laser diode, the intrinsic intensity noise can be sub-Poissonian when the laser is at very high bias [21].

5.4 Conclusion

We have used a balanced homodyne detector to measure intensity noise reduction by the amplitude-phase decorrelation technique in relation to the photon shot noise level. For all lasers studied, intensity noise could be reduced close to, but not below this fundamental noise floor. The observed power dependence of the reduction was consistent with the presence of a power-independent source of phase noise in the instantaneous frequency fluctuation spectrum.

Bibliography

[1] L. Wu, H. J. Kimble, J. L. Hall, and H. Wu, "Generation of squeezed states by parametric down conversion," *Phys. Rev. Lett.*, vol. 57, pp. 2520-2523, 1986.

[2] R. E. Slusher, L. W. Hollberg, B. Yurke, J. C. Mertz, and J. F. Valley, "Observation of squeezed states generated by four-wave mixing in an optical cavity," *Phys. Rev. Lett.*, vol. 55, pp. 2409-2412, 1985.

[3] G. J. Milburn, M. D. Levenson, R. M. Shelby, S. H. Perlmutter, R. G. DeVoe, and D. F. Walls, "Optical-fiber media for squeezed-state generation," *J. Opt. Soc. Am. B*, vol. 4, pp. 1476-1489, 1987.

[4] F. Haake, S. M. Tan, and D. F. Walls, "Photon noise reduction in lasers," *Phys. Rev. A*, vol. 40, pp. 7121-7132, 1989.

[5] W. H. Richardson, S. Machida, and Y. Yamamoto, "Observation of 10 dB squeezing in the amplitude fluctuations of light from a diode laser," presented at XVII Int. Quantum Electron. Conf., May 21-25, 1990, Anaheim, CA, postdeadline paper QPDP28.

[6] J. Mertz, A. Heidmann, C. Fabre, E. Giacobino, and S. Reynaud, "Observation of high-intensity sub-poissonian light using an optical parametric oscillator," *Phys. Rev. Lett.*, vol. 64, pp. 2897-2900, 1990.

[7] G. P. Agrawal and N. K. Dutta, *Long-Wavelength Semiconductor Lasers*, New York: Van Nostrand Reinhold, 1986, pp. 250-251.

[8] C. S. Harder, "Bistability, high-speed modulation, noise, and pulsation in GaAlAs semiconductor lasers," Ph.D. dissertation, California Instit. Technol., Pasadena, CA, 1983, pp. 139-141.

[9] R. M. Shelby, M. D. Levenson, S. H. Perlmutter, R. G. DeVoe, and D. F. Walls, "Broad-band parametric deamplification of quantum noise in an optical fiber," *Phys. Rev. Lett.*, vol. 57, pp. 691-694, 1986.

[10] S. Machida and Y. Yamamoto, "Quantum-limited operation of balanced mixer homodyne and heterodyne receivers," *IEEE J. Quantum Electron.*, vol. QE-22, pp. 617-624, 1986.

[11] S. Machida, Y. Yamamoto, and Y. Itaya, "Observation of amplitude squeezing in a constant-current-driven semiconductor laser," *Phys. Rev. Lett.*, vol. 58, pp. 1000-1003, 1987.

[12] M. A. Newkirk and K. J. Vahala, "Investigation of the intensity noise level of a 1.3 μm InGaAsP DFB laser by measurement with a balanced homodyne detector," presented at Opt. Fiber Comm. Conf., Feb. 18-22, 1991, San Diego, CA, paper WG3.

[13] H. P. Yuen and V. W. S. Chan, "Noise in homodyne and heterodyne detection," *Opt. Lett.*, vol. 8, pp. 177-179, 1983.

[14] B. Schumaker, "Noise in homodyne detection," *Opt. Lett.*, vol. 9, pp. 189-191, 1984.

[15] G. L. Abbas, V. W. S. Chan, and T. K. Yee, "A dual-detector optical heterodyne receiver for local oscillator noise suppression," *J. Lightwave Technol.*, vol. LT-3, pp. 1110-1122, 1985.

[16] T. L. Koch, U. Koren, and B. I. Miller, "High performance tunable 1.5 μm InGaAs/InGaAsP multiple quantum well distributed Bragg reflector lasers," *Appl. Phys. Lett.*, vol. 53, pp. 1036-1038, 1988.

[17] S. L. Woodward, T. L. Koch, and U. Koren, "RIN in multisection MQW-DBR lasers," *Photon. Tech. Lett.*, vol. 2, pp. 104-108, 1990.

[18] K. Uomi, S. Sasaki, T. Tsuchiya, M. Okai, M. Aoki, and N. Chinone, "Spectral linewidth reduction by low spatial hole burning in 1.5 μm multi-quantum-well $\lambda/4$-shifted DFB lasers," *Electron. Lett.*, vol. 26, pp. 52-53, 1990.

[19] M. J. Collett and C. W. Gardiner, "Squeezing of intracavity and traveling-wave light fields produced in parametric amplification," *Phys. Rev. A*, vol. 30, pp. 1386-1391, 1984.

[20] J. Bergou, L. Davidovich, M. Orszag, C. Benkert, M. Hillery, and M. O. Scully, "Role of pumping statistics in maser and laser dynamics: Density-matrix approach," *Phys. Rev. A*, vol. 40, pp. 5073-5080, 1989.

[21] Y. Yamamoto and S. Machida, "High-impedance suppression of pump fluctuations and amplitude squeezing in semiconductor lasers," *Phys. Rev. A*, vol. 35, pp. 5114-5130, 1987.